Materials Science and Engineering R 71 (2011) 53–86

Contents lists available at ScienceDirect

Materials Science and Engineering R

journal homepage: www.elsevier.com/locate/mser

Electromigration in submicron interconnect features of integrated circuits

H. Ceric [a,b,*], S. Selberherr [b]

[a] Christian Doppler Laboratory for Reliability Issues in Microelectronics at the Institute for Microelectronics, Austria
[b] Institute for Microelectronics, TU Wien, Gußhausstraße 27-29, 1040 Wien, Austria

ARTICLE INFO

Article history:
Available online 29 October 2010

Keywords:
Electromigration
Reliability
Modeling
Simulation
Interconnect

Abstract: Electromigration (EM) is a complex multiphysics problem including electrical, thermal, and mechanical aspects. Since the first work on EM was published in 1907, extensive studies on EM have been conducted theoretically, experimentally, and by means of computer simulation. Today EM is the most significant threat for interconnect reliability in high performance integrated circuits.

Over years, physicists, material scientists, and engineers have dealt with the EM problem developing different strategies to reduce EM risk and methods for prediction of EM life time. During the same time a significant amount of work has been carried out on fundamentally understanding of EM physics, of the influence of material and geometrical properties on EM, and of the interconnect operating conditions on EM. In parallel to the theoretical studies, a large amount of work has been performed in experimental studies, mostly motivated by urgent and specific problem settings which engineers encounter during their daily work. On the basis of accelerated electromigration tests, various time-to-failure estimation methods with Blacks equation and statistics have been developed. The big question is, however, the usefulness of this work, since most contributions about electromigration and the accompanying stress effects are based on a very simplified picture of electromigration.

The intention of this review paper is to present the most important aspects of theoretical and experimental EM investigations together with a brief history of the development of the main concepts and methods. We present an overview of EM models from their origins in classical materials science methods up to the most recent developments for submicron interconnect features, as well as the application of ab initio and first principle methods. The main findings of experimental studies, important for any model development and application, will also be presented.

© 2010 Elsevier B.V. All rights reserved.

Contents

1. Introduction . . . 54
 1.1. The electromigration induced failure . . . 54
 1.2. The history . . . 54
 1.3. The physics of electromigration . . . 55
2. Experimental studies . . . 56
 2.1. The impact of mechanical stress . . . 57
 2.2. The impact of microstructure . . . 58
  2.2.1. Texture distribution . . . 58
  2.2.2. Grain size distribution . . . 58
 2.3. The impact of interfaces . . . 58
  2.3.1. The barrier layer/copper interface . . . 58
  2.3.2. The Etch stop/copper interface . . . 58
 2.4. Empirical and semi-empirical studies . . . 59
  2.4.1. Extrapolation of time-to-failure . . . 59
  2.4.2. Estimation of void growth time . . . 59
3. Electromigration modeling . . . 60
 3.1. Material transport prior to void nucleation . . . 60

* Corresponding author at: Christian Doppler Laboratory for Reliability Issues in Microelectronics at the Institute for Microelectronics, Austria. Tel.: +43 1 58801 36032; fax: +43 1 58801 36099.
E-mail address: Ceric@iue.tuwien.ac.at (H. Ceric).

0927-796X/$ – see front matter © 2010 Elsevier B.V. All rights reserved.
doi:10.1016/j.mser.2010.09.001

3.2. The anisotropy of elastic properties . . . 65
3.3. Stress induced anisotropy of electromigration . . . 66
3.4. Grain boundary movement . . . 69
3.5. Void nucleation . . . 70
3.6. Void evolution . . . 70
3.7. Integration of atomistic and continuum-level models . . . 74
3.7.1. Parametrization of continuum-level models . . . 74
3.7.2. Molecular dynamics of electromigration . . . 75
3.7.3. EM force calculation in grain boundary . . . 76
3.8. Usage scenarios for simulation . . . 76
4. Electromigration simulation studies . . . 77
4.1. Electromigration in redundant vias . . . 77
4.2. Stress-dependent electromigration . . . 79
4.3. Electromigration statistics . . . 79
5. Some special approaches . . . 82
5.1. The atomic flux divergence approach . . . 82
5.2. Electromigration stress evolution in microstructure . . . 83
5.3. The driftless electromigration theory . . . 84
6. Summary . . . 84
Acknowledgements . . . 84
References . . . 84

1. Introduction

When a sufficiently strong electric current is passed through a metal interconnect, a diffusive motion of impurities and/or vacancies takes place in a direction along or opposite to the current flow. This phenomenon is called electromigration (EM). The technological interest in EM arises from its manifestation as a cause of failure in integrated circuits.

1.1. The electromigration induced failure

The density of on-chip interconnects increases from generation to generation of modern integrated circuits. This requires a decrease in both interconnect width and thickness and consequently the operational current densities increase, cf. Fig. 1. The ever smaller interconnects now pose a significant delay to signal propagation in a chip and are also much more susceptible to process defects as well as reliability issues. In Fig. 2 we can see a SEM micrograph of a typical interconnect stack showing the density and complexity of these structures [1].

EM failures in copper interconnects occur mainly by void growth at the cathode end of the line. With continuing void growth the line resistance increases, eventually leading to failure of the line. The corresponding failure times usually follow a lognormal distribution with the median lifetime depending on the quality of the interface, which controls the mass transport.

1.2. The history

Electromigration has been for a long time only of an academic importance. The earliest observation can be traced back to 1861 when Gerardin observed EM in lead [3]. Next was the work of Sakupy in 1907 [4], who studied mass transport of impurities in molten metals. Sakupy was also the first to use the term "electron wind". The technological interest for EM started in 1966, when IBM, Fairchild, Motorola, and Texas Instruments independently observed failures in integrated circuits, which could not be explained. At this time EM surprised and briefly threatened the existence of the integrated circuit industry [5]. In the following decades the development of new interconnect technologies was determined by the following factors:

- manufacturability
- the complexity of integrated circuits
- resistivity and power-loss reduction
- stress and EM reliability

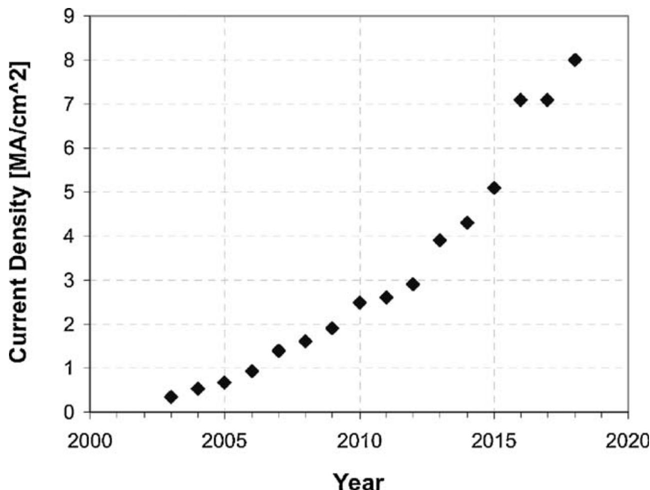

Fig. 1. The current density as a function of time [2] (courtesy of Dr. M. Hauschield).

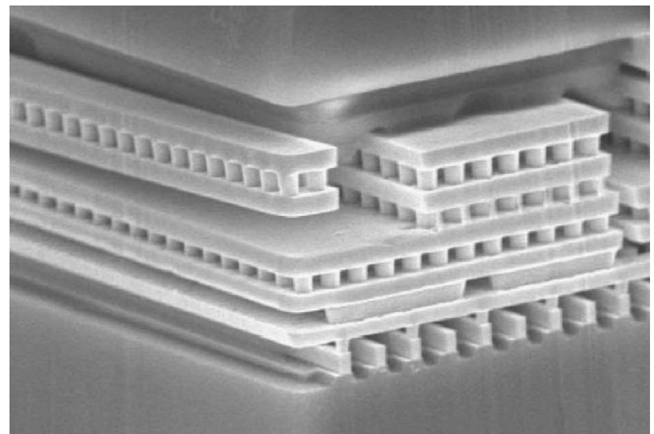

Fig. 2. The typical multilayer interconnect (courtesy of Dr. P. R. Justison) [1].

The introduction of aluminum as interconnect metal was motivated by its low resistivity and low costs. The analysis of EM in aluminum has shown that grain boundaries are the main problem, since they act as high diffusivity paths. The dynamics of the new developments was determined by the emergence of new reliability concerns. In 1970s an incorporation of copper in aluminum-based interconnects (IBM) became a common praxis, because the alloy copper atoms block the fast diffusivity paths at grain boundaries. At that time the general importance of the microstructure was recognized and the search for other alloys began.

With ongoing miniaturization of electronic devices, aluminum-based interconnects with small cross-sections were found to be unable to meet the circuit speed requirement (around the late 1990s) due to their higher electrical resistivity. Copper was proposed, as replacement which has the second lowest resistivity besides silver [6]. The general efforts to implement copper-based interconnects were accelerated after IBM and Motorola announced in 1997 to integrate copper in CMOS technology [7]. In the late 1980s and 1990s the use of complex stacking metalizations and the transition into deep submicron dimensions took place [8].

Today the most common method for designing fine geometries is the dual-damascene technique. Interconnects are made by electrodepositing the material in the vias at the same time as in the trenches. The metal is deposited into the vertical (via) and horizontal (trench) interconnections in one step, so that no interfacial film can form between them.

1.3. The physics of electromigration

In the context of solid-state physics theoretical studies of EM are focused on describing the various contributions to the main driving force. In a simple picture the driving force is split into two contributions: The first arises from the direct action of the external field on the charge of the migrating ion ("direct force"), the second from the scattering of the conduction electrons by the impurity or point defect under consideration ("wind force").

$$\vec{F} = \vec{F}_{direct} + \vec{F}_{wind} = (Z_{wind} + Z_{direct})e\vec{E} = Z^{*}e\vec{E} \tag{1}$$

Z^{*} is called the effective valence of the defect, which is the sum of wind Z_{wind} and direct valence Z_{direct}, e is the elementary charge assumed to be positive throughout this article, and $\vec{E}$ is the macroscopic (space-averaged) electric field.

Until 1962 there was a common belief that Z_{direct} was equal to the bare valence of the ion. It was assumed that at most a small deviation from that value could arise from the electrons in the metallic environment of the ion. In 1962 Bosvieux and Friedel [9] predicted a complete cancellation of the direct force due to screening effects, so that only the wind force would remain. With this result a long lasting controversy was born. The matter was hard to be decided by experiments and a satisfactory theoretical answer was lacking as well. The controversy ended in 1985, when a consensus was reached based on numerical calculations showing that the screening was 25% or less [10].

The first to derive an expression for the wind force acting on a point defect was Landauer in 1954 and this result is presented in an unpublished IBM memorandum. Landauer recognized that the local electric field is not equal to the macroscopic electric field, as it contains contributions from electron pile-up due to scattering by point defects.

The first published models, describing the interaction between conduction electrons carrying the electric current and the migrating ion, are the semiclassical ballistic models of Fiks [11] and Huntington and Grone [12]. They make the rather arbitrary assumption that electrons are decoupled from the lattice and that they are scattered by point defects alone. The scattering electrons lose their momentum to a point defect, which leads to an increase of the point defect's momentum $\vec{M}$. The rate of this momentum increase is equal to the average electron wind force $\vec{F}_{wind}$.

$$\vec{F}_{wind} = \frac{1}{C_d}\frac{d\vec{M}}{dt} = \frac{1}{C_d}\int \hbar(\vec{k} - \vec{k}')W(\vec{k}, \vec{k}')\,f(\vec{k})(1 - f(\vec{k}'))\,d\vec{k}\,d\vec{k}' \tag{2}$$

C_d is the point defect concentration, $\vec{k}$ is the wave vector of the electrons and $W(\vec{k}, \vec{k}')$ the transition probability per unit time that the electron in state $\vec{k}$ will jump to state $\vec{k}'$ by virtue of its interaction with the point defect, and $f(\vec{k})$ is the shifted Fermi–Dirac distribution function. Furthermore, Huntington and Grone [12] assume that, in the case that the external field is switched off, the distribution function $f(\vec{k})$ decays to its equilibrium value $f_0(\vec{k})$ in an exponential manner with the time constant τ. By taking into account $\vec{v} = \hbar\vec{k}/m_0$, (2) is transformed into

$$\vec{F}_{wind} = \frac{m_0}{4\pi^3\tau C_d}\int \vec{v}\,f(\vec{k})\,d\vec{k}. \tag{3}$$

The expression for the current density $\vec{J}$ is [13]

$$\vec{J} = -\frac{e}{4\pi^3}\int \vec{v}\,f(\vec{k})\,d\vec{k}, \tag{4}$$

and from (3) considering the external field $\vec{E}$ and conductivity σ one obtains

$$\vec{F}_{wind} = -\frac{\sigma m_0}{\tau C_d}\vec{E}. \tag{5}$$

In free-electron-like metals the wind-force contribution is expected to be dominant.

The ballistic model cannot be extended beyond the free-electron approximation. First, the momentum of a Bloch electron is not equal to $\hbar\vec{k}$ and second, for more complicated cases such as the scattering by clusters of atoms or by atomic-vacancy complexes, the momentum transfer must be partitioned among defects and lattice.

The first fully quantum-mechanical theory of the EM wind force was provided by Bosvieux and Friedel [9]. They were also the first to calculate the electron wind force as rising from the interaction of a moving gas of free electrons with a stationary point defect. The guiding principle is the Born–Oppenheimer adiabatic approximation [14], which states that, since the ions are so much heavier than the electrons, the ions may be considered to be perfectly fixed in position as they interact with the electrons. Bosvieux and Friedel [9] start their treatment by writing the Hamiltonian for a system of N particles

$$H = -\hbar\sum_{i=1}^{N}\frac{\Delta_i}{2m_i} + V(\vec{r}_1, \ldots, \vec{r}_i, \ldots, \vec{r}_N), \tag{6}$$

denoting its eigenstates as $\psi_0,\ \psi_1,\ \ldots$ and eigenenergies as $\mathcal{E}_0, \mathcal{E}_1, \ldots$.

The $V(\vec{r}_1, \ldots, \vec{r}_i, \ldots, \vec{r}_N)$ is the intrinsic, native potential of the metal. When the external electric field $\vec{E}e^{at}$ is switched on adiabatically, this native field is perturbed by the potential

$$\delta V = e\vec{E}e^{at}\left(\sum_j \vec{r}_j - \sum_k Z_k\vec{R}_k\right). \tag{7}$$

The wave function $\psi(\vec{r}_0, \vec{r}_1, \ldots, \vec{r}_N)$ for the particle system is then defined by the time dependent Schrödinger equation.

$$i\hbar\frac{\partial\psi}{\partial t} = (H + \delta V)\psi \tag{8}$$

The driving force on the lattice atom is given by

$$\vec{F} = -\langle\psi|\nabla_{\vec{r}}(V + \delta V)|\psi\rangle. \tag{9}$$

In order to obtain ψ, first order perturbation theory [14] can be used.

$$|\psi\rangle = |\psi_0\rangle + \sum_{n\neq 0} \frac{\langle \psi_n|\delta V|\psi_0\rangle}{\mathcal{E}_0 - \mathcal{E}_n} |\psi_n\rangle \tag{10}$$

Before the external field is turned on, all the particles (electrons and ions) are in a pure quantum state $\psi_0\rangle$. On the basis of (6)–(10) the force expression is obtained [9,15].

$$\vec{F} = Z_i e\vec{E} + \frac{i}{\hbar}\int_0^\infty e^{-at}\langle\psi_0|[e^{iHt/h}(\nabla_{\vec{r}}V)e^{-iHt/h}\, e\vec{E}\cdot\sum_j \vec{r}_j]|\psi_0\rangle\,dt \tag{11}$$

The second term of Eq. (11) consists of two contributions, the first one is identified as the wind force and the second one implies some screening of the bare direct force $Z_i e\vec{E}$ [15].

A more sophisticated treatment of the wind force based on Kubo's linear response theory [16] was carried out by Kummar and Sorbello [17]. They start with the equation of motion for the expectation value of the momentum $\vec{P}$ and write the total force on the atom as [14]

$$\vec{F} = \frac{d\langle\vec{P}\rangle}{dt} = -\frac{i}{h}\langle[\vec{P},(H+V+\delta V)]\rangle, \tag{12}$$

where V is the electron-point defect interaction. By inserting (7) we obtain

$$\vec{F} = Z_i e\vec{E} - \langle\nabla_{\vec{R}}V\rangle. \tag{13}$$

The quantity $\langle\nabla_{\vec{R}}V\rangle$ is exactly the electrostatic force exerted on the point defect by the electron charge density. It contains both electron wind as well as the contribution from local screening of the local field.

In the linear response theory we observe a statistical operator ρ for a system of identical particles. If one assumes that this system can be in different states defined by wave functions $\Psi^1, \Psi^2, \ldots$ and that the probability that the particle system is in a state defined by a wave function, Ψ^i is ϱ_i. The statistical operator ρ is then defined as

$$\rho = \sum_i |\Psi_i\rangle\varrho_i\langle\Psi_i|. \tag{14}$$

Now one can write an expectation value for an arbitrary operator A as

$$\langle A\rangle = \mathrm{Tr}(\rho A). \tag{15}$$

If the Hamiltonian of the system H is perturbed by a time-dependent operator $Be^{-i\omega t}$, the new expectation value is given by Kubo's expression

$$\langle A\rangle' = \langle A\rangle - \frac{i}{\hbar}\int_0^\infty e^{i\omega t}\mathrm{Tr}(\rho[A(t),B])\,dt, \tag{16}$$

where $A(t)$ is a Heisenberg picture of the operator A, [18].

$$A(t) = e^{iHt/h}Ae^{-iHt/h} \tag{17}$$

The Heisenberg picture is part of a general concept in which operators become time-dependent and states time-independent.

Now we set

$$A \to \nabla_{\vec{R}}V, \quad B \to e\vec{E}\sum_j \vec{r}_j \tag{18}$$

and using (16) and (17), (13) transforms into

$$\vec{F} = Z_i e\vec{E} - \frac{i}{\hbar}e\vec{E}\int_0^\infty e^{i\omega t}\mathrm{Tr}(\rho[\nabla_{\vec{R}}V(t),\sum_j \vec{r}_j])\,dt. \tag{19}$$

The linear force expression (19) is exact and holds for a very general system, since no restrictions are assumed for a system Hamiltonian. Both driving force expressions (11) and (19) are equivalent, as has been shown in extensive studies by Lodder [11,15,19].

Sorbello also calculated the wind force for vacancies and impurities for virtually all free-electron-like metals within the pseudopotential formalism [20].

Besides the perturbation theories of Bosvieux and Friedel, and Kumar and Sorbello, there is a third quantum-mechanical EM theory developed by Sham [21] and Schaich [22]. The perturbation theory and the pseudopotential theory are not expected to be valid, when we have to deal with a strong scatterer in a point defect complex. But in reality the region containing the migrating atom contains more than one scattering center and electrons will suffer collisions with all these centers.

As a basis for studying situations with multiple and strong scatterers, Sham [21] and Schaich [22] provided the very general expression for the wind force

$$\vec{F}_{wind} = -\sum_{\vec{k}}\delta f(\vec{k})\int|\psi(\vec{k})|^2\nabla_{\vec{R}}V\,d\vec{r}, \tag{20}$$

where V is the electron-point defect interaction potential, $\delta f(\vec{k})$ is the perturbed electron-distribution function caused by the applied field

$$\delta f(\vec{k}) = e\tau\vec{E}\cdot\vec{v}\,\frac{\partial f(\varepsilon)}{\partial\varepsilon}, \tag{21}$$

and $\psi(\vec{k})$ is the electron scattering wave function for an electron incident upon the defect complex. The expression (20) can be heuristically derived from the general Feynman–Helmann [23] form for the force

$$\vec{F} = -\int n(\vec{r})\nabla_{\vec{R}}V\,d\vec{r}, \tag{22}$$

where $n(\vec{r})$ is the electron density. We can now simply assume that the electron density is the density which corresponds to each scattering state summed over all occupied scattering states

$$n(\vec{r}) = \sum_{\vec{k}}\delta f(\vec{k})|\psi(\vec{k})|^2 \tag{23}$$

By substituting (23) in (22) we immediately obtain (20).

The effective valence Z^* can be measured by various methods. From its temperature or resistivity dependence it is sometimes possible to gain information both on the direct force and the wind force [24]. Ab initio results for the wind valence in a number of FCC and BCC metals are presented by Lodder and Dekker in [25]. They calculated both positive and negative wind valences, cf. Table 1, as result of the detailed electronic structure of the system. Apparently, Z_{wind} appears to be rather small for quite a number of metals, which means that a measurement of the effective valence Z^* will be valuable in the determination of the direct valence.

2. Experimental studies

The development of new interconnect technologies always requires a development of devices, methods, and procedures for

Table 1
Calculated Z_{wind} and measured Z^* at 0.9× melting temperature [25].

FCC			BCC		
System	Z_{wind}	Z^*	System	Z_{wind}	Z^*
Al	−3.11	−3.4	V	0.99	
Al(Cu)	−5.29	−6.8	Nb	0.76	1.3
Al(Pd)	−8.71		Ta	0.35	
Al(Si)	−24.26		Nb(Y)	0.95	
Cu	−3.87	−5	Nb(Zr)	0.93	
Ag	−3.51	−8	Nb(Mo)	0.85	

the estimation of EM lifetime. This is a very demanding task due to the small dimensions of state of the art integrated circuits (ICs) and the variety of materials employed. A vast number of circuit elements must be evaluated in terms of a multitude of possible failure mechanisms. Although there is no generally accepted industry standard, competitive reliability targets of chip failure rates have been in the order of one per thousand throughout the anticipated interconnect lifetime of 10–15 years [26].

In order to study interconnect failure behavior the usage of accelerated EM tests is necessary, in which failure times are commonly less than 1000 h. As indicated by Black's equation [27], the life time of an interconnect can be reduced by either increasing the current density or by increasing the diffusivity. The latter is done by increasing temperature. Current densities used for tests are 5–45 mA/μm^2 and temperatures 170–350 $^\circ$ C [28] for copper based technologies.

The EM tests are carried out using simple structures and operating conditions which accelerate EM failure. One of the goals is the identification of failure mechanisms and their impact on the interconnect properties [8]. The results of EM tests have to be related to the operation of real devices under realistic usage conditions. It is known that important causes of EM are microscopic and macroscopic flux divergences, hence, a test structure has to be suitable for reproducing such divergences [26]. Since EM experiments are conducted at higher current densities and temperatures compared to operating conditions, extrapolations are needed to assess reliability at operating conditions. In addition, only a limited number of interconnect structures are tested, whereas often hundreds of millions of interconnects exist on a chip. Therefore, the extrapolation needs to take into account, how to assess on-chip reliability from the EM-tested sample structures.

One of the first standard structures used to study EM was Blech's structure [29–31]. In this structure an interconnect is deposited directly over a thin redundant layer of material with higher resistivity, for example aluminum over titanium nitride or copper over tungsten. The EM induced movement of material is then visible from above and a direct measurement of the physical drift rate is possible.

The results of life time experiments are regularly expressed as the mean time-to-failure and the standard deviation of a lognormal distribution of nominally identical samples.

An originally used test structure is the NIST (National Institute of Standards and Technology) structure, which is composed of a straight metal strip with four terminals for Kelvin resistance measurements. A length of 800 mm is suggested to prevent short length effects and avoid thermal interferences between the pads [32]. The length and width of the end-contact segments and voltage taps are defined in order to reduce the heat dispersion along these paths, thus improving the temperature profile of the test line. The major flaw of the NIST test structure is that there are no significant macroscopic flux divergences and, therefore, experiments always indicate unrealistically long times-to-failure. Another standard test structure is the SWEAT (Standard Wafer-level Electromigration Acceleration Test) structure. It was proposed in 1985 [33] for a very rapid characterization technique capable of giving information about the quality of a metalization process in less than 15 s. There exist also several others tests, e.g. BEM (Breakdown Energy of Metal) [34], WIJET (Wafer-level Isothermal Joule heated Electromigration Test) [35], TRACE (Temperature-ramp Resistance Analysis to Characterize Electromigration) [36], assorted pulsed-current techniques [37], and noise measurements [38]. The line-via test structure is the most widely used today, especially for copper-based metalization. A typical line-via EM test structure is shown in Fig. 3.

2.1. The impact of mechanical stress

There are three major sources of mechanical stress in passivated interconnect lines. The first is the thermal stress, resulting from the difference in thermal expansion between the passivation and metal upon cooling from high deposition temperatures. Metalization processing can expose an integrated circuit to temperatures of more than 500 °C. The second source of stress is non-equilibrium film growth. As wafer curvature measurements have shown this source of stress is even more important than the thermal stress. The third major source of stress is EM itself.

Although the measurements significantly contribute to the understanding of thin film stresses, they are, in most cases, limited to simple test structures. Furthermore, the detailed stress distribution within a material cannot be experimentally determined.

The evolution of mechanical stress in interconnect lines depends on whether or not vacancies can be created or annihilated such that their equilibrium is maintained. For mechanical stresses to develop, there must be both a volume expansion or contraction of the line with respect to the surrounding material and a mechanical constraint applied by the surrounding material. As atoms exchange place with vacancies and travel towards the anode end of the line, there is a flow of vacancies towards the cathode end. In the absence of vacancy sources and sinks, this would result in a vacancy supersaturation on the cathode end and a deficiency at the anode end. Since the replacement of an atom with a vacant site produces a small relaxation in the surrounding lattice, there would be a net volume contraction at the cathode and expansion at the anode.

For the dual-damascene technology high tensile stress at the interfaces, where one can expect defects is critical. The conditions for EM and stressmigration can work both in order to increase this local tensile stress or act against each other in order to reduce the stress.

The choice of passivating film material and corresponding process technology causes tensile or compressive stress in the interface between the passivating film and the interconnect metal. Interfacial compressive stress diminishes EM along interfaces by reducing the diffusivity [26]. However, numerous experimental observations have shown [39] that tensile stress in the interface

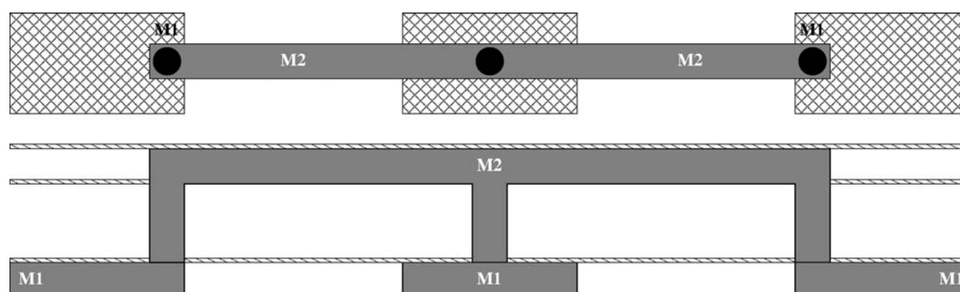

Fig. 3. Typical dual-damascene via test structure.

increases the possibility of failure. Increased thickness and rigidity of the capping layer prevent relaxation of both thermal and EM induced stress, which results in dielectric cracking and metal extrusion.

2.2. The impact of microstructure

The interconnect microstructure depends on many parameters such as the core material deposition technique, barrier material types, barrier material deposition technique, copper seed layer deposition technique and thickness, and line width. As an example, for a given line width, the grain size may differ significantly, when the copper deposition technique changes from CVD to electroplating. The grain size distribution can be precisely determined using AFM (Atomic Force Microscopy) and EBSD (Electron Back Scatter Diffraction) [40], the texture distribution with XRD (X-Ray Diffraction) and EBSD [41]. Furthermore, advanced experimental techniques enable a direct observation of the influence of layout geometry on the microstructure.

2.2.1. Texture distribution

Thin metal films generally have a strong {1 1 1} sheet texture which is a function of the deposition process and the geometry of the film. It has been observed over the past decade that the texture has a significant effect on EM performance, but the reason for the effect is rather subtle. The effect of texture remains approximately the same both for thick interconnects with complex microstructures and for bamboo and near-bamboo interconnects [42]. This indicates a significant surface effect of the texture, which has been extensively investigated in [43].

In order to study the texture effect independently from the grain structure effect, it is necessary to apply various barrier and seed layers, deposition techniques, and line patterning methods. The current density exponent in Black's equation [27] is about 2 for both {1 1 1} and {2 0 0} CVD copper lines, but the time-to-failure of {1 1 1} CVD copper lines is about four times longer than that of {2 0 0} CVD copper lines under the same current density [44]. The cause of a longer lifetime of {1 1 1} CVD copper lines over {2 0 0} CVD copper lines is most probably the smaller variance of the grain boundary tilting distribution resulting in slower atomic diffusion.

The growth of voids nucleated in {1 1 1} grains is rather uniform [45], but if they move into a non-{1 1 1} grain, the void geometry changes dramatically. Frequently, the voids become very narrow and nearly slit-like, spanning the entire interconnect and causing a failure without an actual increase in volume.

Very extensive studies on the interplay between geometry features, microstructure, and void evolution have been carried out by the group of Prof. Carl Thompson. The role of microvoids, caused by thermal processing, in EM failure build-up was investigated in [46]. It has been clearly shown that wider interconnects do not lead to improved EM behavior, when the dual-damascene process itself produces microvoids in the copper bulk. Another work illuminates the role of texture of the grains surrounding voids [47]. In estimating interconnect failure times, the period of void evolution is critical, however, the behavior of evolving voids is difficult to predict. Particularly the dependence of void evolution on different grain textures is up to now not well understood. In this sense, the systematical study provided in [47] is very helpful for developing void evolution models.

2.2.2. Grain size distribution

Since atoms are more loosely bound at grain boundaries than in the lattice, atoms migrate along grain boundaries more easily than through the lattice. Therefore, the EM failure rate should depend on the grain size of the metallic thin film. Such a dependence is well documented for aluminum interconnects, however, the dependence is found to be less pronounced in copper interconnects. The reason is probably that EM along interfaces is dominant in copper interconnects. However, the difference in EM performance between interconnect lines with large and small grains can clearly be seen. Electroplated copper in the dual-damascene structures has a significantly larger grains than CVD copper line resulting in its longer EM life-time compared with CVD copper line [44].

Walton et al. [48] argue, based on the model of secondary grain growth, that the length of the grain sections is likely to be exponentially distributed. They give for the distribution of grain lengths

$$G(L) = 1 - e^{-(M/L)}, \tag{24}$$

where M is the average grain size and $G(L)$ is the probability that a particular grain is smaller than L. Arzt and Nix [49] give essentially the same formula, although based on different physical arguments.

2.3. The impact of interfaces

Since the introduction of copper interconnects, their surface and interface EM properties have been extensively studied by many researchers. However, the focus was on EM lifetime tests and the results are significantly affected by various factors such as microstructure, processing, and structure layout. The copper interconnect in modern dual-damascene technology is completely embedded in a barrier layer and in a capping layer. For both the capping and the barrier layer the quality of adhesion is of crucial importance. The adhesion quality can be influenced by the choice of processes and materials, for example, the following combinations have been extensively investigated: Cu/TiW, Cu/SiO_2, TiW/Cu/TiW, W/Cu/TiW, SiO_2/Cu/TiW [50]. Weak bonding between copper and the capping layer not only enhances EM prior to void nucleation but also speeds-up void evolution and growth. Observations showed that an epitaxy-like (e.g. non-interrupted array of parallel lattice planes) transition between copper and the capping layer strengthens the copper/capping bonding [51].

2.3.1. The barrier layer/copper interface

The most commonly used barrier layer material is tantalum (Ta). The adhesion between tantalum and copper is quite good as long as the surface is not oxidized. Strong adhesion clearly retards diffusion along the barrier layer [39]. Actually, interconnects with tantalum layers inhibit EM along the barrier layer interfaces in a manner similar to that of an aluminum/oxide interface. The relatively high activation energy of 2.1 eV [28] makes EM along the interface between copper and the barrier layer less critical.

2.3.2. The Etch stop/copper interface

The interface between copper and the capping layer is known to be the dominant diffusion pathway in dual-damascene interconnects [52]. The properties of this particular interface play therefore a key role for EM. SiN- and SiC-based films are widely used as capping materials for copper interconnects. It has been published in several studies [2] that the EM lifetime depends on the adhesion behavior, i.e. the sticking coefficient between the capping layer and the copper surface. Good adhesion and hence large EM lifetimes are enabled by a tightly bonded interface which suppresses the migration along this pathway. In contrast, a poorly adhering interface would correspond with enhanced diffusion and lower EM lifetimes [52]. One of the major tasks during process development is to find capping layer materials as well as pre-clean and deposition techniques that yield good interface adhesion to obtain adequate EM performance. Recently, numerous experiments have shown that the best results are obtained, when an adherent metallic layer, such as electroless CoWP, is applied to the surface before deposition of the interlevel dielectric. In such a case,

a very thin (∼10 nm) layer is sufficient to completely stop all interfacial diffusion. This is especially valuable in narrow lines, where a bamboo copper grain structure exhibits bulk-like activation energies for failure, which makes this system essentially immortal with respect to EM failure. Because the copper interfaces are such an easy pathway for diffusion, one of the important properties of a capping layer is, that it must be a good diffusion barrier to oxygen. Any oxygen which is allowed to diffuse to the copper surface will reduce the adhesion consequently leading to an increase in diffusion and a reduction in EM lifetime. Poor cleaning practice prior to the application of a capping layer has also been found to degrade the interconnect lifetime.

2.4. Empirical and semi-empirical studies

2.4.1. Extrapolation of time-to-failure

The statistical character of EM necessitates to carry out EM experiments on a number of test structures. Normally, at least 20 test structures are used which are exposed to the same stressing conditions. The failure is defined as a pre-defined increase of the measured relative resistance $\Delta R/R$. Depending on the application, the resistance increase is chosen to be 5, 10, or 20%. During the test the resistance of every single structure is observed and registered. For a statistical description of the measured individual time-to-failure ($t_{F,i}$) of each sample a lognormal distribution is well established. It is characterized by the mean time-to-failure ($\bar{t}_F$) and the standard deviation σ. The mean time-to-failure is calculated as the average of the logarithmic times-to-failure.

$$\ln(\bar{t}_F) = \frac{1}{N}\sum_{i=1}^{N}\ln(t_{F,i}) \tag{25}$$

N is the number of test structures. The standard deviation is obtained as

$$\sigma = \sqrt{\frac{1}{N-1}\sum_{i=1}^{N}(\ln(t_{F,i}) - \ln(\bar{t}_F))^2}. \tag{26}$$

The cumulative failure frequency of the i-th structure is given by

$$h_i = \frac{i-0.3}{N+0.4}. \tag{27}$$

The data points ($t_{F,i}$, h_i) are sorted in order of increasing failure time and presented in cumulative failure diagrams (Fig. 4). For the probability density function PDF of the lognormal distribution holds

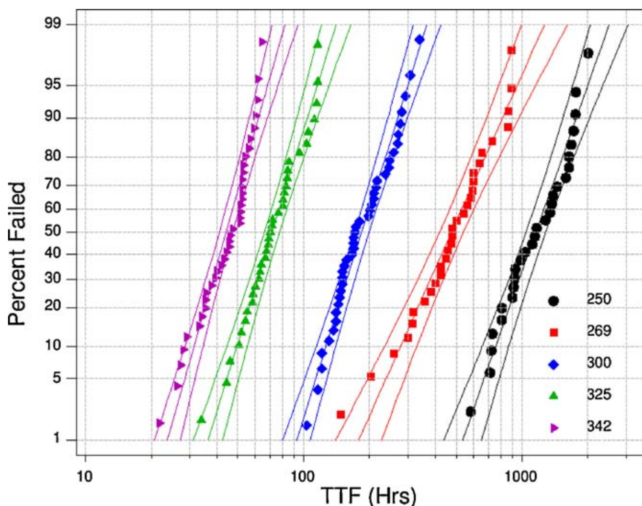

Fig. 4. Example of a lognormal EM failure plot for a structure tested in a range of temperatures from 250 to 342 °C (courtesy of Dr. P. R. Justison) [1].

$$\mathrm{PDF}(t) = \frac{1}{\sqrt{2\pi}\sigma t}\exp\left(-\frac{(\ln(t) - \ln(\bar{t}_F))^2}{2\sigma^2}\right). \tag{28}$$

The cumulative distribution function CDF(t) gives the number of failures until some defined time t.

$$\mathrm{CDF}(t) = \int_0^t \mathrm{PDF}(\tau)\,d\tau = \Phi\left(\frac{\ln(t) - \ln(\bar{t}_F)}{\sigma}\right) \tag{29}$$

$$\Phi(z) = \frac{1}{\sqrt{2\pi}}\int_{-\infty}^{z}\exp\left(-\frac{y^2}{2}\right)dy \tag{30}$$

The goal of accelerated EM tests is to obtain the mean time-to-failure $\bar{t}_F$ and the standard deviation σ defined by the current density I_{str} and temperature T_{str}, which are significantly higher than the expected operating current density I_{op} and operating temperature T_{op}. Once $\bar{t}_F$ and σ are determined, the time-to-failure t_F under operating conditions is calculated as [53,54]

$$t_F = \bar{t}_F\left(\frac{I_{str}}{I_{op}}\right)^n \exp\left[\frac{E_a}{k}\left(\frac{1}{T_{str}} - \frac{1}{T_{op}}\right) + \Phi^{-1}(s)\,\sigma\right]. \tag{31}$$

for any given percentage s of cumulative failure. Eq. (31) is based on the work of Black [27]. The parameter n represents the current density exponent which is experimentally determined and Φ^{-1} is the inverse function to Φ.

2.4.2. Estimation of void growth time

Void evolution represents the period of EM failure development with the most dramatic changes of interconnect resistance and it has been intensively studied with a combination of empirical and semi-empirical methods. As an illustration we present an analysis of void growth in a single-damascene structure (cf. Fig. 5). The basis for semi-empirical modeling is a simple expression for the mass flux J_m

$$J_m = C_a\frac{\delta}{h}\frac{D_a}{kT}Z^* e\rho J. \tag{32}$$

Here, C_a is the atomic concentration, δ is the width of the diffusion path along the interface, h is the interconnect line height, D_a is the self-diffusion coefficient, ρ is the resistivity, and J is the current density.

The mass flux through an interconnect can also be described as

$$J_m = \frac{N_a}{A\Delta t}, \tag{33}$$

where A is the cross-section of the interconnect and N_a is the number of atoms moving through the interconnect cross-section A in time Δt.

Due to geometrical reasons (cf. Fig. 5) the moving atoms are not replenished and leave a void of volume ΔV behind. The number of atoms which were contained in this void are

$$N_a = \frac{\Delta V}{\Omega_a}, \tag{34}$$

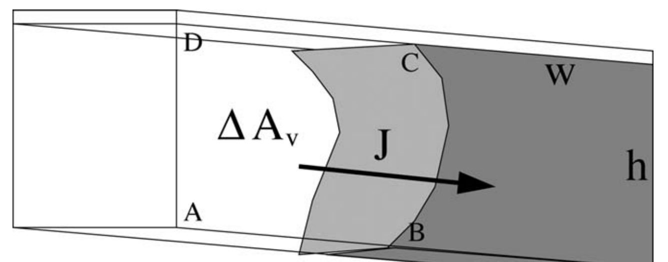

Fig. 5. Part of the single-damascene interconnect used for analysis.

where Ω_a is the atomistic volume. Combining Eqs. (32), (33), and (34) we obtain

$$\frac{\delta}{h}\frac{D_a}{kT}Z^* e\rho J = \frac{\Delta V}{A\Delta t}, \quad (35)$$

and by setting $J = I/A$

$$\Delta t = \frac{kTh}{D_a Z^* e\rho I\delta}\Delta V. \quad (36)$$

Expression (36) is commonly used for estimation of the void growth time [7,55–57]. One of the most interesting statistical investigations on the EM failure behavior of single-damascene copper interconnect structures was performed by Hauschield et al. [56,57]. The author sets $\Delta V = w\Delta A_v$ and $A = wh$ and obtains from (36)

$$\Delta t = \frac{kTA}{D_a Z^* e\rho I\delta}\Delta A_v, \quad (37)$$

where ΔA_v is the void surface which can be measured using scanning electron microscope (SEM) and focused ion beam (FIB) cross-sectioning (in Fig. 5 the surface defined by the points A, B, C, and D), A is the cross-section area of the interconnect, and w is the width of the interconnect (cf. Fig. 5). The derivation of Eq. (37) basically assumes a rectangular void shape defined by two parallel cutting planes (orthogonal to interconnect line) and the barrier and capping layers. Furthermore, during the void evolution the flux along these cutting planes remains constant. These are rather rough assumptions, but, nevertheless, they provide an interesting insight into the statistics of EM failure development. If we additionally assume that the void during its evolution retains the same shape and integrate Eq. (37) up to time t_c, we obtain

$$t_c = qA_c, \quad q = \frac{kTA}{D_a Z^* e\rho I\delta}. \quad (38)$$

Here, A_c is the surface of the void after the time t_c. As the results of experimental void area measurements show, there is indeed a linear dependence between the testing time and the median void area size (Fig. 6) [2]. The expression (38) was also applied by Kang and Shin [58], where a three-dimensional calculation of the electric field and the temperature for a constant voltage load is used in order to determine a critical volume of the rectangular void. After estimating the average current density and average temperature the void growth time is calculated with (38). The relationship (38) allows to study interesting statistical correlations between different types of experiments. In [56,57] the EM tests for a single-damascene copper via were either stopped after a given test time (t-based) or after a certain resistance increase (R-based) and for both kind of experiments the void area statistics are obtained (mean value, standard deviation). Using these extracted statistical features of t-based and R-based experiments artificial distributions of void areas ($A_i^{\text{t-based}}$, $i = 1\ldots500$) and ($A_j^{\text{R-based}}$, $j = 1\ldots500$) are produced. Now, for a single R-based failure criterion (10 %, 20%,. . ., change of interconnect resistance) mean time t_m is calculated. By randomly choosing i and j from two artificially created void area lists a new distribution is obtained

$$t_{ji} = \frac{A_j^{\text{R-based}}}{A_i^{\text{t-based}}}t_m. \quad (39)$$

However, as shown in [56,57], this new distribution has almost the same standard deviation as the original failure time distribution of R-based experiments. Hence, by knowing the statistical properties of a void size distribution, the standard deviance of the failure time distribution can be estimated.

The well presented and carefully studied experimental results together with corresponding semi-empirical models as those presented above are extraordinary useful for development and verification of theoretical models for EM failure.

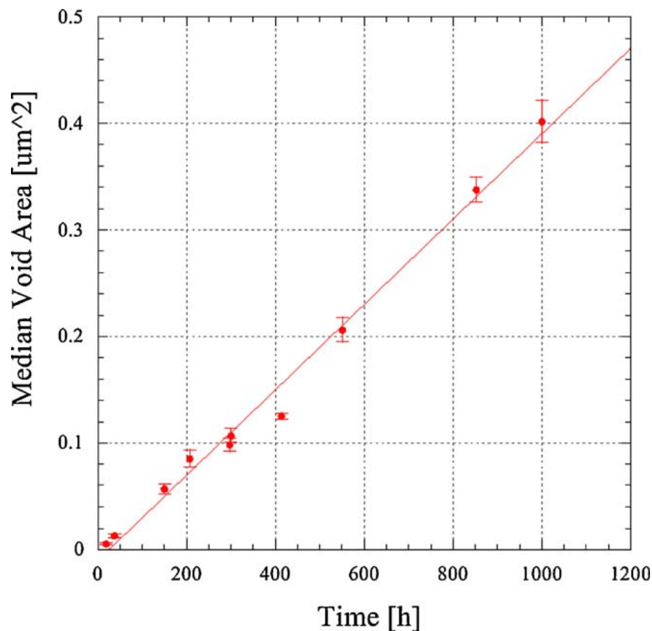

Fig. 6. Median void area as a function of median test time (courtesy of Dr. M. Hauschield) [2].

3. Electromigration modeling

The development of intrinsic voids, which leads to interconnect failure, goes through two distinctive phases. These phases exhibit the different influence on the operating abilities of interconnects and are based on different physical phenomena.

The first phase is the void nucleating phase in which EM generated voids do not exist and a significant resistance change is not observable. The second phase starts, when a void is nucleated and becomes visible in SEM pictures [41]. This is the so-called rapid phase of void development. The void expands from its initial position (nucleation site) to a size which can significantly change the resistance or completely sever the connection. If we denote the void nucleation time with t_N and the void evolution time with t_E, the time-to-failure t_F is

$$t_F = t_N + t_E. \quad (40)$$

The development of a general EM model demands a careful analysis of physical phenomena in both phases of void development.

3.1. Material transport prior to void nucleation

The simple, linear relationship between electric field and EM force (1) can straightforwardly be used to build a continuum EM model. This was done by Wever [59] in 1973, who gives the general phenomenological expression for the molar fluxes $\bar{J}_i$, ($i = 1, \ldots, M$) of M distinguishable components (in original notation).

$$\bar{J}_i = -D_i\left[\text{grad}_x N_i - \frac{F\varrho_e I N_i}{RTm_i f_i^E z_i^*}\right] \quad (41)$$

Here, N_i is the molar fraction of component i, F is the Faraday constant, ϱ_e is the resistivity, I is the current density, R is the Rydberg constant,

$$m_i = \left(\frac{\partial \ln a_i}{\partial \ln N_i}\right)_{p,T}, \quad (42)$$

where a_i is the activity of the component i in the mixture, f_i^E is the correlation factor of "Elektrotransport", and z_i^* is the effective charge [59].

The most widely used model today is the simple semi-empirical model of Black [27]. According to Black the migration rate R_m is proportional to the number of ions which overcome a potential barrier E_a in the metal lattice, which can be expressed as

$$R_m \sim \exp\left(-\frac{E_a}{kT}\right). \tag{43}$$

Furthermore, Black concluded that, if the current density J is increased, the impulse transfer Δp from electrons to atoms is increased.

$$R_m \sim \Delta p \sim J \tag{44}$$

The probability of an electron-atom collision is proportional to the density of conduction electrons n.

$$R_m \sim n \sim J \tag{45}$$

Considering (43), (44), and (45), and the simple assumption that the mean time-to-failure $\bar{t}_f$ is inversely proportional to the migration rate R_m, Black derives the following expression:

$$\bar{t}_f \sim \frac{1}{R_m} \Rightarrow \bar{t}_f = \frac{A}{J^2}\exp\left(\frac{E_a}{kT}\right) \tag{46}$$

Here, A is a constant defined by materials and geometry of an interconnect layout.

Fitting of (46) to experimental data has shown that the current density exponent varies between 1 and 2. A value close to 2 indicates that the void runs through both phases of evolution. A current density exponent closer to 1 indicates that the void existed prior to EM stressing or a large interfacial defect was present.

The theoretical explanation for an exponent value 2 was found by Shatzkes and Lloyd [60]. They discuss the solution of the one-dimensional continuity equation for the vacancy concentration C_v with a perfectly blocking boundary:

$$\frac{\partial C_v}{\partial t} = D_v\frac{\partial^2 C_v}{\partial x^2} - v\frac{\partial C_v}{\partial x}, \quad v = \frac{Z^* e\rho J D_v}{kT} \tag{47}$$

D_v is the vacancy diffusivity. According to Shatzkes and Lloyd [60], the failure will occur, when the vacancy concentration reaches a certain critical value C_{vf} which can be significantly higher than the initial equilibrium value C_{v0}. They found that

$$t_f = \left(\frac{2C_{vf}}{C_{v0}J^2 D_v}\right)\left(\frac{kT}{Z^* e\rho}\right)^2. \tag{48}$$

The vacancy diffusivity is thermally activated.

$$D_v = D_{v0}\exp\left(-\frac{E}{kT}\right) \tag{49}$$

The major shortcoming of the Shatzkes–Lloyd model is that the time scale for failure is too short, e.g. [26], and the effect of stress is not included. The short time scale for failure follows from the absence of any vacancy sinks in the model.

The work of Blech from 1976 which was published in a series of short papers [29–31] led to the introduction of three important concepts: the "Blech Product", the "Blech Length", and the "Blech Condition". While studying the EM induced movement of conductor islands deposited on TiN, Blech found that the drift velocity can be expressed as

$$v_D = \frac{D_a Z^* e\rho J}{kT}. \tag{50}$$

EM moves only one side of the metal island so that its length generally shrinks. When the island shrinks to a particular length l_B ("Blech length") the upstream end stops moving and EM essentially comes to a halt. The parameter called "Blech product" depends on temperature.

$$c(T) = J l_B \tag{51}$$

If the conductor length is less or equal to the Blech length l_B, no EM will occur.

The Blech effect was understood by realizing that in addition to EM also stressmigration in the opposite direction takes place. The driving force of stressmigration is the gradient of the hydrostatic mechanical stress σ. The total vacancy flux in a Blech experiment is then

$$J_v = \frac{D_v C_v}{kT}\left(Z^* e\rho J - \Omega\frac{\partial\sigma}{\partial x}\right). \tag{52}$$

EM vanishes, when the stressmigration equals the EM, e.g. $J_v = 0$. This steady state condition is called the Blech condition.

$$\frac{\partial\sigma}{\partial x} = \frac{Z^* e\rho J}{\Omega} \tag{53}$$

The origin and nature of stress in Blech's work was not clear. Korhonen et al. [61] argues that supersaturation of vacancies cannot be supported in a thin film as assumed by Shatzkes and Lloyd [60].

The transport of vacancies causes a change in local vacancy concentration. Some of these vacancies are deposited on grain boundaries or lattice dislocations [62] and, therefore, grain boundaries and lattice dislocations are regarded as vacancy sinks. Korhonen et al. [61] consider only dislocations as vacancy sinks. By accepting a vacancy a process of dislocation climb is initiated [62], which changes local concentration of lattice sites C_L what in turn induces hydrostatic stress according to Hooke's Law

$$\frac{\partial C_L}{C_L} = \frac{\partial\sigma}{B}, \tag{54}$$

with B as the bulk elastic modulus. On the other hand side the production/annihilation rate of vacancies γ is equal to the negative rate of change of the concentration of lattice sites [63].

$$\gamma = -\frac{\partial C_L}{\partial t} \tag{55}$$

Using (54) and (55) one can write a material balance equation for atoms and vacancies [61].

$$-\frac{\partial J_a}{\partial x} = \frac{\partial C_v}{\partial t} - \gamma = \frac{\partial C_v}{\partial t} + \left(\frac{C_L}{B}\right)\frac{\partial\sigma}{\partial t} \tag{56}$$

The atomic flux J_a is given with the relationship (52).

$$J_a = -\frac{D_a C_a}{kT}\left(Z^* e\rho J - \Omega\frac{\partial\sigma}{\partial x}\right) \tag{57}$$

Eqs. (56) and (57) connect C_a, C_v, and σ but in effect we have only one continuum equation for three unknown functions. Moreover, the model considers only hydrostatic stress, while generally the stress in an interconnect confined by surrounding layers is anisotropic.

In aluminum, grain boundaries are the dominant diffusion paths. This fact is used by Korhonen et al. [61] to argue that, since the grain boundaries are randomly distributed in the interconnect, the stresses in the grain boundaries become equal in all directions (i.e., $\sigma = \sigma_1 = \sigma_2$) in a very short time, so only one stress component is needed in the model (Fig. 7). This equilibration of stress assumes a fast and homogeneous redistribution of atoms. According to [61], the mechanism of vacancy production/annihilation keeps the value of stress closely connected to the vacancy concentration, i.e. these two values are in equilibrium

inside the grain boundaries. This allows the application of an equilibrium relationship

$$C_v = C_{v0} \exp\left(\frac{W_f + \Omega\sigma}{kT}\right), \quad (58)$$

which was originally derived in [62]. W_f is the interaction energy between the vacancy and the stress field, while C_{v0} is the vacancy concentration in the absence of stress. Including some further, but less critical assumptions, the following equation is obtained [61]:

$$\frac{\partial\sigma}{\partial t} = \frac{\partial}{\partial x}\left(\frac{D_a B\Omega}{kT}\left(\frac{\partial\sigma}{\partial x} + \frac{Z^* e\rho J}{kT}\right)\right) \quad (59)$$

Clement [63] studied the Eq. (59) under similar conditions, but he uses a vacancy description.

$$\frac{\partial C_v}{\partial t} - D_v\left(\frac{\partial^2 C_v}{\partial x^2} - \frac{Z^* e E}{kT}\frac{\partial C_v}{\partial x}\right) + \gamma = 0 \quad (60)$$

Eq. (60) can be analytically solved for various cases of initial and boundary conditions [60,61,63,64], however, from a practical point of view, the most important solution is for the situation where the vacancy flux is blocked at both ends of a finite line, i.e.

$$J_v(0,t) = J_v(-l,0) = 0, \quad (61)$$

on the segment $[-l, 0]$, assuming the initial vacancy concentration to be $C_v(x,0) = C_v^{eq}$. In this case the solution of (60) is given in [64] as

$$\nu(\xi,\zeta) = \frac{C_v(x,t)}{C_v^{eq}} = A_0 - \sum_{n=1}^{\infty} A_n \exp(-B_n\zeta + \alpha\xi/2), \quad (62)$$

where

$$A_0 = \frac{C_v(x,\infty)}{C_v^{eq}} = \frac{\alpha \exp(\alpha\xi)}{1 - \exp(-\alpha)} \quad (63)$$

is the steady-state solution and

$$A_n = \frac{16n\pi[1 - (-1)^n \exp(\alpha/2)]}{(\alpha^2 + 4n^2\pi^2)^2} \times \left(\sin(n\pi\xi) + \frac{2n\pi}{\alpha}\cos(n\pi\xi)\right), \quad (64)$$

$$B_n = n^2\pi^2 + \alpha^2/4. \quad (65)$$

For the sake of simplification, we used the substitutions

$$\nu = \frac{C_v}{C_{v0}}, \quad \xi = \frac{x}{l}, \quad \zeta = \frac{D_v t}{l^2}, \quad \alpha = \frac{Z^* eEl}{kT}, \quad (66)$$

in Eqs. (62)–(65).

For $\alpha = 4$ in Figs. 8 and 9 the distribution of the normalized vacancy concentration ν and the reduced hydrostatic pressure,

$$\eta = \frac{\Omega\sigma}{kT} = \ln(\nu) \quad (67)$$

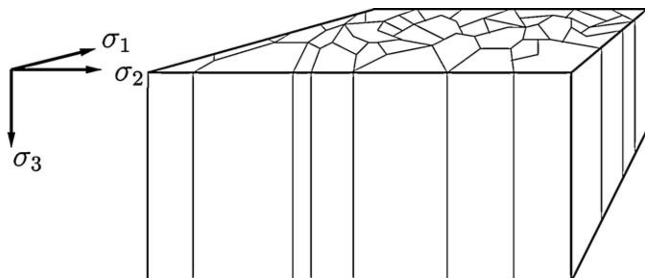

Fig. 7. Aluminum interconnect with a columnar grain structure.

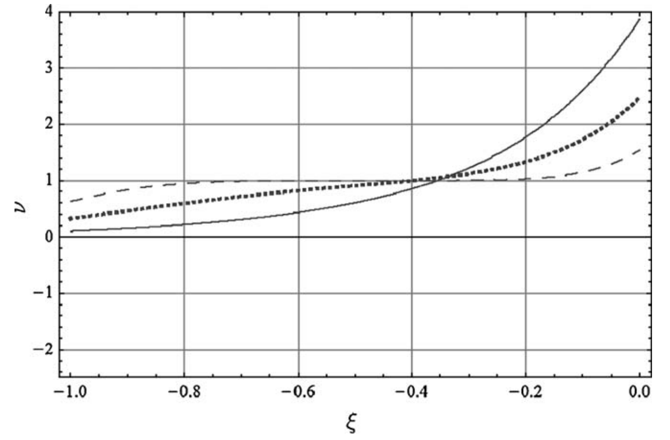

Fig. 8. Build-up of vacancies at the blocking boundaries for $\zeta = 0.01$ (dashed line), $\zeta = 0.05$ (points), $\zeta = 0.2$ (full line).

are presented for different EM stressing times. The normalized flux

$$J_v = \frac{\partial\nu}{\partial\xi} - \alpha\nu \quad (68)$$

is presented in Fig. 10. The stress build-up continues, until the EM driving force is counter-balanced by intrinsic stress in the line. That is the case in Fig. 9 for $\zeta = 0.2$, where the stress profile is a straight line. The condition for the equilibrium between stressmigration and EM is, as expected, again the Blech condition (45).

In the model of Korhonen et al. [61], the source term γ describes the vacancy recombination which takes place in dislocations, while Clement's model [65] includes also grain boundaries as possible recombination sites. This kind of models was developed for a generation of interconnects, where the dimensions substantially exceed the grain size, but for modern copper interconnects more detailed models of the grain boundary physics are necessary.

The analysis of experimental results led already in 1971 Rosenberg and Ohring [66] to the conclusion that for aluminum the grain boundary transport plays the major role for EM. The film surface and bulk diffusion effect are only of secondary importance. Consequently, the vacancy balance equation holds only for grain boundaries

$$\frac{\partial C_v(\vec{r},t)}{\partial t} = -\nabla\cdot\vec{J}_v + \frac{C_v(\vec{r},t) - C_v^{eq}}{\tau_v}, \quad (69)$$

where the *ad hoc* second term was introduced on the right side as the vacancy generation rate with C_v^{eq} as the equilibrium vacancy

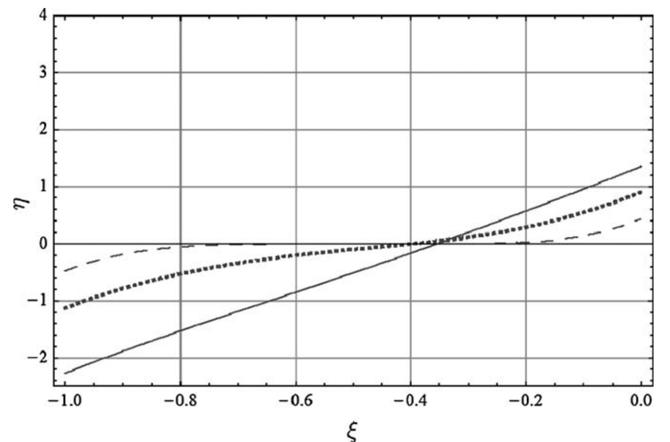

Fig. 9. Build-up of hydrostatic pressure at the blocking boundaries for $\zeta = 0.01$ (dashed line), $\zeta = 0.05$ (points), $\zeta = 0.2$ (full line).

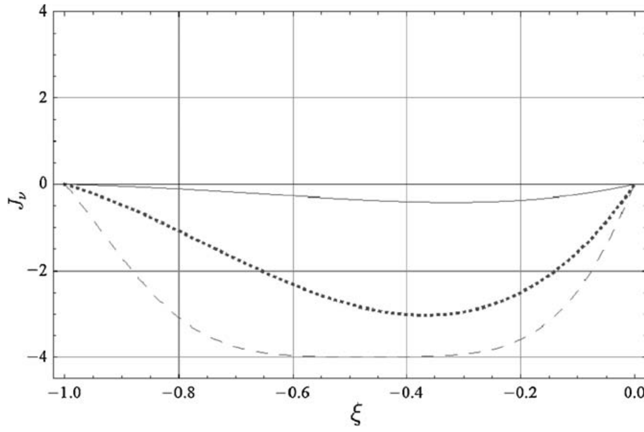

Fig. 10. Normalized flux J_v along the interconnect line for ζ = 0.01 (dashed line), ζ = 0.05 (points), ζ = 0.2 (full line).

concentration rate and τ_v as the lifetime of vacancies in the presence of sinks. The fact that grain boundaries in metals present sites of point defect generation and annihilation has been experimentally validated at the end of the 70s [67], also the role of grain boundary dislocations has been extensively investigated [68].

A similar recombination term is used by Kirchheim in 1992 [69], with an additional dependence of the equilibrium vacancy concentration on the hydrostatic stress σ.

$$C_{v0}^{eq} = C_{v0} \exp\left(\frac{(1-f)\Omega\sigma}{kT}\right) \tag{70}$$

Here, C_{v0} is the equilibrium concentration in the absence of stress and f is the atom–vacancy relaxation factor. Using a simplified aluminum microstructure with squared grains Kirchheim [69] derives the equation for the "rate of vacancy annihilation or production" τ_s.

$$\frac{1}{\tau_s} = \frac{2D_{gb}}{d\lambda} \tag{71}$$

D_{gb} is the diffusivity in grain boundaries, λ is the characteristic diffusion length, and d is the grain diameter.

In 1999 Sarychev and Zhitnikov [70] in their general, three-dimensional formulation of the EM problem give the following expression for the recombination term:

$$\gamma = L_v \mu_v \tag{72}$$

L_v is the rate parameter and μ_v is the chemical potential of vacancies, which can be written as

$$\mu_v = kT \ln\left(\frac{C_v}{C_v^{eq}}\right). \tag{73}$$

If the deviation of the vacancy concentration from its equilibrium value is small, the chemical potential μ_v can be approximated as

$$\mu_v = kT\left(\frac{C_v}{C_v^{eq}} - 1\right). \tag{74}$$

By setting $\tau_v = -C_v/kTL_v$ the original Rosenberg–Ohring term is recovered.

$$\gamma = -\frac{C_v - C_v^{eq}}{\tau_v} \tag{75}$$

The model of Sukharev et al. [71] in 2007 extends the previous models by introducing "plated atoms" to describe the atom exchange between copper bulk on the one hand side and grain boundaries and interfaces on the other hand side. It has been assumed that the vacancy-plated atom pairs are simultaneously generated/recombined. Because of the huge difference in mobility of the atoms and vacancies the plating atoms stay, where they are generated (interfaces and grain boundaries), while vacancies migrate under the influence of the present driving forces. Evolution of the plated atom concentration (M) is described by the following set of equations

$$\frac{\partial M}{\partial t} = 0 \tag{76}$$

for bulk and

$$\frac{\partial M}{\partial t} - \gamma = 0 \tag{77}$$

for interfaces and grain boundaries.

The diffusion of point defects inside the grain boundary is faster compared to grain bulk diffusion due to the fact [72] that a grain boundary generally exhibits a larger diversity of point defect migration mechanisms. Moreover, formation energies and migration barriers of point defects are in average lower than those for lattice.

In 1951 Fisher published his nowadays classic paper [73] presenting the first theoretical model of grain boundary diffusion. That pioneering paper, together with concurrent experimental measurements by Turnbull and Hoffman [74], initiated quantitative studies of grain boundary diffusion in solids. The fact that grain boundaries in metals provide high-diffusivity paths was known already in the 1930s, mostly from indirect and qualitative experiments. For example, the enhanced rates of sintering, creep, discontinuous precipitation, and other processes and reactions in polycrystalline samples were attributed to an accelerated atomic transport along grain boundaries.

The model of Fisher [73] considers diffusion in a semi-infinite sample containing a single grain boundary normal to the surface. The grain boundary is modeled by a high-diffusivity slab of width δ, embedded in a bulk with low diffusivity.

Both the grain boundary and the bulk segment are assumed to be uniform and isotropic media which follow Fick's law with the diffusion coefficients D_{gb} and D_b, respectively (Fig. 11). The diffusing atoms, initially deposited on the surface, penetrate fast along the grain boundary and are partly lost to the surrounding volume (grains). Fisher described an interesting analogy of this situation with diffusion of heat along a copper foil embedded in cork. The diffusion of vacancies into the system is described by two coupled equations.

$$\frac{\partial C_v}{\partial t} = D_b\left(\frac{\partial^2 C_v}{\partial x^2} + \frac{\partial^2 C_v}{\partial y^2}\right) \quad |x| > \frac{\delta}{2} \tag{78}$$

$$\frac{\partial C_v^{gb}}{\partial t} = D_{gb}\frac{\partial^2 C_v^{gb}}{\partial y^2} + \frac{2D_b}{\delta}\left(\frac{\partial C_v}{\partial x}\right)_{x=\delta/2} \tag{79}$$

C_v^{gb} is the vacancy concentration in the grain boundary and δ is the grain boundary thickness. The last term in Eq. (79) takes into account the leakage of the diffusing atoms from the grain boundary to the bulk. Based on this model for a single grain boundary, diffusion in polycrystalline samples has been analyzed in great detail, e.g. [75] Different kinetic regimes of experiments have been identified, depending on the grain size relative to the diffusion paths in the grains and along grain boundaries.

Grain boundaries play an important role in stress relaxation during EM. This model can therefore not be sufficient for the complete description of the grain boundary physics.

We consider the famous relationship

$$\mu_v^{gb} = \mu_0 + \Omega\sigma_{nn} \tag{80}$$

given by Herring for a chemical potential on the material surfaces and grain boundaries [76] as a basis for the extension of Fisher's grain

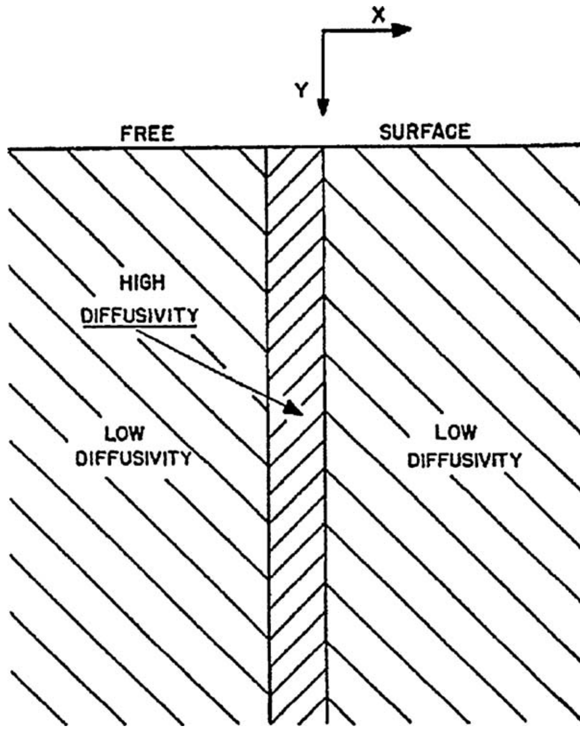

Fig. 11. Coordinate system used by Fisher [73]. A high diffusivity area (grain boundary) is embedded in the semi-infinite bulk.

boundary model. μ_0 is some chemical reference potential, $\sigma_{nn} = \vec{n} \cdot \bar{\bar{\sigma}} \cdot \vec{n}$ and $\vec{n}$ is the normal to the grain surface. This relationship is obtained by careful equilibrium analysis of the material exchange between the grain bulk and the grain boundary [76–78].

In the case that the vacancy concentration varies along the grain boundary one has to extend (80) with a concentration contribution

$$\mu_v^{gb} = \mu_0 + \Omega\sigma_{nn} + k_B T \ln\left(\frac{C_v^{gb}}{C_v^0}\right) \tag{81}$$

Assuming that in equilibrium $\mu_v^{gb} = \mu_v = \mu_0$ it follows that

$$C_v^{gb,eq} = C_v^0 \exp\left(-\frac{\sigma_{nn}\Omega}{k_B T}\right), \tag{82}$$

which is similar to the equilibrium expression (58) used by Korhonen et al. [61]. Eq. (82) is originally derived by Balluffi and Granato [62]. Both expressions (80) and (82) are infact the consequences of different kinds of equilibriums. Eq. (80) follows from equilibrium atom exchange between volume and surface (grain boundary) [76] and (82) from local equilibrium between surface stress and vacancy concentration [62]. The presence of the EM force makes the usage of any kind of equilibrium model for grain boundaries problematic.

The general expression for the vacancy flux along a grain boundary is

$$J_v^{gb} = \frac{D_v^{gb} C_v^{gb}}{k_B T} \frac{\partial \mu_{gb}}{\partial l}, \tag{83}$$

where l is the distance along the grain boundary.

Fisher's expression for vacancy diffusion inside a grain boundary is

$$\frac{\partial C_v^{gb}}{\partial t} = -\frac{\partial J_v^{gb}}{\partial l} - \frac{1}{\delta}(J_{v,2} - J_{v,1}). \tag{84}$$

By taking $J_{v,2}$ and $J_{v,1}$ to be the normal components of the flux from both sides of the grain boundary, the extension of the originally two-dimensional model to a three-dimensional situation is straightforward. The emission and absorption of the vacancies is determined by the fluxes $J_{v,2}$ and $J_{v,1}$ and both of these fluxes depend on the stress σ_{nn}.

For the expressing chemical potential of the vacancies in the bulk we use the expression based on the work of Larché and Cahn [79–81].

$$\mu_v = \mu_0 + k_B T \ln\left(\frac{C_v}{C_v^0}\right) + \frac{1}{3} f\Omega \mathrm{tr}(\bar{\bar{\sigma}}). \tag{85}$$

Larché and Cahn make also equilibrium assumptions, but their work is more general and rigorous than the work of Herring and thus opens a way for studying systems out of equilibrium. The grain boundary as a vacancy transport medium is defined by the chemical potential (81) in the continuum modeling approach. This chemical potential is constant through the grain boundary thickness and equal to the bulk chemical potential on the interfaces to the bulk regions, e.g. $\mu_v^1(-\delta/2) = \mu_v^2(+\delta/2) = \mu_{gb}$, Fig. 12.

The vacancy fluxes on both sides of the grain boundary are given by

$$J_{v,1} = \frac{D_v C_v}{k_B T} \nabla \mu_v^1, \tag{86}$$

$$J_{v,2} = \frac{D_v C_v}{k_B T} \nabla \mu_v^2. \tag{87}$$

The difference $J_{v,2} - J_{v,1}$ is an actual loss (gain) of vacancies, which is localized at the thin slice representing the grain boundary. The recombination rate can now be approximated as

$$\frac{\partial C_v}{\partial t} = -\mathrm{div} J_v \approx -\frac{J_{v,2} - J_{v,1}}{\delta}. \tag{88}$$

The combination of Larché and Cahn's and Fisher's modeling approaches enables a certain insight in the vacancy dynamics in the presence of grain boundaries, however, for numerical implementation such a method is rather inconvenient. In [82] a new model is introduced where a grain boundary is treated as a separate medium with the capability of absorbing and releasing vacancies. We denote the vacancy concentration from both sides of the grain boundary as $C_{v,1}$ and $C_{v,2}$, respectively, and the concentration of immobile vacancies which are trapped inside the grain boundary as C_v^{im} (Fig. 13). We assume that vacancies are trapped from both neighboring grains with the trapping rate ω_T and released to these grains with a release rate ω_R.

With a careful analysis of the exchange of vacancies between the grain boundary and the grains and taking into account the

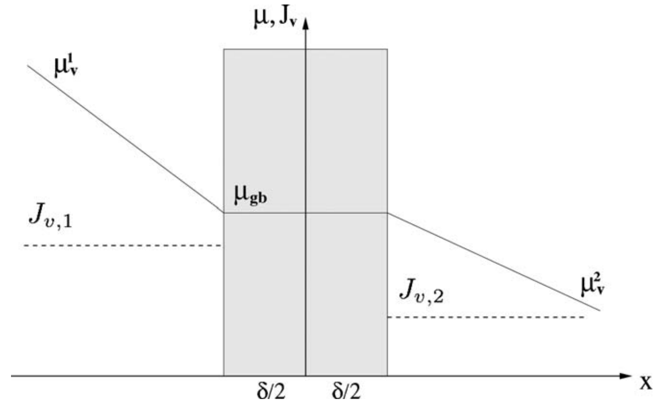

Fig. 12. The grain boundary according to Fisher's model and Herring's relationship.

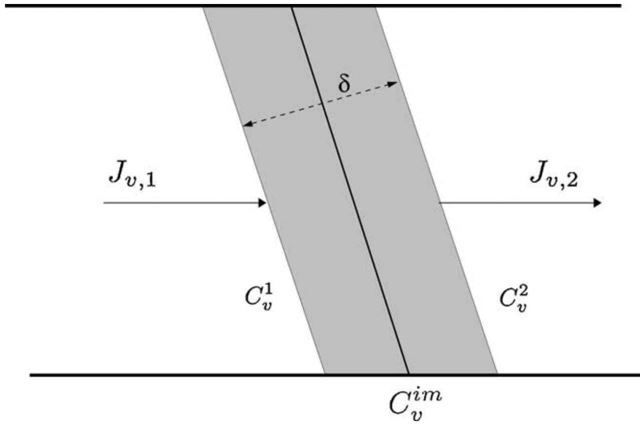

Fig. 13. The fluxes $J_{v,1}$ and $J_{v,2}$ change the concentration of mobile vacancies ($C_{v,1}$,$C_{v,2}$) and immobile vacancies (C_v^{im}).

process of vacancy trapping the following expression for the source term γ is obtained [82]

$$-\gamma = \frac{\partial C_v^{im}}{\partial t} = \frac{1}{\tau_v}\left(C_v^{eq} - C_v^{im}\left(1 + \frac{2\,\omega_R}{\omega_T(C_{v,1} + C_{v,2})}\right)\right), \tag{89}$$

$$\frac{1}{\tau_v} = \frac{\omega_T(C_{v,1} + C_{v,2})}{\delta}. \tag{90}$$

For

$$\frac{2\,\omega_R}{\omega_T(C_{v,1} + C_{v,2})} \ll 1 \tag{91}$$

the expression (89) reduces to the Rosenberg–Ohring term (75).

A general, three-dimensional expression for the vacancy flux $\vec{J}_v$ driven by gradients of the chemical potential and EM is given by

$$\vec{J}_v = -\frac{C_v}{k_B T}\mathbf{D}_v(\nabla\mu_v + |Z^*|e\nabla\varphi). \tag{92}$$

φ is the electric potential which obeys Laplace's equation ($\Delta\varphi = 0$). Here we also introduce a tensorial diffusivity $\mathbf{D}_v$ which describes an anisotropy of vacancy transport caused by the crystal deformation. The bulk chemical potential μ_v of vacancies is defined by (85).

Instead of using the immediate relationship between lattice density and hydrostatic stress (54) as Korhonen et al. [61] and Clement [63] do, other researchers, such as Povirk [83] and Rzepka et al. [84] employed the idea that diffusion fluxes give rise to volumetric strain, which establishes stress fields, thus driving stress-migration fluxes. Using a similar concept, Sarychev and Zhitnikov [70] proposed a three-dimensional self-consistent model of stress evolution during EM. In this model local volume change is assumed to be generated by vacancy migration and by EM. The local volume change is then treated like thermal strain. The stress fields are calculated as a result of volumetric strain induced by EM. In this approach the assumption of elastic material property is not longer necessary, and all the components of the stress tensor, instead of just hydrostatic stress, are available.

We obtain a kinetic relation for the evolution of the strain tensor $\bar{\bar{\varepsilon}}^v$ caused by vacancy migration and recombination [70,85]

$$\frac{\partial\varepsilon_{ij}^v}{\partial t} = \frac{\Omega}{3}\left[(1 - f)\nabla\cdot\vec{J}_v + f\,\gamma\right]\delta_{ij}. \tag{93}$$

According to [81] the general form of the mechanical equilibrium equation is

$$\sum_{j=1}^{3}\frac{\partial\sigma_{ij}}{\partial x_j} = 0, \quad \text{for } i = 1,2,3. \tag{94}$$

Taking into account the strain induced by vacancy migration and recombination we obtain [70]

$$\sigma_{ij} = (\lambda\,\mathrm{tr}(\varepsilon) - B\,\mathrm{tr}(\varepsilon^v))\delta_{ij} + 2G\varepsilon_{ij}, \tag{95}$$

where λ and G are Lame's constants and $B = (3\lambda + 2G)/3$ is the bulk modulus. The strain tensor ε^v is defined by relation (93). In [70,85,86] a similar expression for the strain rate is used, however, instead of immobile vacancies related to the source term γ a Rosenberg–Ohring term is used.

Sukharev et al. [71] use an expression for the strain, which also includes variation of the plated atom concentration.

$$\varepsilon_{ij}^v = [(1 - f)(C_v - C_v^{eq}) - (M - M^{eq})]\delta_{ij} \tag{96}$$

According to this approach, EM induced strain and the vacancy and the plated atom concentration are closely coupled with similar time and spatial behavior.

The continuum and phenomenological modeling of EM was initially motivated by the necessity to interpret and explain the experimentally observed degradation of metal films. Two main development paths can be recognized. The work of Wever [59] marks an important milestone of the first direction. It was rigorosly founded on non-equilibrium thermodynamics and has set a framework for modeling of EM in connection to other driving forces such as gradients of temperature and atom concentration. This work has been continued in the publications of Kirchheim and Kaeber [87] who also introduced a thermodynamical expression for the atomic flux driven by the gradient of the hydrostatic stress. The study of realistic three-dimensional structures was enabled by a numerical implementation of the model which was performed by Weide-Zaage et al. [88].

The crucial relationship between EM and mechanical stress has begun to reveal in the work of Blech [29,30], which together with Black [27] designates a second development line of EM models. The main characteristic of this work is the semi-empirical approach in modeling and considering mechanical stress. Schatzkes and Lloyd [60] have provided a rigorous derivation of Black's Eq. (45) and their work was continued by Korhonen et al. [61] and Clement [63]. However, all of these models are basically one-dimensional.

Both lines of EM models finally led to the model of Sarychev and Zhitnikov [70], which is set for general three-dimensional interconnect structures, where the vacancy flux is driven by EM and the gradients of vacancy concentration, stress, and temperature. It contains the linear elastic mechanics model with a strain build-up rate related to recombination and migration of vacancies (93). Including of the grain boundaries and interfaces in EM modeling was performed by Sukharev et al. [71].

3.2. The anisotropy of elastic properties

It has been observed that in dual-damascene copper lines mainly four texture components occur [89]. {1 1 1} orientations are the main component but in addition, also orientations due to sidewall nucleation and due to twinning, as well as a random component exist. The volume fractions for the {1 1 1} orientations depend strongly on the processing conditions.

Copper exhibits a pronounced elastic anisotropy. For example, the shear modulus for {1 0 0} shear is three times larger than the shear modulus for {1 1 0} shear.

The elastic problem accompanying the material transport problem for vacancies, which relates strain ε_{kl} to stress σ_{ij}, is defined by Hook's law

$$\sigma_{ij} = \sum_{i,j} C_{ijkl}\varepsilon_{kl} \tag{97}$$

and the equilibrium condition (94), where C_{ijkl} are the components of the stiffness tensor. For a cubic crystal the stiffness tensor is

defined by only three elastic stiffness constants: C_{11}, C_{12}, and C_{44}. If we prescribe these constants to a grain with crystallographic planes parallel to the interconnect line facets, the transformation of the stiffness tensor due to the rotation of the grain is given by [90]

$$C'_{ijkl} = \sum_{g,h,m,n} T_{ig} T_{jh} C_{ghmn} T_{km} T_{nl}. \tag{98}$$

If the disorientations of the grains relative to the line are described using Euler's angles (ϕ, θ, κ) in Bunge's form, the rotation is described by the product of three matrices: $T = A_z(\phi)A_x(\theta)A_z(\kappa)$, where

$$A_z(\phi) = \begin{bmatrix} \cos\phi & \sin\phi & 0 \\ -\sin\phi & \cos\phi & 0 \\ 0 & 0 & 1 \end{bmatrix}, \tag{99}$$

$$A_x(\theta) = \begin{bmatrix} 1 & 0 & 1 \\ 0 & \cos\theta & -\sin\theta \\ 0 & \sin\theta & \cos\theta \end{bmatrix}, \tag{100}$$

$$A_z(\kappa) = \begin{bmatrix} \cos\kappa & \sin\kappa & 0 \\ -\sin\kappa & \cos\kappa & 0 \\ 0 & 0 & 1 \end{bmatrix}. \tag{101}$$

The relationship (98) is used by Sukharev et al. [71,91] and Kteyan et al. [92], where the crystal orientation inside the grains is experimentally determined by EBSD analysis. Compared with the impact of other microstructural features, the variation of the elastic properties is found to cause only small stress variations [71].

The copper interconnect is a complex mechanical system consisting of grain regions with distinctive mechanical properties. The studied cases did not show a significant impact of elastic properties variation due to different grain boundary regions on the overall stress distribution but these application considered bulk properties only. The situation may change when we consider crystal orientation related variation of mechanical in combination with more detailed models for fast diffusivity paths.

3.3. Stress induced anisotropy of electromigration

Electromigration is influenced by stress through a stress-dependent diffusion coefficient of vacancies. The choice of passivating film material and the corresponding process technology cause tensile or compressive stress in the interface between the passivating film and the interconnect metal. Interfacial compressive stress diminishes EM along interfaces by reducing diffusivity [26]. The stress in a dual-damascene interconnect is anisotropic and, moreover, different components relax with different rates [93]. The unpassivated interconnect relaxes fastest, while those passivated with carbide relax at an intermediate rate compared to the slow relaxation rate in the case of the SiN passivation (Fig. 15). The relative rates of stress relaxation correlate with the EM lifetimes. The transverse stress component σ_{yy} relaxes faster than the longitudinal one σ_{yy}, cf. Fig. 14.

A careful analysis of the vacancy diffusion [94] based on classical thermodynamics provides the following expression

$$D_v = \gamma a^2 \nu \exp\left(-\frac{\Delta G}{kT}\right) \tag{102}$$

where γ is a geometrical constant of order unity, a is the lattice parameter, and ν is the vibrational frequency. $\Delta G = \Delta G_f + \Delta G_m$, where ΔG_f and ΔG_m are increments of Gibbs free energy of vacancy formation and vacancy migration. The diffusion of vacancies is studied as an isobaric and isothermal process [95]. Therefore, the starting point of the analysis is the Gibbs free energy

$$G = F + pV, \tag{103}$$

which is determined by the free energy F, the pressure p, and the volume V. The vacancy formation causes a volume change V_f, and vacancy migration a volume change V_m. For the vacancy diffusivity under the influence of an external pressure p we obtain from (102) and (103)

$$D_v = \gamma a^2 \nu \exp\left(-\frac{\Delta F + p(V_f + V_m)}{kT}\right), \tag{104}$$

with $\Delta F = \Delta F_f + \Delta F_m$, where ΔF_f and ΔF_m are changes of the free energy upon vacancy formation and vacancy migration, respectively.

Instead of a scalar point defect (vacancy) formation volume, Aziz [96,97] introduces a formation strain tensor $\bar{\bar{V}}_f$.

$$\bar{\bar{V}}_f = \pm\Omega \begin{bmatrix} 0 & & \\ & 0 & \\ & & 1 \end{bmatrix} + \frac{V^r}{3} \begin{bmatrix} 1 & & \\ & 1 & \\ & & 1 \end{bmatrix} \tag{105}$$

The sign + is for vacancy formation and the sign − is for interstitial formation. V^r is the relaxation volume which propagates elastically to all surfaces and provides equal contributions along all axes, on average, after point defect equilibration(Fig. 16). Similarly to the formation strain tensor, Aziz [96,97] also introduces the migration strain tensor $\bar{\bar{V}}_m$.

$$\bar{\bar{V}}_m = \begin{bmatrix} V_\perp^m & & \\ & V_\perp^m & \\ & & V_\parallel^m \end{bmatrix} \tag{106}$$

where $V_\perp^m$ and $V_\parallel^m$ are the volume changes perpendicular and parallel to the diffusion direction, respectively. The dependence of

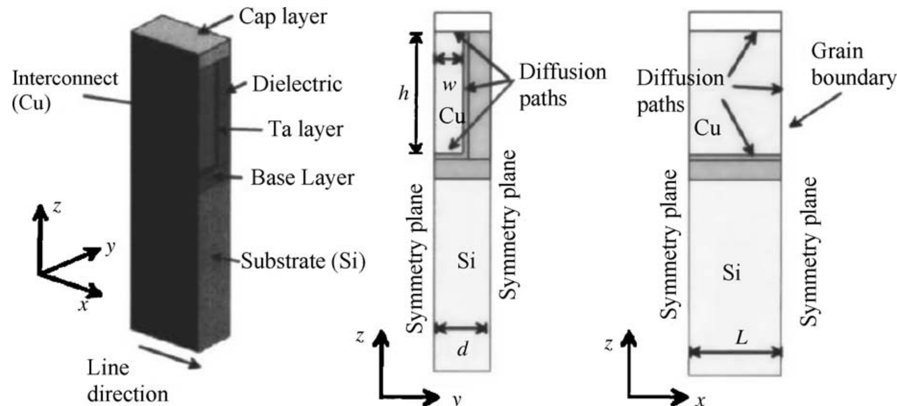

Fig. 14. Idealized model of the three-dimensional interconnect model used for relaxation studies (courtesy of Dr. N. Singh) [93].

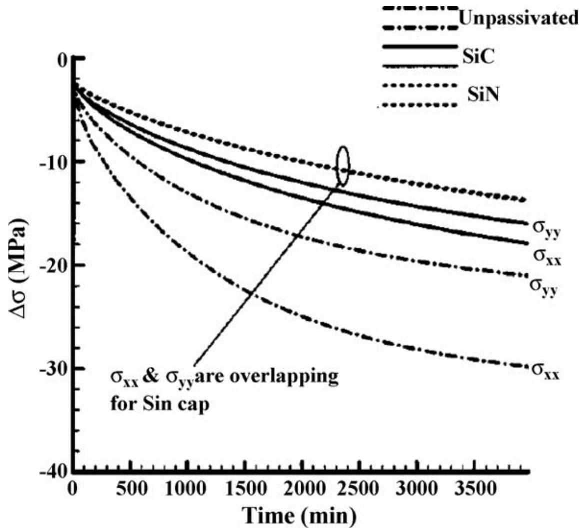

Fig. 15. Stress relaxation in the idealized interconnect structure (courtesy of Dr. N. Singh) [93].

the vacancy diffusivity D_v on hydrostatic pressure (104) can also be extended for a general stress field $\bar{\bar{\sigma}}$ we have

$$D_{\nu} = \gamma a^2 \nu \exp\left(-\frac{\Delta F + \bar{\bar{\sigma}} : \bar{\bar{V}}}{kT}\right) \tag{107}$$

The relationship (104) is used in numerous EM models [92,98–100], however it only describes the influence of a scalar hydrostatic pressure on the scalar diffusivity.

In order to fully understand the interplay between EM and the stress field one has to consider an atomic theory of diffusion and EM. Generally, linear elasticity is used, which ensures that the problem can be equally well defined in the terms of stress as well in the terms of strain.

The simplest case of diffusion of a homogeneously deformed cubic crystal with a strain field ε_{kl} was studied by Flynn [94]. In this case the isotropic diffusion coefficient D_0 contains a contribution proportional to ε_{kl},

$$D_{ij} = D_0\,\delta_{ij} + \sum_{k,l=1}^{3} d_{ijlk}\,\varepsilon_{kl}, \tag{108}$$

where d_{ijlk} is the elastodiffusion tensor [94], which is experimentally determined.

A comprehensive and rigorous theory of anisotropic diffusion in strain field was given in 1978 by Dederich and Schroeder [101].

We denote with $c_\nu(\vec{r}_m, t)$ the probability that a vacancy occupies a site m at time t. The change of the occupation probability c_ν at this site is defined by the master equation.

$$\frac{\partial c_\nu(\vec{r}_m, t)}{\partial t} = \sum_n (\Gamma_{mn} c_\nu(\vec{r}_n, t)) - (\Gamma_{nm} c_\nu(\vec{r}_m, t)) + p(\vec{r}_m) \tag{109}$$

$p(\vec{r}_m)$ is the particle production rate at the site m. The vacancy concentration C per unit volume is given as $C = Nc_\nu$, where N is the number of possible vacancy sites per unit volume.

The transition probabilities Γ_{mn} are given with the Vineyard formula [102].

$$\Gamma_{mn} = \frac{\prod_{i=1}^{3N} \nu_i^{(n)}}{\prod_{j=1}^{3N-1} \nu_j^{(m,n)}} \exp\left(-\frac{E_0}{kT}\right) \exp\left(-\frac{E_s^{(m,n)} - E_e^{(n)}}{kT}\right) \tag{110}$$

$\nu_i^{(n)}$, $i = 1 \ldots 3N$ are the eigenfrequencies of the whole crystal, if the vacancy is localized at the position $\vec{r}_n$, whereas $\nu_j^{(m,n)}$, $j = 1 \ldots 3N - 1$ are the eigenfrequencies of the crystal, if the vacancy is at the saddle point between the sites $\vec{r}_n$ and $\vec{r}_m$. E_0 is the saddle-point energy in the ideal lattice. The potential energy in the saddle-point (m, n), which connects equlibrium positions n and m, differs from E_0 by $E_s^{(m,n)}$, and the energy in the equilibrium position n is $E_e^{(n)}$ (Fig. 17).

In thermal equilibrium we have

$$p(\vec{r}_m) = 0, \quad \text{and} \quad \frac{\partial c_\nu(\vec{r}_m, t)}{\partial t} = 0. \tag{111}$$

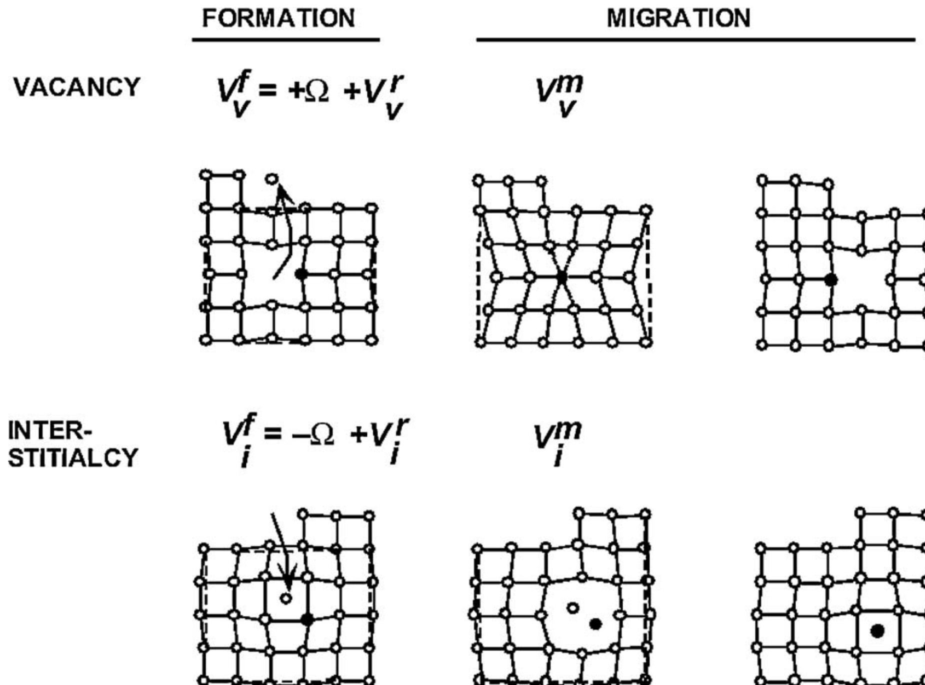

Fig. 16. Formation and migration volumes for vacancy (top) and interstitial (bottom) diffusion mechanisms [97].

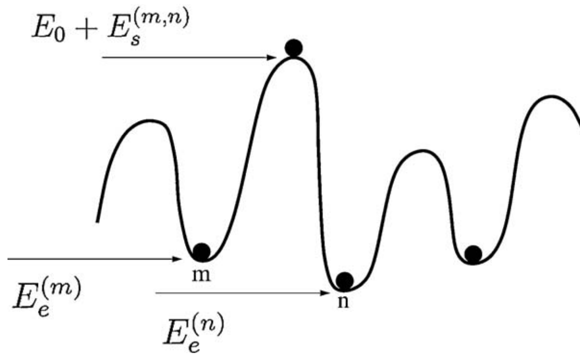

Fig. 17. The energy profile of the vacancy in a distorted crystal.

Together with the normalization condition

$$\sum_n c_v(\vec{r}_n, t) = 1 \tag{112}$$

the equlibrium vacancy probability of finding a vacancy at site n is

$$c_v^e(\vec{r}_n) = \frac{\exp(-(E_e^n/kT))}{\sum_m \exp(-(E_e^m/kT))}. \tag{113}$$

The last equation can be also derived from variational principles. For this purpose Dederich and Schroeder introduce the "lattice equivalent of Lagrangian" [101]

$$L(W_m) = \frac{1}{4}\sum_{(m,n)} \Gamma_{mn}(W_n - W_m)^2 - \sum_m p_m W_m \tag{114}$$

by introducing a renormalized density

$$W_n = c_v(\vec{r}_n) \exp\left(\frac{E_e^n}{kT}\right). \tag{115}$$

The extremal condition $\delta L = 0$ yields the stationary distribution at the thermal equilibrium (113).

(114) can be used for the description of the transition to continuum diffusion. For this purpose one expands $W_n = W(\vec{r}_n)$ in a Taylor series at point $\vec{r}_m = (x_1^m, x_2^m, x_3^m)$.

$$W(\vec{r}_n) = W(\vec{r}_m) + \sum_i (x_i^n - x_i^m) \frac{\partial W(\vec{r})}{\partial x_i}\bigg|_{\vec{r}=\vec{r}_m} + \ldots \tag{116}$$

This is possible only, if we assume that $W(\vec{r}_n)$ is slowly varying [101]. By inserting (116) into (114) and transforming the sum in an integral over $\vec{r}_n = \vec{r}$ we obtain

$$L(W) = \int \frac{d^3 r}{V}\left(\frac{1}{2}\sum_{ij} D'_{ij}(\vec{r}) \frac{\partial W(\vec{r})}{\partial x_i}\frac{\partial W(\vec{r})}{\partial x_j} - p(\vec{r})W(\vec{r})\right), \tag{117}$$

where D'_{ij} is the diffusivity tensor for the renormalized probability W.

$$D'_{ij}(\vec{r}) = \frac{1}{2}\sum_k \Gamma_0^k x_i^k x_j^k \exp\left(-\frac{E_s^k}{kT}\right) \tag{118}$$

The summation in (118) is performed over all available jump vectors ($\vec{r}_k = \vec{r}_m - \vec{r}_n$) in the crystal lattice. Γ_0^k is the jump rate for the ideal crystal for the jump direction $\vec{r}_k$ defined with the Vineyard formula (110), which gives

$$\Gamma^k = \Gamma_{mn} = \Gamma_0^k \exp\left(-\frac{E_s^{(m,n)} - E_e^{(n)}}{kT}\right). \tag{119}$$

We confine the jump vectors only to Z neighboring sites and assume the same length λ of all jump vectors, which is the case for vacancy assisted diffusion in fcc crystals, cf. Fig. 18,

$$|\vec{r}_1| = |\vec{r}_2| = \ldots = |\vec{r}_Z| = \lambda. \tag{120}$$

Furthermore, we assume the isotropy of jumping frequencies for an ideal unstressed crystal lattice (e.g. $\Gamma_0^k = \Gamma_0$). Now, with normalized coordinates for jump sites

$$a_i^k = \frac{x_i^k}{\lambda}, \tag{121}$$

from (118) follows

$$D'_{ij}(\vec{r}) = \frac{6D_0}{Z}\sum_{k=1}^{Z} a_i^k a_j^k \exp\left(-\frac{E_s^k}{kT}\right). \tag{122}$$

Here D_0 is the vacancy diffusivity in the ideal crystal lattice [95].

$$D_0 = \frac{1}{12} Z \Gamma_0 \lambda^2 \tag{123}$$

Following the procedure originally described by Schroeder and Dettmann [103] we obtain the differential equation for the renormalized probability W.

$$\sum_{ij} \frac{\partial}{\partial x_i}\left(D'_{ij}\frac{\partial W}{\partial x_j}\right) + p = 0 \tag{124}$$

Together with appropriate boundary conditions this equation determines W uniquely. The vacancy flux is given by

$$J_{v,i} = \sum_j D'_{ij}\frac{\partial W}{\partial x_j}. \tag{125}$$

By reintroducing the probability $c_v(\vec{r}) = W(\vec{r}) \exp(-E_e(\vec{r})/kT)$ in (125) one obtains the vacancy flux J_v separated in a diffusive part and a drift part.

$$J_{v,i} = J_{v,i}^{\text{diff}} + J_{v,i}^{\text{drift}} = \sum_j D_{ij}\frac{\partial c_v}{\partial x_j} - \frac{c_v}{kT}\sum_j D_{ij}\frac{\partial E_e}{\partial x_j} \tag{126}$$

$$D_{ij} = \frac{6D_0}{Z}\sum_{k=1}^{Z} a_i^k a_j^k \exp\left(-\frac{E_s^k - E_e}{kT}\right) \tag{127}$$

The application of a stress field $\bar{\bar{\sigma}}$ generally causes a distorsion of the saddle point energy E_s^k and the valley point energy E_e [103]. When a defect is created, the solid changes shape from its original condition (Fig. 19). With linear elasticity theory the change in the shape of a volume can be expressed with a real, symmetric tensor. For example, the distorsion of a sphere into an ellipsoid produces a new volume $\bar{\bar{\Omega}}$ [104].

$$\bar{\bar{\Omega}} = \begin{bmatrix} \Omega_1 & & \\ & \Omega_2 & \\ & & \Omega_3 \end{bmatrix} \tag{128}$$

Generally the symmetry of the shape change due to defect production depends on the symmetry of the defect.

The change of energy at the saddle and the valley points is determined as an additional energy needed to create the defect in

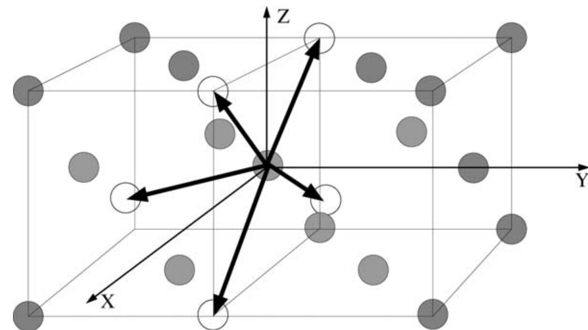

Fig. 18. Jump vectors in face-centered cubic (fcc) crystals.

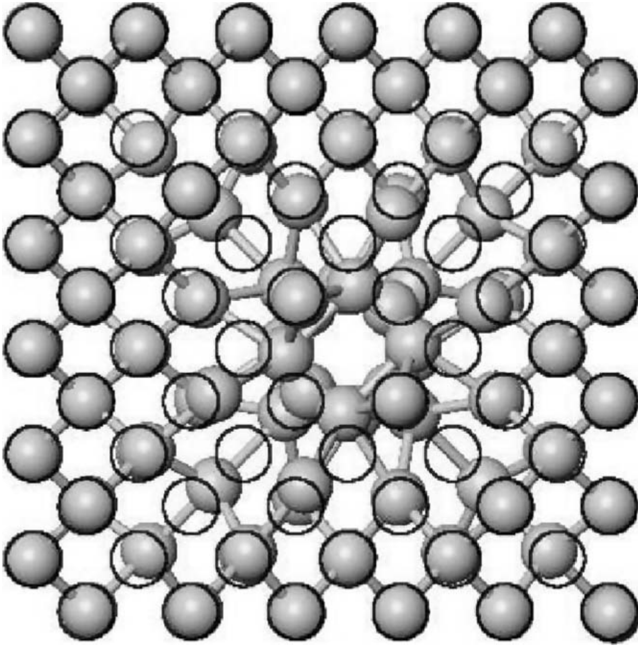

Fig. 19. A vacancy in a fcc crystal viewed along {1 0 0} direction. The open circles mark positions of atoms of the undistorted crystal before vacancy formation.

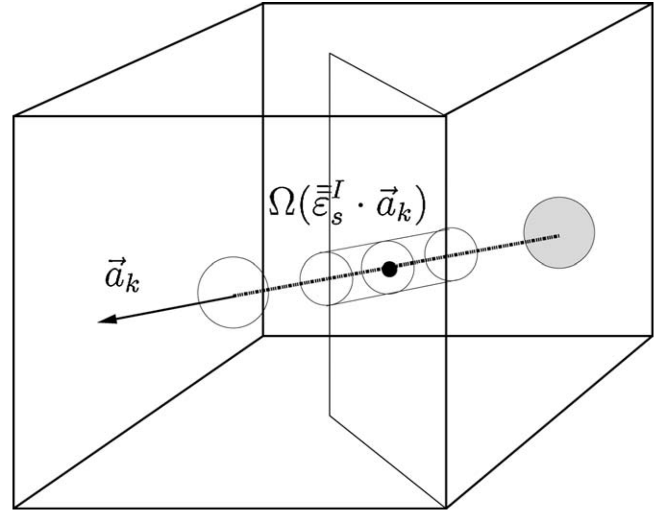

Fig. 20. Volume change caused by placing a vacancy at the saddle point in a stressed fcc crystal.

the presence of an external stress $\bar{\bar{\sigma}}$, where the stress is evaluated locally.

$$E_e(\bar{\bar{\sigma}}) = E_e(0) + \bar{\bar{\Omega}}_e : \bar{\bar{\sigma}} \tag{129}$$

$$E_s^k(\bar{\bar{\sigma}}) = E_s(0) + \bar{\bar{\Omega}}_s^k : \bar{\bar{\sigma}} \tag{130}$$

$E_e(0)$ and $E_s^k(0)$ are the creation energies in the absence of the external stresses. $\bar{\bar{\Omega}}_e$ and $\bar{\bar{\Omega}}_s^k$ are the changes in volume/shape imposed on the perfect, stressed crystal by placing the defect at the valley and the saddle point, respectively. They are not equal to the creation and migration volumes [104]. The applied stress changes the energies at the valley and the saddle site. The volume change caused by placing a vacancy at a valley site can be expressed as $\bar{\bar{\Omega}}_e = \Omega\,\bar{\bar{\varepsilon}}_e^I$, where $\bar{\bar{\varepsilon}}_e^I$ is the induced strain. In order to fully consider the influence of anisotropic stress on the saddle site energies the dependence of the strain, which is induced by a defect placed at the saddle site, on the jumping direction must be taken into account, e.g. $\Omega\,\bar{\bar{\varepsilon}}_s^I \cdot \vec{a}_k$, (Fig. 20). $\bar{\bar{\varepsilon}}_e^I$ and $\bar{\bar{\varepsilon}}_s^I$ are determined as

$$\bar{\bar{\varepsilon}}_e^I = \begin{bmatrix} \epsilon_e & & \\ & \epsilon_e & \\ & & \epsilon_e \end{bmatrix}, \quad \bar{\bar{\varepsilon}}_s^I = \begin{bmatrix} \epsilon_s & & \\ & \epsilon_s & \\ & & \epsilon_s \end{bmatrix}, \tag{131}$$

since the vacancy exhibits at the valley as well as at the saddle site a cubic symmetry. Now (129) and (130) can be rewritten as

$$E_e(\bar{\bar{\sigma}}) = E_e(0) - 3\,p\epsilon_e, \tag{132}$$

$$E_s^k(\bar{\bar{\sigma}}) = E_s(0) + \Omega(\bar{\bar{\varepsilon}}_s^I \cdot \vec{a}_k) \cdot (\bar{\bar{\sigma}} \cdot \vec{a}_k). \tag{133}$$

By inserting these expressions into (127) one obtains

$$D_{ij} = D_v \sum_{k=1}^{Z} a_i^k a_j^k \exp\left(-\frac{\Omega(\bar{\bar{\varepsilon}}_s^I \cdot \vec{a}_k) \cdot (\bar{\bar{\sigma}} \cdot \vec{a}_k)}{kT}\right) \tag{134}$$

with

$$D_v = \frac{6D_0}{Z} \exp\left(-\frac{E_s(0) - E_e(0)}{kT}\right) \exp\left(-\frac{3\,p\Omega}{kT}\right). \tag{135}$$

The effects of hydrostatic stress (pressure) can be separated from those due to devatoric stress. The devatoric stress is defined as the traceless part of the stress.

$$\bar{\bar{\sigma}} = p\bar{\bar{I}} + \bar{\bar{\sigma}}_{dev} \tag{136}$$

Similarly, for the volume tensor holds

$$\bar{\bar{\Omega}} = \frac{1}{3}\bar{\bar{\Omega}}_h + \bar{\bar{\Omega}}_a, \tag{137}$$

$$\Omega_h = \mathrm{tr}(\bar{\bar{\Omega}}), \tag{138}$$

where $\bar{\bar{\Omega}}_h$ is the total scalar volume change and $\bar{\bar{\Omega}}_a$ is the traceless part of $\bar{\bar{\Omega}}$.

The work against the external stress has two terms: one couples the pressure to the total volume change, and the other couples the devatoric stress to the anisotropic part of the saddle-point volume.

$$\bar{\bar{\Omega}} : \bar{\bar{\sigma}} = p\Omega_h + \bar{\bar{\sigma}}_{dev} : \bar{\bar{\Omega}}_a \tag{139}$$

The stress induced anisotropy of EM can be described by two modeling approaches. The first approach uses methods and concepts of classical equilibrium thermodynamics and is applicable for copper geometries of dimensions larger than about 1 μm, where microstructural and atomic properties are sufficiently good approximated by the bulk material properties. However, modern dual-damascene copper interconnects have dimensions well below 1 μm and here grain boundaries, texture, and crystal imperfections have a more subtle influence on material transport. To capture the detailed influence of material properties and stress on EM an atomic level modeling approach is necessary.

3.4. Grain boundary movement

There are experimental results [105], which show that EM in combination with mechanical stress also causes an observable grain boundary movement. This grain boundary drifting can be important in some void nucleation scenarios and also causes pre-nucleation fluctuation of interconnect resistance [105]. Wilkening et al. [106,107] have analyzed an influence of EM and mechanical stress on grain boundaries. The work itself does not include a new model of EM, it relays on the well known continuum description of the phenomena and, regarding mechanics, remains in the linear elastic regime, but its significance lies in the mathematical rigor

regarding the analysis of the governing equations and the development of numerical algorithms.

3.5. Void nucleation

From the early days of EM modeling for void nucleation, i.e., the transition from the first to the second phase of failure evolution, the following two conditions are used:

- void nucleation after reaching a vacancy (atom) concentration threshold [45,100]
- void nucleation after reaching a tensile stress threshold [108,109]

However, a careful investigation based on classical nucleation theory has shown that these nucleation conditions cannot be justified from a thermodynamic point of view.

A detailed theory of stress-driven void nucleation by vacancy condensation is given by Raj and Ashby [110] and Hirth and Nix [111]. Gleixner et al. [112] apply this theory to stress-driven void nucleation in aluminum interconnects embedded in a SiN_x passivation. For the case of a passivated aluminum interconnect, the free energy change ΔF upon creation of an embryo of volume V_e is given by

$$\Delta F = \Delta F_v V_e + \gamma_{Al} A_{Al} + (\gamma_{Al_2O_3} - \gamma_{Al-Al_2O_3}) A_i - \gamma_{gb} A_{gb}, \tag{140}$$

where ΔF_v is the Helmholz free energy change per unit volume of the embryo. γ_{Al}, $\gamma_{Al_2O_3}$, $\gamma_{Al-Al_2O_3}$, and γ_{gb} are interfacial free energies. A_{Al}, A_i, and A_{gb} are interface areas created or destroyed upon formation of the embryo. The quantity $(\gamma_{Al_2O_3} - \gamma_{Al-Al_2O_3})A_i$ in (140) is non-zero only in the case of the nucleation at a sidewall [112].

In the case of vacancy coalescence in a stressed material, the quantity ΔF_v is given by the chemical potential per unit volume of the vacancy relative to the unstressed solid [111].

$$\Delta F_v = p \tag{141}$$

p is the hydrostatic pressure for homogenous nucleation [111]. In the case of nucleation on the aluminum interface to a surrounding layer σ_{nn} must be taken instead of p (see Section 3.1). For negative p the free energy ΔF increases with increasing embryo volume, until a maximum value is reached, after which it decreases monotonically with embryo volume. The barrier to void nucleation, ΔF^*, is the maximum value of ΔF.

An embryo with this volume is unstable with respect to growth and is termed as critical embryo. For homogenous nucleation in the absence of grain boundaries the barrier energy ΔF^* is given by [113]

$$\Delta F^* = \frac{48\pi\gamma_m^3}{(\mathrm{tr}(\bar{\bar{\sigma}}))^2} \tag{142}$$

for spherical embryos. Here γ_m is the surface free energy of the metal and $\mathrm{tr}(\bar{\bar{\sigma}}) = 3p$ is the applied stress field.

If we assume a rather high hydrostatic pressure of 1 GPa [112] and take the surface free energy of copper 1.72 J/m^2[114], we obtain an energy barrier of 133 eV. The number of critical embryos Z per unit volume is given by [113]

$$Z = \frac{1}{\Omega n_s}\left(\frac{\Delta F^*}{3\pi k T}\right)^{1/2} e^{-(\Delta F^*/kT)}, \tag{143}$$

where n_s is the critical number of vacancies.

$$n_s = 288\frac{\pi}{\Omega}\left(\frac{\gamma_m}{\mathrm{tr}(\bar{\bar{\sigma}})}\right)^3 \tag{144}$$

Critical embryos are spontaneously formed by condensation of vacancies in stressed aluminum and copper. However, the condensation process is reversible and in most cases the embryos completely dissolve in the surrounding lattice. The situation changes, when a critical embryo starts to accept additional free vacancies. In this case the irreversible transition to an initial void is imminent [113]. The nucleation rate is then calculated as

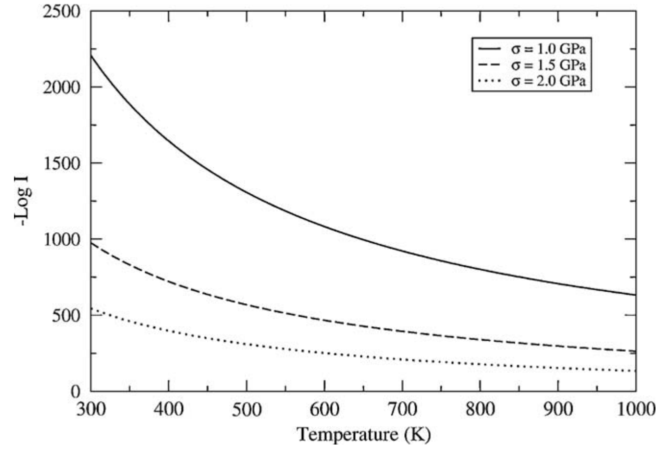

Fig. 21. Nucleation rate dependence on hydrostatic stress and temperature. Even a very high temperature cannot significantly increase the nucleation rate.

$$I = \nu\, e^{-(U_D/k_B T)} Z n_s, \tag{145}$$

where ν is the frequency of vibration of the atoms. The calculated nucleation rate in the metal bulk is $I \sim 10^{-1396}\,\mathrm{m^{-3}\,s^{-1}}$. The temperature/stress dependence of the nucleation rate is presented in Fig. 21. Similar values can be obtained for nucleation at the interconnect sidewall, grain boundaries, and sidewall/grain boundary intersection. This means that void nucleation by vacancy condensation for both, accelerated test conditions and realistic use conditions, is not possible.

An analysis carried out by Flinn [115] gave a new framework for the understanding of void nucleation. The author considers a circular patch on the interface between copper and the capping layer with virtually no adhesion. Such an entity can actually be caused by a surface defect or contamination [116]. As the stress in the line increases, the free metal surface is driven to adopt an equilibrium, half-spherical shape, and a void embryo forms. The stress threshold given by Clemens et al. [98] and Gleixner et al. [112] is

$$\sigma_{th} = \frac{2\gamma_m \sin\theta_c}{R_p}. \tag{146}$$

R_p is the radius of the adhesion-free patch and θ_c is the critical angle. For stresses $\sigma < \sigma_{th}$ an energy barrier exists between the embryo and a stable-growing void. If the stress is above the threshold value ($\sigma > \sigma_{th}$), the free energy monotonically decreases with void volume, and the energy barrier vanishes. If one assumes the adhesion free patch with a radius of 10 nm (about 20 atoms) and $\theta_c = \pi/2$, one obtains $\sigma_{th} \approx 344$ MPa. In modern interconnect structures this stress level can already be reached by thermal stress [117].

3.6. Void evolution

Experimental observations of void evolution in interconnect lines using *ex situ* and *in situ* transmission and scanning electron microscopy have significantly improved our understanding of the various failure mechanisms in interconnect structures.

The ultimate cause for the EM induced interconnect failure are voids which lead to a significant resistance increase, or even completely sever the line.

After nucleation voids grow, migrate, and change shape due to vacancy diffusion driven by a combination of EM and stressmigration. During this process, the voids can heal and disappear or collapse into fatal slits causing open circuits.

The void evolution phenomenon is complex as diffusion occurs along multiple pathways. This includes diffusion on void surfaces resulting in a shape change without growth, coupled with lattice or bulk diffusion, grain boundary diffusion, and diffusion along the line/passivation interface.

Various analytical and numerical models for the simulation of void evolution due to EM and stressmigration in interconnect structures have been developed since 1970s.

In 1970 Ho analyzed the migration of spherical and cylindrical voids under a direct current and a thermal gradient in an infinite medium and near a planar boundary [118]. Ho assumed a different effective charge for surface EM (Z_s^*) and volume EM (Z_v^*), and non-zero electrical conductivity inside the void (σ_v). Denoting the conductivity of the metal as σ_m, the migration velocity of a spherical void induced by an electric field E is

$$v_{sphere} = -\frac{2eE}{kT(2\sigma_m+\sigma_v)}\left(\frac{Z_v^* D_v(\sigma_m-\sigma_v)}{f} + \frac{3Z_s^* D_s \nu\Omega\sigma_m}{r}\right). \quad (147)$$

Here, r is the radius of the spherical void, f is the correlation factor, ν is the effective number of atoms per unit surface participating in diffusion, and D_v and D_s are the volume and the surface diffusivity, respectively. Analogously the velocity of a cylindrical void is

$$v_{cylinder} = -\frac{2eE}{kT(\sigma_m+\sigma_v)}\left(\frac{Z_v^* D_v(\sigma_m-\sigma_v)}{f} + \frac{Z_s^* D_s \nu\Omega\sigma_m}{r}\right). \quad (148)$$

In order to study the energetic and kinetic behavior of an evolving void Suo and Wang [119] introduce the thermodynamic potential Φ as the difference between the surface U_s and total elastic energy U_e.

$$\Phi = U_s - U_e \quad (149)$$

This potential is a functional of the void shape, i.e. when a surface of the void is given with a function $z = f(x, y)$, the thermodynamic potential is defined as $\Phi = \Phi[f]$. For a given void shape U_e is determined by the elasticity problem. The total elastic and surface energy are obtained by integration over the volume and the surface of the void, respectively,

$$U_s = \int_S \gamma\, dS, \quad U_e = \int_V w\, dV, \quad (150)$$

where w is the elastic energy density and γ is the surface energy density. The rates of change of the elastic and the surface energy are given with the following expressions [119,120].

$$\frac{dU_s}{dt} = -\int_S \gamma\kappa v_n\, dS, \quad \frac{dU_e}{dt} = -\int_S w v_n\, dS \quad (151)$$

Here, v_n is the normal velocity of the void surface and κ is the curvature of the surface. $v_n > 0$ means advance of the void surface, e.g. void growth. Combining (149) and (151) we obtain

$$\frac{d\Phi}{dt} = \int_S (-w+\gamma\kappa) v_n\, dS. \quad (152)$$

If $\vec{J}$ is the atomic flux along the void surface driven by a general driving force $\vec{F}$, the first law of thermodynamics requires that

$$\frac{d\Phi}{dt} + \int_S \vec{F}\cdot\vec{J}\, dS = 0, \quad (153)$$

i.e., the work done by the general dissipation driving force $\vec{F}$ equals the negative rate of change of the potential Φ. The normal velocity of the void surface v_n is simply related to the material flux divergence.

$$v_n = -\Omega\,\nabla_s\cdot\vec{J} \quad (154)$$

∇_s is the surface gradient operator. By setting (154) in (152) and integrating by parts one obtains

$$\frac{d\Phi}{dt} = -\Omega\int_S \vec{J}\cdot\nabla_s(-w+\gamma\kappa)\, dS. \quad (155)$$

The Eqs. (153) and (155) are valid for any virtual flux $\vec{J}$. By comparing these equations the expression for the driving force $\vec{F}$ is obtained

$$\vec{F} = -\Omega\nabla_s(w-\gamma\kappa). \quad (156)$$

Including the work done by EM ($\int_S \vec{F}_{wind}\cdot\vec{J}\, dS$), the balance Eq. (153) becomes [119]

$$\frac{\partial\Phi}{\partial t} + \int_S \vec{F}\cdot\vec{J}\, dS = \int_S \vec{F}_{wind}\cdot\vec{J}\, dS, \quad (157)$$

and now it follows

$$\vec{F} = \vec{F}_{wind} - \Omega\nabla_s(w-\gamma\kappa). \quad (158)$$

If one takes into account that $\vec{F}_{wind} = -|Z^*|e\vec{E}_t = |Z^*|e\nabla_s\varphi$ one obtains

$$\vec{F} = \nabla_s(|Z^*|e\varphi - \Omega(w-\gamma\kappa)). \quad (159)$$

$\vec{E}_t = -\nabla_s\varphi$ is the tangential component of the electric field. The above considerations are applicable for any kinetic relations between $\vec{J}$ and $\vec{F}$. We assume a simple linear Einstein relation

$$\vec{J} = M\vec{F}, \quad M = \frac{D_s\delta_s}{\Omega kT}. \quad (160)$$

With (159) and (160) we obtain the important relationship

$$\vec{J} = \frac{D_s\delta_s}{\Omega kT}\nabla_s(|Z^*|e\varphi - \Omega(w-\gamma\kappa)). \quad (161)$$

Eq. (161) can be generally interpreted as a flux of atoms along the surface of a void.

In 1998 Gungor and Maroudas [121] used (161) as basis for their study of the evolution of a two-dimensional void. They neglect any elastic properties of the void and introduce an anisotropy of the surface diffusivity $D_s = D_{s,min} f(\theta)$, where $D_{s,min}$ is the minimum surface diffusivity which corresponds to a specific surface orientation, and $f(\theta)$ is a function of the angle θ formed by the local tangent to the surface and the direction of the electric field far away from the void surface. In their simulations Gungor and Maroudas [121] set

$$f(\theta) = 1 + A\cos^2[m(\theta+\phi)], \quad (162)$$

where A, m, and ϕ are dimensionless parameters which determine the anisotropy. The model equations are solved using the boundary element method with linear elements. The surface of the void is explicitly tracked with the nodes of the spatial discretization. Several hundred nodes along the void surface are used. This model predicts the formation of stable faceted voids, the formation of wedge-shaped voids through a facet selection mechanism, as well as failure due to propagation of slit-like features from void surfaces. All these shapes are observed in aluminum EM tests [121].

In their publication from 1998 [122] Gungor and Maroudas improve their model by including mechanical stress. The surface elastic energy density in (161) is given by

$$w = \frac{1}{2}(\bar{\bar{\sigma}} : \bar{\bar{\varepsilon}}) \quad (163)$$

Depending on the strength of the electric field and the stress, void morphological instabilities can lead to film failure by propagation of either faceted slits or finer-scale crack-like features from the void surface.

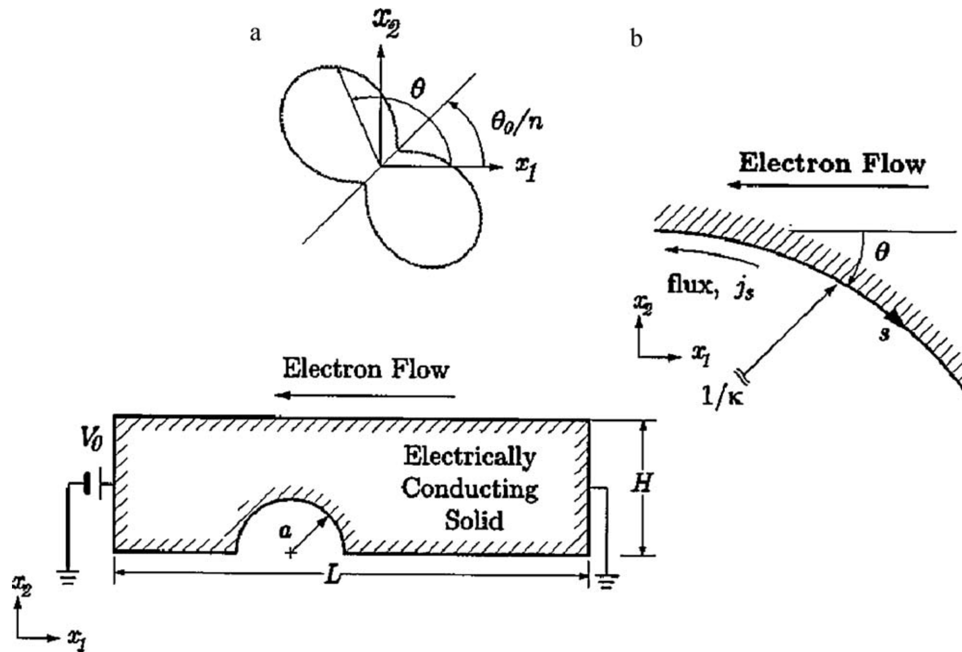

Fig. 22. (a.) Anisotropic diffusivity. (b.) Schematic representation of the model and the simulation setting (courtesy of Dr. D. Fridline) [123].

A comprehensive parametric study of void migration and evolution in an idealized interconnect was presented in 1999 by Fridline and Bower [123]. They apply anisotropic surface diffusivity and assume a completely relaxed two-dimensional interconnect structure as Gungor and Maroudas in [121]. Fridline and Bower use a finite element scheme together with local mesh adaptation. This approach enables a simulation of void movement along larger portions of a straight interconnect line (Fig. 22). Similarly to Gungor and Maroudas [121,122], Fridline and Bower introduce a dimensionless parameter χ which describes the ratio of the EM driving force to the surface energy driving force.

$$\chi = \frac{V_0 Z^* e r^2}{\Omega \gamma L} \tag{164}$$

Depending on the values of χ three void evolution regimes are recognized and discussed:

- stable void migration
- void collapse
- line severing

For low values of χ and weak anisotropy one finds that voids remain stable and develope towards an equilibrium shape as they migrate. For higher values of χ and a moderate degree of anisotropy, voids become unstable and can break up into smaller voids. For large values of χ and strong anisotropy, one finds that the void shape change may lead to the formation of transverse slit-like voids which are responsible for line failures due to severing. In Fig. 23 the case of a severing void for $\chi = 4.12$ is presented.

The models for void evolution presented are based on sharp interface theories, requiring an explicit tracking of the void surface during the course of evolution. As voids typically undergo substantial motion, growth and shape change, this surface tracking can be numerically very demanding. The numerical schemes used by Fridline and Bower [123], Gungor and Maroudas [121,122], and also for the models used by Arzt et al. [124] have performed well, when applied to an idealized two-dimensional straight interconnect line, but the complexity of surface tracking makes any extensions almost impossible.

In order to overcome the difficulties associated with the sharp interface model, Mahadevan and Bradley [125–127] proposed an alternative diffuse interface model for simulating void growth and migration. Such diffuse interface models have successfully predicted the motion and evolution of voids in interconnects by EM and stress induced surface diffusion, as well as EM induced surface instabilities. The model of Mahadevan and Bradley circumvents surface tracking by the introduction of a smooth order parameter field to describe the void structure. The order parameter takes on constant values in the material and the void,

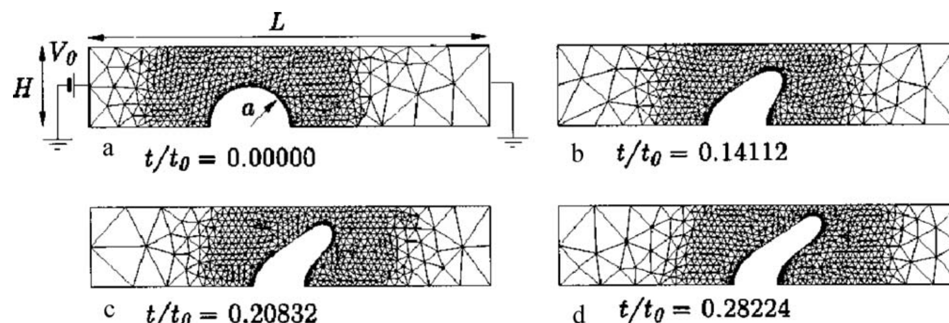

Fig. 23. An initially semi-circular void migrates and collapses into a slit-like void for $\chi = 4.12$ (courtesy of Dr. D. Fridline) [123].

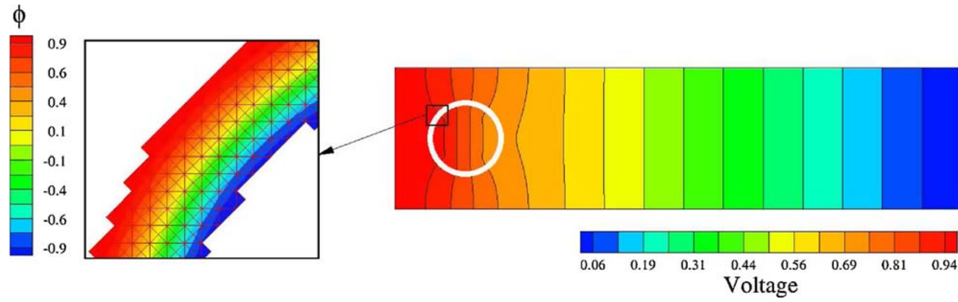

Fig. 24. Void evolution in an interconnect line. The zoomed region shows counters of the order parameter field along the interface layer (courtesy of Dr. D. Bhate) [129].

and changes across a narrow interfacial layer. The void surface of the sharp interface model is approximated by an interface of small width.

To model realistic interconnect failures further extensions of the diffuse interface model are necessary. There are several mechanisms of mass transport in interconnects besides surface diffusion, including lattice diffusion, grain boundary diffusion, and diffusion along the interface between the interconnect and the surrounding layers. All of these mechanisms are included in the diffuse interface model presented by Bhate et al. in 2000 [128,129]. The diffuse interface order parameter ϕ is governed by an extended Cahn–Hilliard equation [130,131]. The Cahn–Hilliard equation is known to provide a diffuse interface representation for surface diffusion. The order parameter evolves in response to gradients of chemical potential and EM.

The chemical potential is derived from a free energy functional that depends on the order parameter, its gradient, and strain

$$F(\phi, \bar{\bar{\varepsilon}}) = \int_V \left(\frac{2\gamma}{\epsilon\pi} \left(f(\phi) + \frac{1}{2}\epsilon^2 |\phi|^2 \right) + w(\phi, \bar{\bar{\varepsilon}}) \right) \mathrm{d}V \tag{165}$$

ϵ is a parameter that controls the thickness of the interfacial layer associated with the void surface and $f(\phi)$ is the free energy of the unstrained, homogeneous solid (Fig. 25).

Blowey and Elliott [130,131] set the free energy $f(\phi)$ as a non-smooth double obstacle potential of the form

$$f(\phi) = \frac{1}{2}(1 - \phi^2) + I_{[-1,+1]}(\phi) \tag{166}$$

where $I_{[-1,+1]}$ denotes the indicator function which constrains the order parameter ϕ to +1 in the metal region and -1 in the void region.

$$I_{[-1,+1]} = \begin{cases} \infty & |\phi| > 1 \\ 0 & |\phi| \le 1 \end{cases} \tag{167}$$

The governing equation for the evolution of a void described by the order parameter ϕ reads [128]

$$\frac{\partial \phi}{\partial t} = \frac{2D_s}{\epsilon\pi} \nabla \cdot (\nabla \mu_s - Z^* e \nabla \varphi) - \frac{4A}{\epsilon\pi}(1 - \phi^2)(\mu_s + \mu_v). \tag{168}$$

μ_s is the chemical potential of an atom in the interfacial region defined as

$$\mu_s = 2\Omega \frac{\delta F}{\delta \phi} = 2\Omega \left(\frac{2\gamma}{\epsilon\pi} (f'(\phi) - \epsilon^2 \Delta\phi) + \frac{\partial w}{\partial \phi} \right) \tag{169}$$

and A is the kinetic parameter controlling the rate of transfer between the surface and the bulk. μ_v is the bulk chemical potential of vacancies. Bhate et al. [128,129] also describe finite element schemes to solve the modified Cahn–Hilliard Eq. (168), as well as the equations associated with the accompanying mechanical, electrical, and bulk diffusion problem. An asymptotic analysis carried out by Bhate et al. [128] demonstrates that for $\epsilon \to 0$ the motion of a void evolving by coupled surface and lattice diffusion, driven by stress, electron wind, and vacancy concentration gradients converges to the sharp interface description. Bhate et al. [128,129] have simulated two-dimensional void evolution agreeing closely with equivalent sharp interface simulation results (Fig. 24).

The main disadvantage of diffuse interface models [129,125] is their requirement of structured underlaying meshes for the order parameter evaluation to reach sufficiently high resolution of the order parameter profile in the void-metal interfacial area. To overcome this drawback the diffuse interface model governing equation can be solved with a finite element scheme coupled with a mesh adaptation algorithm [132]. The robustness of this finite element approach with respect to the underlying mesh makes it possible to efficiently simulate the damage induced by EM in complex interconnect structures.

Eq. (168) is solved by means of the finite element method [132] on a sequence of meshes each one adapted to the position of the void-metal interface in time. The initial mesh is produced by refinement of a basic triangulation according to the initial profile of the order parameter ϕ. The motivation of mesh adaptation is to construct and maintain a fine triangulated belt of width $\epsilon\pi$ in the interconnect area, where the void-metal interface area is placed.

The initial order parameter profile depends on the initial shape of the void $\Gamma(0)$ and can be expressed as:

$$\phi(x, y) = \begin{cases} +1 & \text{if } d > \frac{\epsilon\pi}{2} \\ \sin\left(\frac{d}{\epsilon}\right) & \text{if } |d| \le \frac{\epsilon\pi}{2} \\ -1 & \text{if } d < -\frac{\epsilon\pi}{2} \end{cases} \tag{170}$$

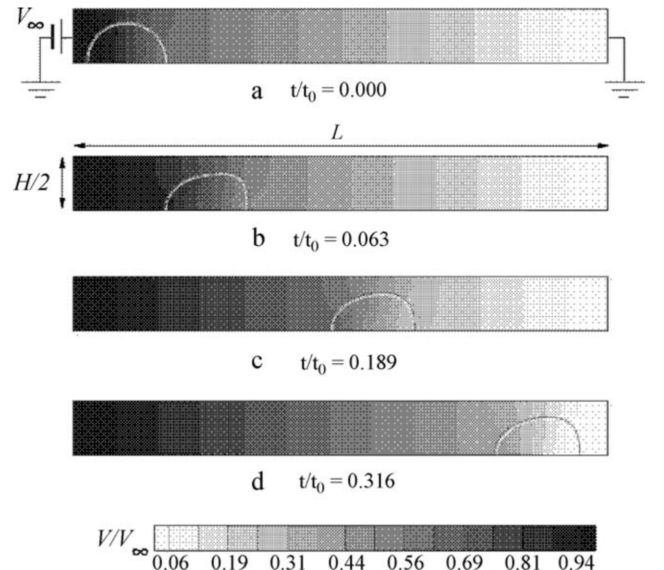

Fig. 25. Migration of a stable circular void evolving to an arrowhead shape in a stress-free, electrically conducting strip [129].

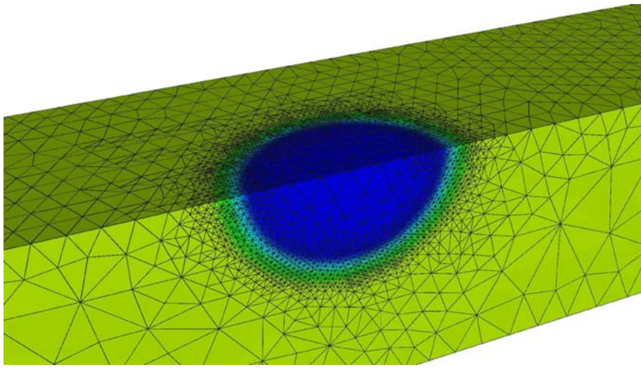

Fig. 26. Adaptively refined mesh at the void/metal interface.

$d = dist(P(x, y), \Gamma(0))$ is the signed normal distance of the point $P(x, y)$ from the initial interface $\Gamma(0)$.

Many simulations have shown that for all considered initial void radii, voids follow the electric current direction and do not transform in slit-like or wedge-like like formations which have been found to be the main cause for complete interconnect failure [124].

Theoretical and numerical concepts for void evolution open a way for an accurate calculation of the failure times as well as the resistance change until failure [132]. However, the numerical implementation of algorithms which describe the evolution of void surfaces is generally very demanding.

In order to model void growth and its influence on interconnect resistance in three dimensions a simplified version of the diffuse interface model is proposed [133].

The void shape is built as an intersection of a sphere with the interconnect geometry, cf. Fig. 27. The electric field around the void is calculated by setting an order parameter ϕ dependent conductivity

$$\rho(\phi) = \frac{\rho_{Cu}(1+\phi)}{2}, \tag{171}$$

where ρ_{Cu} is the conductivity of copper bulk. As in the two-dimensional case, the finite element mesh along the void-metal interface is refined (Fig. 26). During the simulation the size of the void is gradually increased and for each void size the normal speed of the void surface is estimated [133]. Simultaneously, the interconnect resistance is calculated. The whole process is stopped, when a void radius is reached for which $100 \times (R_{actual}/R_{initial} - 1) > 20\%$.

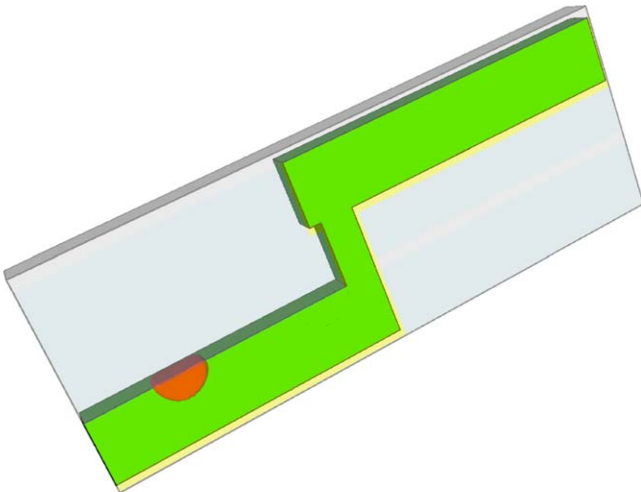

Fig. 27. Position of the growing void. Initial position and volume are chosen on the basis of experimental results.

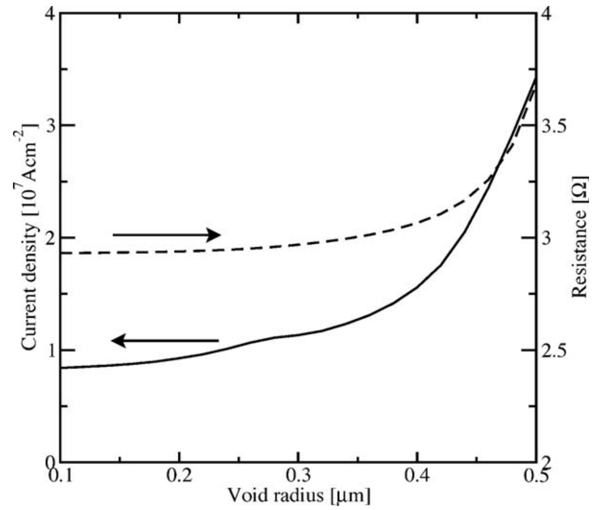

Fig. 28. Change of the average current density and via resistance depending on the void radius.

A typical simulated current density and resistance change are presented in Fig. 28.

3.7. Integration of atomistic and continuum-level models

The interconnect scaling and the introduction of new processes and materials raise an issue of justifiability and applicability of phenomelogical continuum-level models. The parameters of continuum-level EM models are averages over values which generally vary on microscopic and atomistic scale. The question is under which conditions these microscopic or atomistic spatial variations influence the validity of continuum models. Regarding both important parameters of continuum-level EM models, effective valence Z^* and vacancy diffusivity, there is variation depending on crystal orientation and variation between bulk, grain boundaries, and interfaces. Variations on the atomistic scale for the current level of miniutarization does not play an important role, since, for example, interconnect width are several dozens of nm while effective valence varies at the scale of atomic distances (10^{-1} nm).

In the modeling of EM the primary motivation for connecting the atomistic and the continuum-level description is to enable a correct parameterization of the continuum-level models. Experimental methods for the determination of the effective valence are based on two approaches: one is the compositional change induced by the current flow and the other measures the mass transport relative to a fixed reference frame. The principles of these two types of measurements apply to bulk materials as well as thin films [134]. The method based on the compositional change is more complex but also more accurate. One of the reasons for the higher accuracy is that it is not necessary to initially determine a self-diffusion coefficient, which may cause an additional error. The determination of self-diffusion coefficient is part of the simpler mass transport method. The value of the effective valence Z^* can be reliably determined experimentally only for the bulk of metals [135]. Extending experimental methods for grain boundaries and interfaces demands additional, often questionable assumptions [134]. An important result of experimental EM studies is the anisotropy of the effective valence along different crystalline axis.

3.7.1. Parametrization of continuum-level models

The most direct way to include results of atomistic simulation into a continuum-level model is through the calculation of the

effective valence Z^*. Electromigration, on the atomistic level, includes a complex multi-scattering process, where local fields and the local configuration of atoms play a decisive role. The quantum mechanical expression for the calculation of the electron wind force is obtained from (22) and (23),

$$\vec{F}(\vec{r}) = \frac{e\Omega}{4\pi^3} \iint_{\mathrm{FS}} \frac{\mathrm{d}S_k}{|\nabla_k \mathcal{E}_k|} \tau(\vec{k}) \vec{v}(\vec{k}) \cdot \vec{E} \iiint d\vec{r} \psi_k(\vec{r})^* \nabla_R V(\vec{r} - \vec{R}) \psi_k(\vec{r}), \qquad (172)$$

where Ω is atomic volume, V is the interaction potential between an electron and the migrating atom, $\psi_k(\vec{r})$ are the scattering states for electrons in the absence of an external electric field, $\vec{v}(\vec{k})$ is the electron group velocity, $\tau(\vec{k})$ is the relaxation time due to scattering by phonons, and $\vec{E}$ is the external electric field. The first integration is over the Fermi surface and the second over the volume of the crystal.

There are several different approaches for the calculation of the wind force (172), where the most promising and the most sophisticated is the Koringa–Khon–Rostoker (KKR) method [136]. KKR is band-structure calculation method based on Green's function techniques. One of the difficult issues in electronic structure calculation is to take into account the polyhedral shape of the unit cell. To avoid this difficult boundary value problem Green's function techniques are used, as in KKR method, where the Schrödinger equation is transformed into an integral equation.

In general, the microscopic force-field depends on the position of the atom along the diffusion jump path. The appropriate driving force, to be used in continuum-level electromigration models [82], is the average of the microscopic force over the i-th diffusion jump path between locations $\vec{r}_{i,1}$ and $\vec{r}_{i,2}$ [137]

$$\vec{F}_m = \left\langle \frac{1}{|\vec{r}_{i,2} - \vec{r}_{i,1}|} \int_{\vec{r}_{i,1}}^{\vec{r}_{i,2}} \vec{F}(\vec{r}) \cdot d\vec{r} \right\rangle, \qquad (173)$$

where the outer brackets indicate that an average is to be performed over the set of all equivalent diffusion jump-paths, i.e., paths that have the same activation energy or diffusion coefficient in the absence of an electric field and electron current.

3.7.2. Molecular dynamics of electromigration

Molecular dynamics (MD) enables a study of EM on a more fundamental level which goes beyond the calculations of parameters but also includes an insight in the fundamental transport properties for different atomistic configurations. On such a way the validity of a particular application of continuum-level models can be assessed, especially, when one also has to deal with point defect annihilation and production processes. There are just very limited studies in the literature involving atomistic simulations. A MD study of electromigration was carried out in [138], where periodic boundaries for interconnects were constructed and two-dimensional MD simulations were carried out for aluminum. In that study the electromigration driving force was calculated using the Cloud In Cell (CIC) method and an evolution of void formation was reported.

In [139] the grain boundary diffusion for aluminum interconnects was characterized by MD, where the diffusion characteristics with respect to the grain boundary angle were reported. In [140] the void evolution and failure in metallic thin films was studied, whereas plastic deformations in the vicinity of the voids were examined by the use of MD.

The work in [141] and [142] combines the MD approach with the EM force calculation by Sorbello [20]. For this purpose the General Utility Lattice Program (GULP) was used [143]. The pair potential $V(r)$ between Al atoms separated by a distance r was calculated as

$$V(r) = \frac{Z^2 e^2}{r} \left(1 - \frac{2}{\pi} \int_0^\infty \left(1 - \frac{1}{\varepsilon} \right) M^2(q) \frac{\sin(qr)}{qr} dq \right), \qquad (174)$$

$$M^2(q) = \frac{\Omega q^2}{4\pi e^2} |W_0(q)|^2, \qquad (175)$$

where M is the wave number characteristics, Z is the electronic charge of the atom, Ω is the atomic volume, q is the Fourier space vector, ε is the Hartree dielectric function, and W_0 is the bare ion pseudopotential factor [144,145]. The potential above has been chosen in [141,142], because it predicts the value of lattice parameter within an excellent 3% error. However, this potential produces a large discrepancy between experimental and simulated elastic constants, which makes its applicability to any EM/stressmigration related simulation very questionable. Two-body potentials generally overestimate elastic constants because of the lack of many body interactions and for future simulations the usage of many body potentials is advised.

The electromigration force was calculated with the pseudopotential approach described by Sorbello [20], where the electromigration force on an atom j due to an applied electric field depends on the impurities and vacancies in the lattice. Sorbello expressed the electron scattering force on an ion j in terms of a potential U_j as

$$F_j = -\frac{\partial U_j}{\partial R_j}, \qquad (176)$$

$$U_j = -\sum_{n_{\mathrm{vacancies}}} u_{jn} + \sum_{i_{\mathrm{impurities}}} u_{ji} \qquad (177)$$

where u_{jk} has to be defined for all possible cases of pair interactions [20]. The calculated electromigration force is then added to the force obtained from the interatomic interactions and included in the integration of the equation of motion. This added force perturbs the system, which causes non-equilibrium conditions to be imposed, resulting in a continuous increase in temperature. Thus, in order to keep the temperature constant, the system was coupled to a heat bath.

To characterize diffusion under EM force, the authors have determined the atomic jump frequency. EM causes an increase of the jump frequency in electron flow direction, which is interpreted by lowering of the corresponding energetic barrier by an amount of work by the EM force.

The combination of MD with quantum-mechanical calculations of the EM microscopic force is interesting for several reasons. First, it is possible to calculate material flux directly on the atomistic level and to compare results with continuum-level calculations. This comparison will eventually lead to a modification and improvement of the continuum-level description for EM in domains with specific microstructural features.

Furthermore, an interaction of EM with stressmigration and EM in the presence of point defects annihilation and production sites can be directly simulated on the atomistic level. This kind of simulation can be very useful for the construction of new continuum-level models.

However, the presented method relies on EM force calculations based on pseudopotential theory with the obvious restriction of being applicable only to periodic crystals within the weak potential regime. The most interesting cases of EM induced transport in the presence of dislocations, grain boundaries, interfaces, and surfaces, cannot be handled with a pseudopotential-based approach.

The first attempt to deal with EM in extended defects was undertaken by Sorbello [137,146]. He considers grain boundaries

and dislocations as disordered regions confined to slab-like domains. Point defects are presented by delta function potentials and scattering states are calculated using the free electron "jellium model" approach [137]. Even if the applied model is very rough, it enables some interesting insights into the nature of EM in grain boundaries and dislocations. For example, model predicts drop of effective valence inside the grain boundary and the effective valence dependence on angle between grain boundary and current flow direction.

In order to fully exploit the capability of MD, the more accurate calculation of EM wind force is necessary. One possible way to go is an utilization of the Koringa–Khon–Rostoker (KKR) method [136,147].

3.7.3. EM force calculation in grain boundary

The KKR method has proven to be a powerful tool for the calculation of the EM force in crystal bulk and on crystal surfaces. It was a natural step to extend this method to other crystal heterogenities, like dislocations and grain boundaries. An important simplification of the original KKR approach [136] was carried out in [147], where a muffin-tin representation of the crystal bulk was replaced by a jellium model and heterogenities were represented by a cluster of isolated atoms embedded in jellium. As an illustration of these method we give a draft of a scheme for the calculation of the EM force on an atom in the vicinity of a grain boundary. The momentum transfer between the atom and the current carrying electrons is influenced by multiple scattering of the electrons on the atom and the cluster. The grain boundary itself can be constructed by the method of molecular statistics as described in [68].

The grain boundary is modeled as an atomic cluster embedded into the crystal bulk modeled as jellium (Fig. 29). From (172) it is apparent that a calculation of the wind force requires a self-consistent determination of the single particle states of the system at the Fermi energy ψ_k, and the effective one-electron potential in the vicinity of the test atom. In order to calculate these quantities it is necessary to self-consistently solve the Schrödinger equation for the atomic cluster in jellium,

$$\left(-\frac{\hbar}{2m}\nabla^2 + V(\vec{r})\right)\psi_k(\vec{r}) = \mathcal{E}_k\psi_k(\vec{r}). \tag{178}$$

The effective potential $V(\vec{r})$ is given by [147]

$$V(\vec{r}) = V_+(\vec{r}) + e^2\int d\vec{r'}\,\frac{n_0(\vec{r})}{|\vec{r}-\vec{r'}|} + V_{xc}[n_0(\vec{r})], \tag{179}$$

where $V_+(\vec{r})$ is the Coulomb potential generated by the positive jellium background and the ion cores of the atoms inside the cluster. V_{xc} is the exchange-correlation potential evaluated within the local-density approximation and n_0 is the ground state electron density

$$n_0(\vec{r}) = \sum_k \psi_k(\vec{r})\psi_k^*(\vec{r}). \tag{180}$$

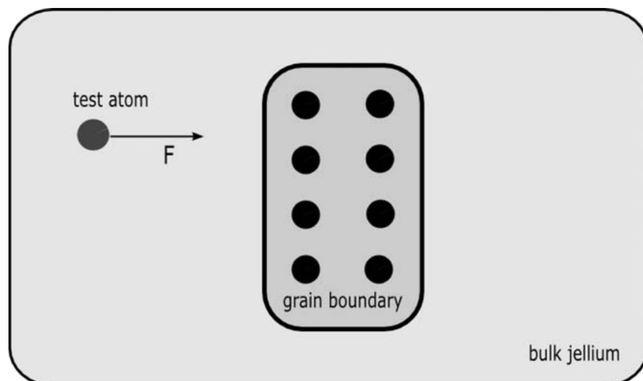

Fig. 29. A schematic illustration of a test atom interacting with an atomic cluster embedded in jellium.

The effective potential in the vicinity of the test atom is replaced with a spherical potential of muffin-tin form. Inside the muffin-tin, the Schrödinger equation is solved and the obtained wave function surrounding the test atom has to fulfill a continuity condition at the muffin-tin surface. The wave function continuity can be enforced by expanding the solution of the Schrödinger equation into spherical harmonics and a suitable choice of the free parameters of expansion. In such a way the wave function ψ_k is defined in the whole simulation domain and can then be used for the calculation of the EM force by (172). The above described procedure turned out to be accurate through comparison with a calculation performed by the layer-KKR method for the case of surface EM [147] of Na.

3.8. Usage scenarios for simulation

Competitive reliability targets of chip failure rates are in the order of one per thousand throughout the anticipated life time. The central problem of interconnect design for reliability is the determination of the long term interconnect behavior.

The analysis of EM reliability with Technology Computer Aided Design (TCAD) has to be carried out on at least two levels. The first level is a physical one, that means application of most complete and comprehensive models to interconnect portions of moderate size. The restriction in size and complexity arises from the capacity of computers (memory, computational time), but has also a cause in numerical issues. The first level analysis is based on the simulation of the behavior of characteristic portions of the interconnect, which, known from experiments, represent a high EM risk. The goal of the analysis by simulation is to determine the time-to-failure distribution for this specific interconnect part.

The second level analysis combines the results of the first level in order to assess EM reliability of an entire chip. If the first level analysis $\mathrm{PDF}_k(t)$, $k = 1, \ldots, N$ (Probability Density Function) provides a time-to-failure distribution for each of N characteristic parts of the interconnect, the cumulative time-to-failure distribution $\mathrm{CDF}(t)$ (Cumulative Distribution Function) for the entire chip is [28,53,148]:

$$\mathrm{CDF}(t) = 1 - \prod_{k=1}^{N}\left[1 - \int_0^t \mathrm{PDF}_k(t')\,dt'\right]. \tag{181}$$

Although there is no stated industry standard, competitive reliability targets of chip failure have been $\mathrm{CDF}(t) < 0.1\%$ for a time of $t = 10$ years or $t = 15$ years.

Simulation can be used for extrapolation of long time interconnect behavior on the basis of results of accelerated EM tests. This capability goes clearly beyond an extrapolation by standard statistical methods which rely on Black's equation and extrapolate a time-to-failure for a single interconnect structure. The usage of TCAD tools enables a prediction of the behavior for structures which are obtained by variation of geometrical properties and operating conditions of a previously used initial test structure.

The assumed scenario for application of an EM reliability TCAD tool is:

- *Model Calibration*. For this purpose we use one layout and many test units. At the end of calibration all parameters of the model are fixed. During this process, different microstructures are considered and simulation parameters are varied with the goal to reproduce experimental failure time statistics, Fig. 30.

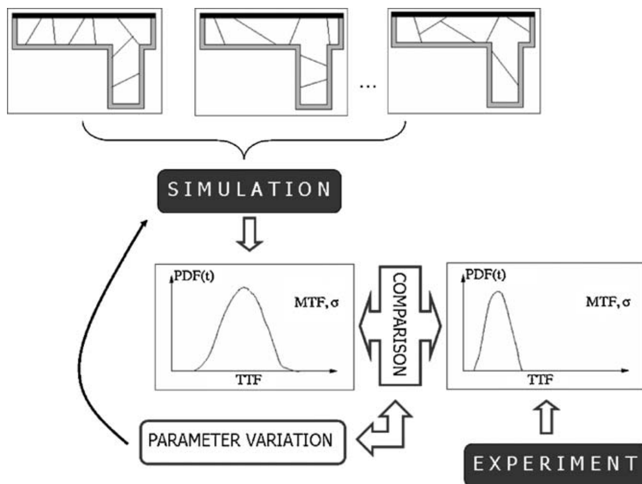

Fig. 30. Electromigration model calibration using a multitude of microstructural inputs.

- *Model Application*. The calibrated model is used for simulation. The simulation extrapolates the behavior of the interconnect under real life conditions.

For a given interconnect layout and monocrystalline material, simulation will provide a unique time-to-failure. All impact factors, e.g. geometry of the layout, bulk diffusivity, interface diffusivity, and mechanical properties, are deterministic and so time-to-failure is deterministic. However, the situation changes, when the interconnect possesses a microstructure. The microstructure has a significant impact on EM, since it introduces a diversity of possible EM paths and local mechanical properties (the Young modulus and Poisson factor depend on the crystal orientation in each grain). However, the microstructure itself cannot be completely controlled by a process technology. In other words, the position of grain boundaries, angles in which they meet the interfaces, etc. cannot be designed, the process itself determines only statistics of grain sizes and textures.

If we extract statistical properties of the microstructure obtained by a specific process used for producing a test structure and use these properties to design an input for simulation tools, the resulting time-to-failure distribution from the simulation with these inputs has to fit the experimental distribution. If this is not the case, the configurable parameters of the model have to be varied, until the simulated time-to-failure distribution fits the experimental one. When a reasonable agreement between the experimentally determined time-to-failure distribution and the simulated time-to-failure distribution is reached, the TCAD tool is considered as calibrated and can be used for EM reliability assessment under realistic operating conditions.

4. Electromigration simulation studies

4.1. Electromigration in redundant vias

In order to reduce EM effects, efforts have been spent in developing new integration processes and investigating different materials which produce exibit properties. Such efforts led from originally aluminum interconnects to aluminum-copper alloys, and later to pure copper interconnects fabricated by a dual-damascene technology. The material design encompasses not only the choice of an appropriate interconnect metal, but also the choice of its surrounding materials. Another strategy pursued to improve the EM behavior is the introduction of specific geometrical features, such as material reservoirs [8,149,150] and redundant vias [28,151]. The effect of these geometrical features has been more widely investigated for stress migration than for EM. The experiments have shown that stress migration failure is also determined by vacancy transport and mechanical stress build-up.

Ogawa et al. [149] introduced the concept of "active diffusion volume", which is the intersection between the interconnect volume, the diffusion volume, and the stress gradient region, to explain the increased lifetimes observed in structures where the vias were contacted to wide lines. However, Kouno et al. [152] found shorter lifetimes for structures with narrow line extrusions, arguing that the interfaces between copper, barrier, and capping layer act as one-dimensional paths for vacancy diffusion, which are faster compared to the two-dimensional vacancy flow in a wide plate and, therefore, the active diffusion model does not apply.

Using two or more via contacts between interconnect levels has shown to be a very promising geometrical strategy for preventing stressmigration [28,151] and EM [28]. However, the complete understanding, why such geometrical features really enhance interconnect reliability, is still lacking.

Yoshida et al. [151] were the first to closely investigate the effect of redundant vias on stress migration. In their work, no stress migration failure was detected, when two neighboring vias were used, because the nucleation of a void underneath the first via relaxes the stress also under the second one, suppressing the driving force for new void formation. Yoshida et al. [151] based their explanation on the concept of active diffusion volume [149].

We consider two cases. First we assume a strengthened copper/capping layer interface [71]. In such case the adhesion between copper and capping layer is strong and, therefore, grain boundaries can be considered as the main paths for diffusion. This situation is modeled by setting an effective diffusion coefficient as $D_{eff} = 1000 D_b$, where D_b is the bulk diffusivity of copper.

$$D_b = D_0 \exp\left(-\frac{E_a}{kT}\right) \tag{182}$$

with $D_0 = 0.52\ \mathrm{cm}^2/\mathrm{s}$ and $E_a = 1.1$ eV [71].

In the second case, we consider the copper/capping layer interface as the main diffusion path, where we have set $D_{int} = 100 D_{eff}$.

The simulations were carried out for an average current density of 8 MA/cm^2 and a temperature of 300 °C. We have used the following parameters:

- Cu: $Z^* = 4$, $f = 0.4$, $\Omega = 1.182 \times 10^{-23}\ \mathrm{cm}^3$, $E = 125$ GPa, $\nu = 0.34$;
- Ta: $E = 380$ GPa, $\nu = 0.27$;
- Si_3N_4: $E = 380$ GPa, $\nu = 0.27$;

The interconnect structure is shown in Fig. 31. The lower line has a cross-section of $0.5 \times 0.2\ \mu\mathrm{m}^2$, the barrier and the capping layer are 25 nm thick. The thickness of the SiO_2 passivation is 500 nm on the top and bottom of the interconnect.

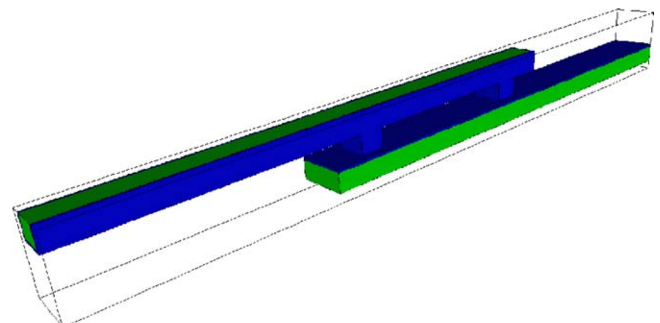

Fig. 31. Dual-damascene interconnect structure.

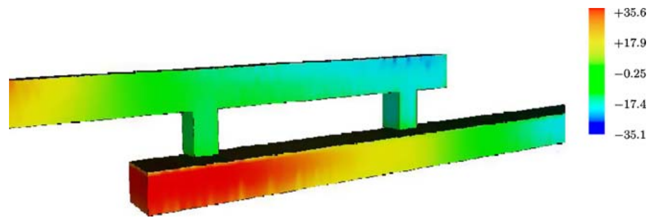

Fig. 32. Detail of the hydrostatic stress distribution in the via region (in MPa).

Fig. 32 shows the hydrostatic stress distribution for the double via structure. The electron flow is from the upper to the lower metal line (downward flow), and, therefore, it is expected that the vacancies accumulate right under the via region at the lower line. As the vacancy has a smaller volume than the metal atom and due to the constraints imposed by the attaching layers and passivation, the accumulation of vacancies in this region leads to the production of local tensile stresses.

The stress build-up for the single via and for the double via structure for two different distances between the vias is shown in Fig. 33. We have observed that the maximum stress developed for the structure with redundant vias is higher than that for the single via. Such a behavior occurs, because the voltage applied at the ends of the interconnect is kept constant and the addition of the second via reduces the interconnect resistance and increases the electrical current. Consequently, the driving force for material transport along the line is increased, and more vacancies concentrate under the left via of the redundant via structure, producing a higher stress.

Fig. 33 shows that the stress also increases as the distance between the vias becomes larger. It should be pointed out that the maximum vacancy concentration and stress is always located at the bottom of the outer via. However, for the redundant via it is expected that the electric current crowds at the innermost via, where more vacancies should accumulate and produce a higher stress. Thus, our results suggest that the current crowding does not suffice to induce a higher vacancy flux divergence at the inner via.

These results suggest that a void nucleates sooner for the redundant via structures. Moreover, as for small distances the stress magnitudes under both of the vias are very similar, a void could nucleate in either the left or the right via. If the void nucleates under the right via, its subsequent growth can span the lower line thickness leading to the interruption of electric current flow in the line, and the interconnect fails even with the redundant via. However, increasing the distance the stress under the right via is significantly reduced, and it can be expected that a void nucleates only under the left via. The associated stress relaxation hinders a void nucleation under the second via, and an increase in the interconnect mean time-to-failure is observed [28,151].

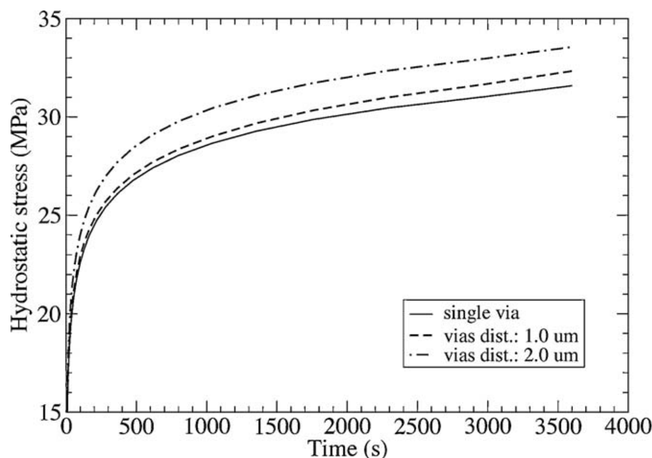

Fig. 33. Maximum hydrostatic stress (tensile) developed under the left via.

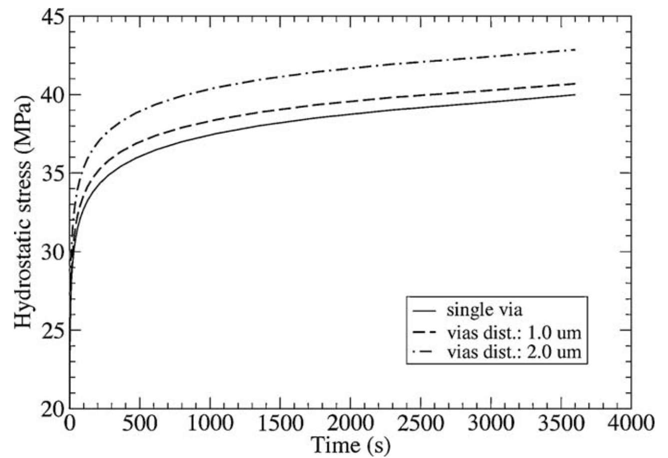

Fig. 34. Maximum hydrostatic stress developed under the left via when the copper/capping layer interface is the main diffusion path.

Experiments [153] have shown that the copper/capping layer interface is frequently the main path for material transport in copper dual-damascene interconnects. In order to model this effect, the diffusion coefficient in this interface is increased by a factor 100 in relation to the effective diffusivity of the last section. The corresponding stress build-up is shown in Fig. 34.

We can see that the stress values are increased by considering the interfacial diffusion as the dominant mechanism. Moreover, the site where the vacancies concentrate and the maximum stress develops has also changed, similarly to the work of Kouno et al. [152] for stress migration. This is clearly seen in the vacancy concentration and stress distribution in Fig. 35 and Fig. 36, respectively, where we can observe a peak of vacancy concentration and stress also at the border of the inner via.

Two facts are responsible for this behavior: the first one is the current crowding which is expected to occur at this region, and the second one is that the intersection between copper, barrier and

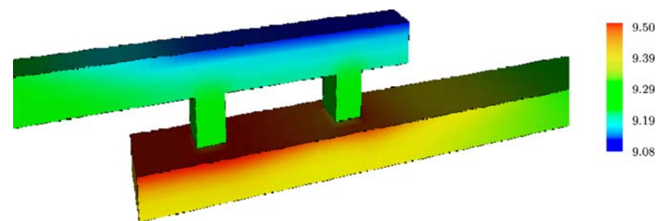

Fig. 35. Vacancy distribution in the double via structure (in 10^{15} cm^{-3}).

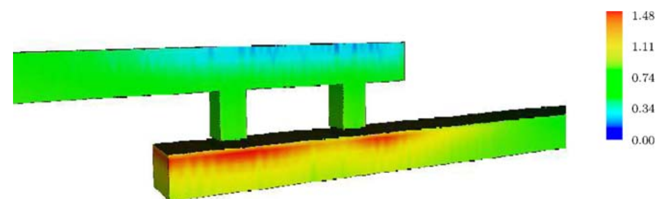

Fig. 36. Early hydrostatic stress distribution under the vias in the double via structure (in MPa).

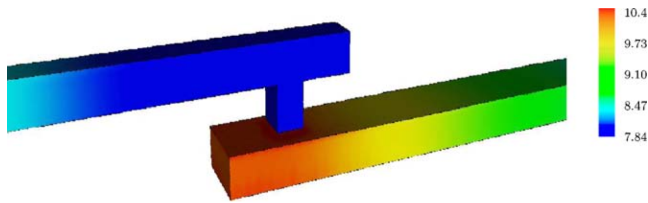

Fig. 37. Vacancy concentration in the single via structure after 1h of EM stress (in 10^{15} cm^{-3}).

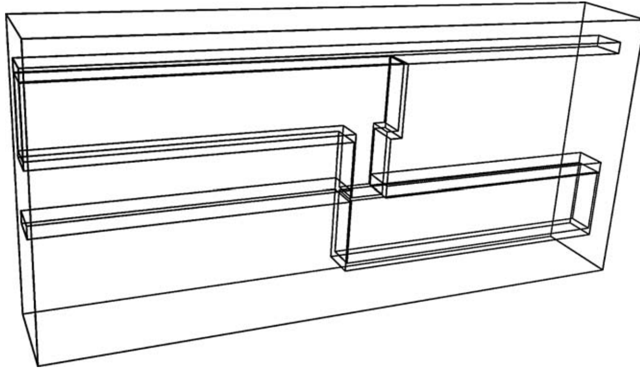

Fig. 38. Dual-damascene layout used. Top and the bottom of the structure are mechanically fixed for thermomechanical simulation.

capping layer constitutes a site of flux divergence due to a faster diffusion along the copper/capping layer interface in comparison to the copper/barrier layer interface.

However, over time the vacancy concentration and stress in this region increase, leading to the development of significant gradients. Since these gradients also act as driving forces for material transport, they prevent the continuous accumulation of vacancies driven by the EM force and, in addition, help to increase the flux of vacancies through the whole line thickness. This effect is shown in Fig. 37.

4.2. Stress-dependent electromigration

The impact of thermo-mechanical stress on EM induced vacancy transport is illustrated with a typical dual-damascene interconnect structure (Fig. 38). Generally, each portion of interconnect is embedded in a surrounding which has spatially varying mechanical properties. This is caused by the three-dimensional character of interconnect layouts as well as different mechanical properties of materials used for dielectric, barrier, and capping layer. The materials and their properties are the same as in Section 4.1.

The mechanical complexity of the interconnects surrounding is modeled by setting appropriate mechanical boundary conditions (Fig. 38). The layout under consideration is bounded by a rectangular box (800 nm × 100 nm × 400 nm), the top and the bottom of the box are mechanically fixed (Fig. 38). Before starting an actual EM simulation a thermo-mechanical simulation is carried out. The layout is cooled down from 120 °C to 20 °C. Due to mismatch of the thermal expansion coefficients of the different materials a mechanical stress is built up. In Fig. 39 the σ_{xx}, σ_{yy}, and σ_{zz} components of the thermal stress tensor are shown, respectively. As we can see, due to the boundary conditions, the stress is anisotropic. Inside the interconnect the stress is tensile, however, due to the geometry and boundary conditions the area of high tensile stress (over 400 MPa in Fig. 39) is spread throughout the via.

Stress influences EM in two ways (Section 3.3) – it is an additional driving force and its presence is a source of anisotropy in diffusion. The importance of stress as a driving force was early recognized [29–31] and since then regularly included in EM models [70,86]. However, from the atomic point of view, the effect of stress as a driving force cannot be separated from the effect of crystal lattice distortion due to stress [101]. In order to demonstrate the influence of stress, we compare the vacancy distribution modeled with a simple pressure-dependent scalar diffusivity (Fig. 40a) with one obtained considering stress dependent tensorial diffusivity (Fig. 40b). In both cases we have simulated upstream EM with an applied current density of 8 MA/cm^2. It can clearly be seen in Fig. 40 that the anisotropic diffusivity causes a significantly more widespread area of high vacancy concentration (threshold of $5e16$ cm^{-3}) than in the case of scalar diffusivity. Wider areas of atom depletion probably match weak adhesion spots at capping/interconnect interfaces and induce void nucleation.

4.3. Electromigration statistics

Experiments have shown that EM times-to-failure obey a lognormal distribution. Although the origin of such a distribution is not entirely clear, the copper grain sizes seem to follow lognormal distributions in typical dual-damascene process technology [154]. Therefore, this has been considered as the major cause for the lognormal distribution of EM. The understanding of the EM lifetime distribution is crucial for the extrapolation of the times-to-failure obtained empirically from accelerated tests to real operating conditions, as performed by a modified form of the Black equation [154]. Also, it has been shown that the microstructure plays a key role regarding the failure mechanisms in copper dual-damascene interconnects [155]. It affects EM in different ways. Grain boundaries are natural locations of atomic flux

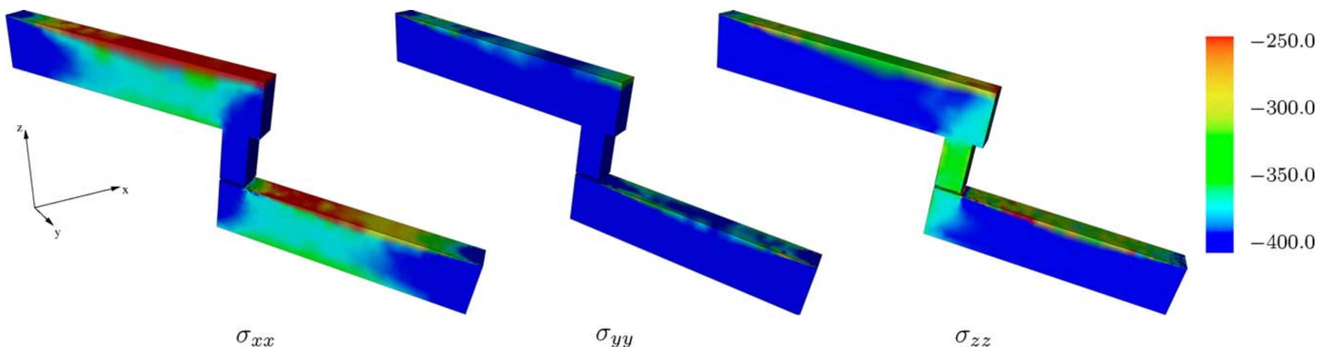

Fig. 39. Components of thermomechanical stress tensor [MPa].

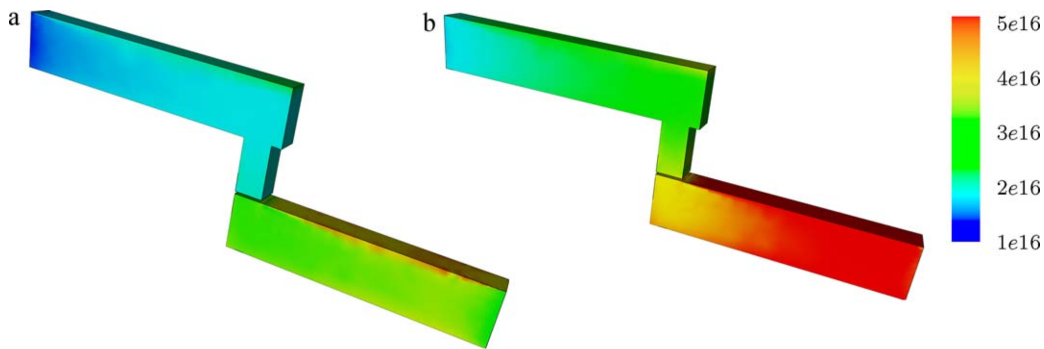

Fig. 40. Vacancy distribution after 10 min for the case of isotropic scalar diffusivity (a) and anisotropic tensorial diffusivity (b) [cm^{-3}]

divergence, they act as fast diffusivity paths for vacancy diffusion [72] and as sites of annihilation and production of vacancies [68].

In this section we investigate the origin of the statistical distribution of EM times-to-failure as a function of the distribution of copper grain sizes. The effect of lognormal grain size distributions on the distribution of EM lifetimes of fully three-dimensional copper dual-damascene interconnect structures is studied based on numerical simulations. Simulation tool include advanced EM models presented in Sections 3.1–3.3.

For the generation of input geometries and microstructures for the EM simulation tool a microstructure generator tool has been developed. Given a specific interconnect structure and providing the tool with a median grain size and corresponding standard deviation, it generates a lognormal distribution of grain sizes. Then, following this distribution, the interconnect line is cut along its length by the planes that form the grain boundaries. Furthermore, the angles between the grain boundaries' planes and the line surface follow a normal distribution with median value of 90°. The corresponding standard deviation can also be specified.

In Fig. 41 we present the schema of the simulation procedure. Three standard deviations for the distribution of grain sizes are considered, namely 0.1, 0.3 and 0.6. For each of them 20 dual-damascene interconnect structures were. As the interconnect line is assumed to present a bamboo-like structure, the median grain size is equal to the line width, 0.10 μm. The barrier, capping and interlayer dielectric layers are Ta, SiN, and SiO_2, respectively. The corresponding interconnect structure is shown in Fig. 42.

The applied current density is 1.5 MA/cm^2, and the temperature is 300 °C. We have used a stress threshold value as failure criterion, which means that the EM time-to-failure represents the time for a void nucleation to occur. Thus, the time-to-failure is determined by the time for the stress to reach a given threshold value at some intersection between a grain boundary and the SiN layer. Such a failure criterion is equivalent to a very small resistance increase criterion, which is commonly used in experiments.

Fig. 44 shows the hydrostatic tensile stress development for the structures with grain size standard deviation of 0.3. The stress peak value follows the peak of trapped vacancy concentration and is located at the intersection of grain boundaries with the capping layer, as shown in Fig. 43.

Collecting the times-to-failure from Fig. 44 and calculating the cumulative failure percentages resulted in lognormal distributions

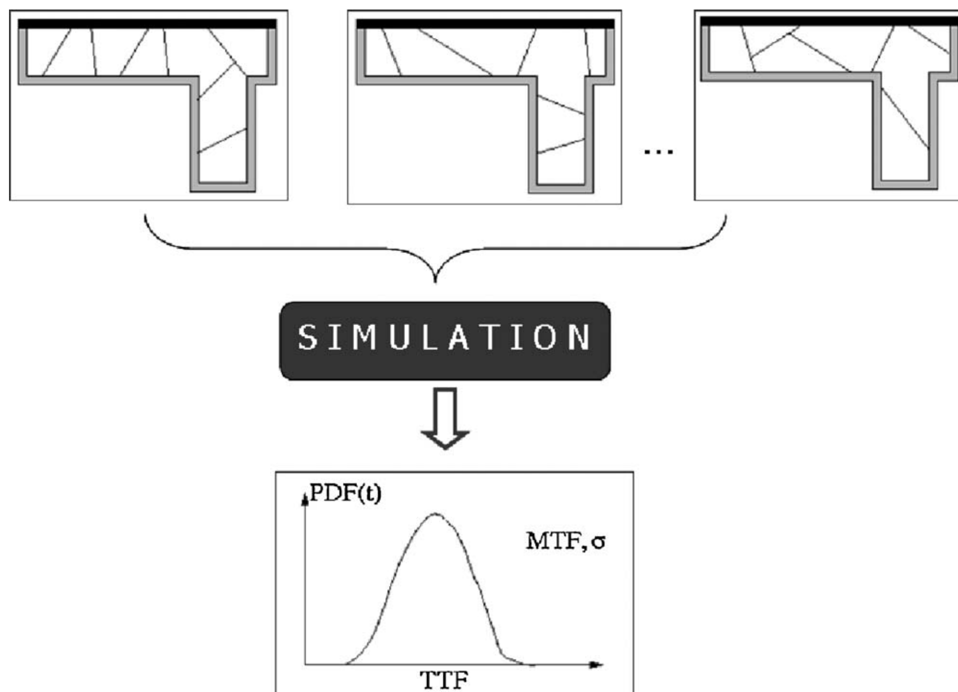

Fig. 41. Schematic simulation procedure.

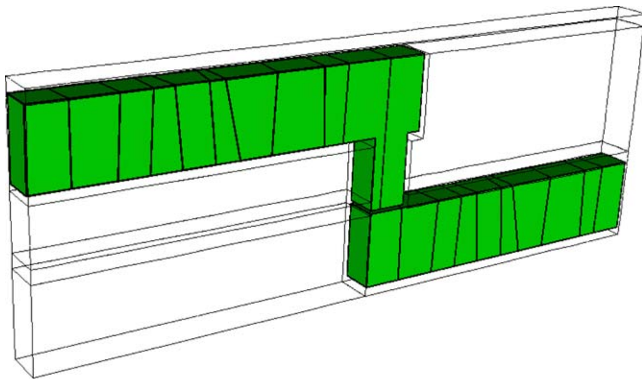

Fig. 42. Dual-damscene interconnect structure.

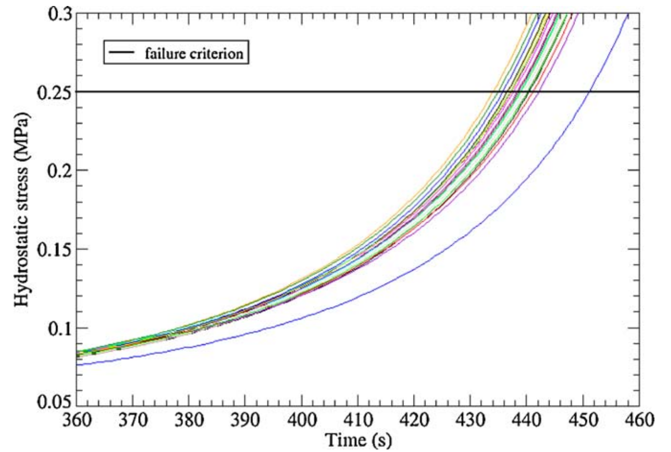

Fig. 44. Peak of hydrostatic stress development for the set with grain size standard deviation of 0.3.

of EM lifetimes, as shown in Fig. 45. The obtained standard deviations of EM lifetimes are 0.0065, 0.0080, and 0.0085 for the grain size distributions with standard deviations of 0.1, 0.3, and 0.6, respectively, with the standard deviation (σ) for a lognormal distribution given by (26).

The standard deviations for the EM lifetimes are rather small compared to those frequently observed in experiments [154]. Several factors can explain this behavior. First, for convenience, we have used a small value of stress threshold as failure criterion to determine the interconnect lifetime. As can be seen from Fig. 44, the variation of the lifetimes can be more pronounced for higher stress thresholds. Second, the simulation parameters and material properties are independent of the grain distribution. This means that mechanical properties and diffusivities, for example, are equal and constant for all grains in an interconnect line, for all simulated structures. This is clearly not the case in real experiments, as it is well known that material properties vary not only from sample to sample but also according to the grain distribution along the line. Therefore, the small standard deviations obtained from our simulations, compared to those experimentally observed, should be indeed expected.

Nevertheless, our results show that the microstructure can still affect the EM lifetimes by providing sites of flux divergence and grain boundaries as fast diffusivity paths, so that the lifetimes clearly follow lognormal distributions, as presented in Fig. 45. Moreover, as the standard deviation of the distribution of grains sizes increases, we observed an increase of the standard deviation of the EM lifetime distribution, as shown in Fig. 46. These results strongly imply that the lognormal grain size distribution is the primary cause for the lognormal distribution of the EM lifetimes.

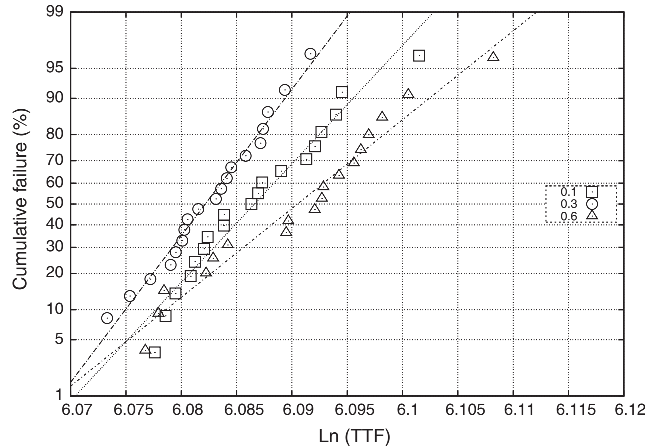

Fig. 45. Electromigration lifetime distributions.

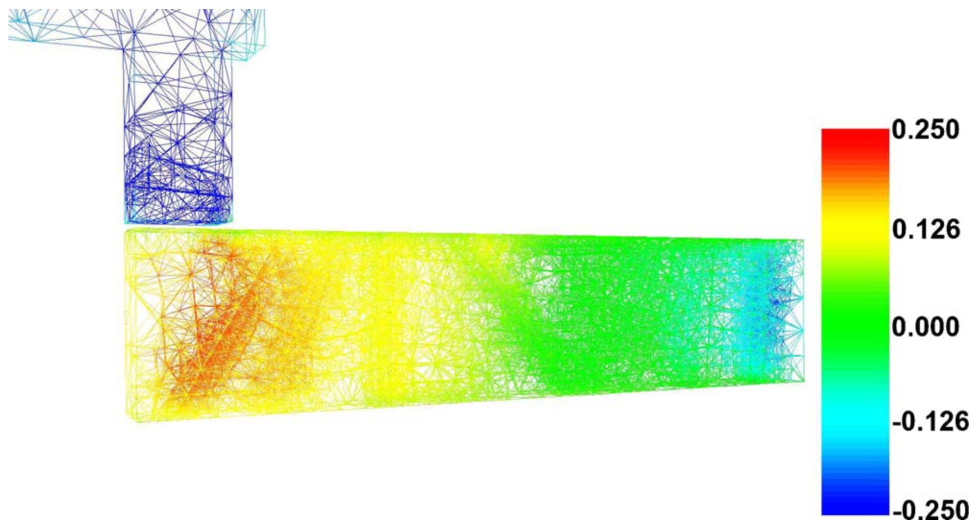

Fig. 43. Hydrostatic stress distribution in a simulated interconnect (in MPa). The peak value is located at grain boundaries, where vacancies are trapped.

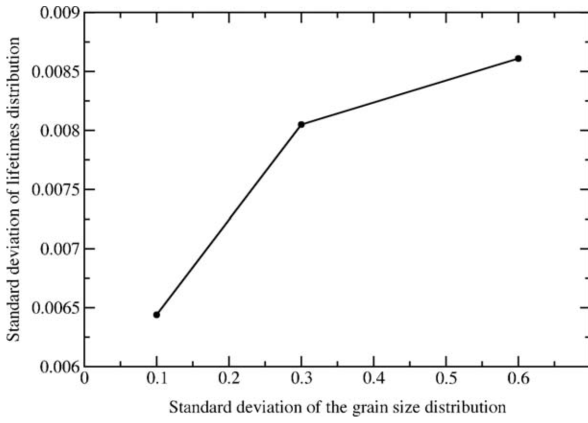

Fig. 46. Electromigration lifetime standard deviation for different standard deviations of grain size.

5. Some special approaches

The methods for EM modeling presented in the previous sections documents the mainstream of published work. The common characteristics of these works is considering all material transport paths (bulk, grain boundary, capping and barrier layer interfaces) and all relevant driving forces (EM, gradient of vacancy/atom concentration, mechanical stress gradient, and temperature gradient). The behavior of the surface of an evolving void, together with all relevant physical influences, is also separately studied. In the following, three special methods of EM modeling are presented. The first two focus on the grain boundary transport and the third on pre-existing voids as basis for drift-less EM.

5.1. The atomic flux divergence approach

The method developed by Sasagawa et al. [156–158] claims the capability of predicting not only the exact position of void nucleation for simple two-dimensional structures, but also void growth to line failure. The central concept of the model is based on the general atomic flux divergence in the interconnect line, AFD_{gen}, which is the sum of the atomic flux divergence in the grain boundary and the bulk [156]

$$\mathrm{AFD}_{gen} = \mathrm{AFD}_{gb} + \mathrm{AFD}_{blk} \tag{183}$$

AFD_{gb} and AFD_{blk} are the atomic flux divergence in the grain boundary and bulk, respectively.

$$\mathrm{AFD}_{gen} = \frac{1}{4\pi}\int_0^{2\pi} (\mathrm{AFD}_{gb\theta} + |\mathrm{AFD}_{gb\theta}|)\,\mathrm{d}\theta \tag{184}$$

For the calculation of AFD_{gen} the complete set of driving forces is applied. In a grain boundary the material transport induced by EM and a temperature gradient is given by [158]

$$\begin{aligned}\mathrm{AFD}_{gb(\theta)} = {}& C_{gb}\rho \frac{4}{\sqrt{3}\,d^2}\frac{1}{T}\exp\left(-\frac{E_{gb}}{kT}\right)\Bigg\{\sqrt{3}\Delta\varphi(j_x\cos(\theta) \\ & + j_y\sin(\theta)) - \frac{d}{2}\Delta\varphi\left[\left(\frac{\partial j_x}{\partial x} - \frac{\partial j_y}{\partial y}\right)\cos(2\theta)\right. \\ & \left. + \left(\frac{\partial j_x}{\partial y} + \frac{\partial j_y}{\partial x}\right)\sin(2\theta)\right] + \frac{\sqrt{3}d}{4T}\left(\frac{E_{gb}}{kT} - 1\right)\left(\frac{\partial T}{\partial x}j_x + \frac{\partial T}{\partial y}j_y\right)\Bigg\}.\end{aligned} \tag{185}$$

Here j_x and j_y are the components of the current density vector, E_{gb} is the activation energy for grain boundary diffusion, and d is the average grain size. The angle functions in (185) make EM dependent on an angle which the grain boundary closes with the electric current direction (Fig. 47). Positive values of AFD_{gen} indicate sites of atomic depletion. For solving the Laplace equation for the electrostatic potential and the equation of steady state heat conduction the finite element method was applied.

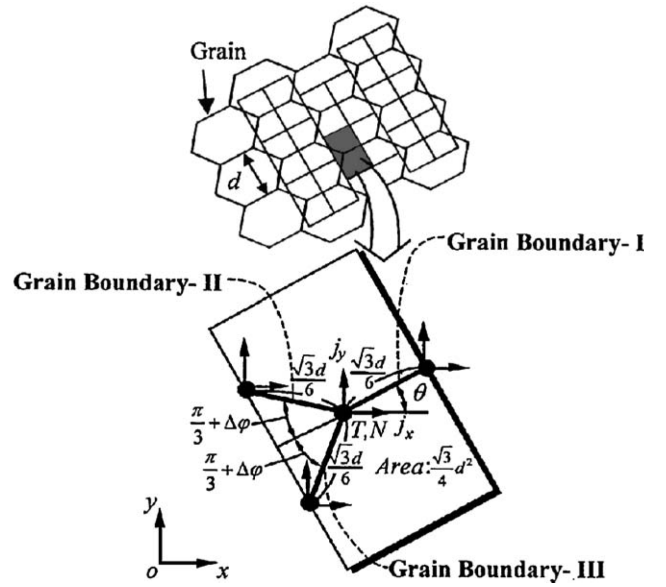

Fig. 47. A model of polycrystalline microstructure introduced for formulation of AFD_{gen}[157].

The studied portion of interconnect is divided into rectangular elements as shown in Fig. 48, the thin elements are set in

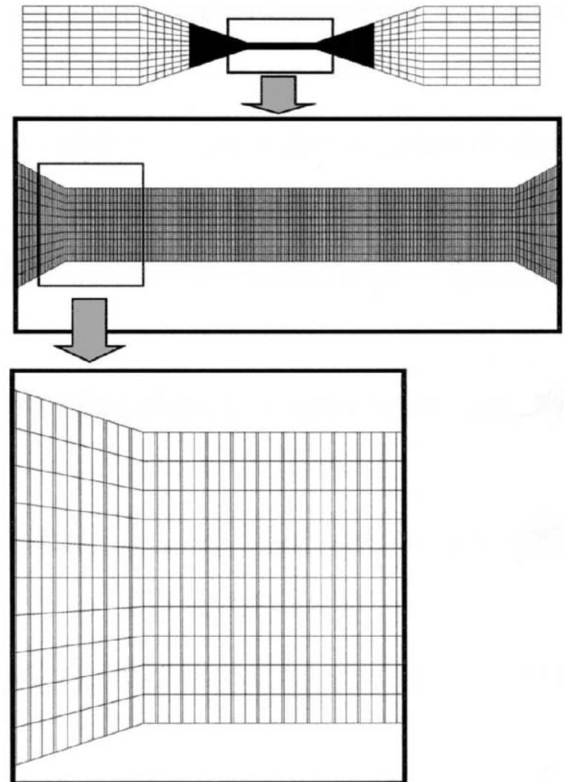

Fig. 48. The finite element mesh used in simulation and its enlargement. Thin elements in the mesh are intended to resolve slit-like voids [157].

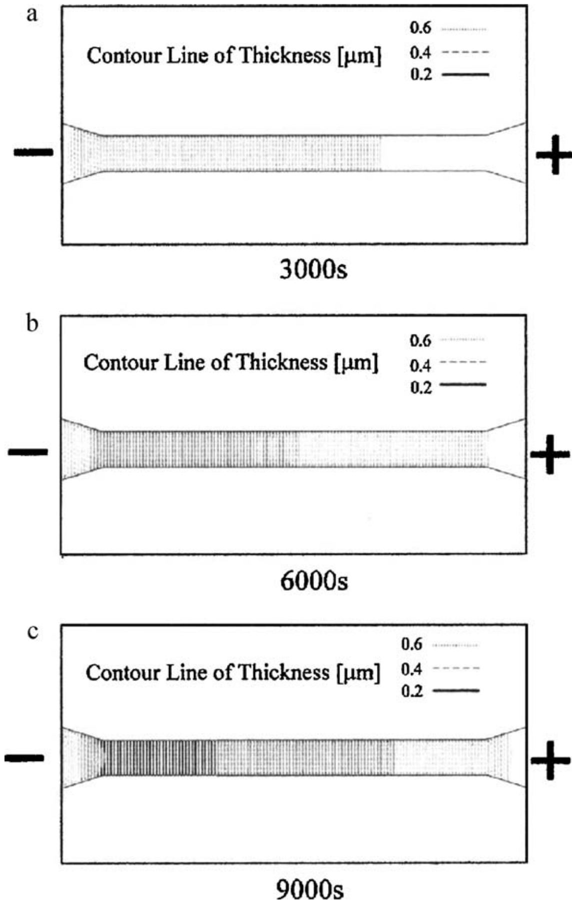

Fig. 49. Time development of slit-like void distribution. Shown is the thickness of slit voids [μm] [157,158].

anticipation of slit-like voids. The net atomic change inside each element is calculated according to AFD_{gen} and for the identification of a void nucleation site the atomic concentration threshold criterion is applied. As a result of EM atom depletion takes place in thin elements and slit-like voids form. The result presented in Fig. 49 shows the formation of slit-like voids, but without taking into account a realistic microstructure. Larger voids which lead to fatal interconnect failure are modeled as a union of many slit-like voids. The prediction of void site and time-to-failure provided by this model is in very good agreement with the presented experimental results, but the simulation and comparison are carried out only for quite simple, basically two-dimensional structures.

This model presents an interesting work aimed to model the whole span of EM development. However, there are several significant drawbacks of the approach. First of all, the continuity equation for atoms (vacancies) is not solved, and, therefore, it is hardly possible to obtain the correct behavior of material transport. Secondly, stress as a driving force is not included, although since the work of Blech [29] it is very well known how crucial its influence is. The finite element mesh used for simulation (Fig. 48) is set, according to the authors [157], based on measurements of average grain size and effective width of slit-like voids [157,158]. However, the microstructure implied by the mesh is very artificial and differs in its basic features both from aluminum as well as copper microstructure. We believe that the void location prediction obtained in the work can also be achieved with a simple continuum model of EM without considering any kind of microstructure. The void formation presented appears to be an obvious result of simple geometrical features.

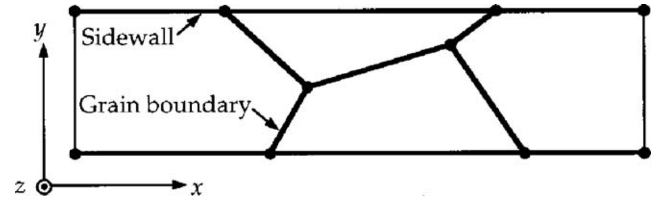

Fig. 50. An example of grain boundary network used for simulation (courtesy of Dr. R. Gleixner) [159].

5.2. Electromigration stress evolution in microstructure

The work of Gleixner and Nix [159] is one of the most comprehensive approaches for EM simulation. It includes detailed physics of EM in grain boundaries with stress effects and mechanisms of void nucleation.

The atom flux along a grain boundary is given by

$$J_a = \frac{D_{gb}}{kT}\left(\frac{\partial \sigma_n}{\partial l} + \frac{F_e \cos(\theta)}{\Omega}\right), \tag{186}$$

where l is the distance along the boundary, θ is the angle between current flow and the grain boundary, and F_e is the EM force along the path aligned with the current flow. It is assumed that ample vacancy sinks and sources are present throughout the material and the vacancy equilibrium is maintained. The volumetric expansion of an element of material given in terms of the atomic flux divergence is

$$\frac{\partial \ln(V)}{\partial t} = -\Omega \nabla \cdot \vec{J}_a. \tag{187}$$

The hydrostatic stress related to this volumetric expansion is

$$\frac{\partial \sigma}{\partial t} = -B\frac{\partial \ln(V)}{\partial t}. \tag{188}$$

Gleixner and Nix [159] consider only a two dimensional network of grain boundaries (Fig. 50). Along the two-dimensional grain boundary, a divergence in the atomic flux causes an effective thickening of the grain boundary. This thickening is modeled as the insertion of a continuum slab of material with width u along the boundary, which is given as

$$\frac{\partial u}{\partial t} = -\delta_{gb}\Omega\frac{\partial J_a}{\partial l}. \tag{189}$$

Combining Eqs. (186) and (189) one obtains

$$\frac{\partial \bar{u}}{\partial t} = -\delta_{gb}\Omega\frac{\partial}{\partial l}\left[\frac{D_{gb}}{kT}\left(\frac{\partial \sigma_n}{\partial l} + \frac{F_e \cos(\theta)}{\Omega}\right)\right]. \tag{190}$$

The variable $\bar{u}$ here is the average displacement of the boundary sidewalls through the line thickness. The normal traction of stress σ_n is related to the average displacement $\bar{u}$ according to

$$\sigma_n = -\Phi\bar{u} + \sigma_n^{\text{ext}}. \tag{191}$$

σ_n^{ext} is the external normal traction which arises from sources external to the boundary under consideration. As the tensile stress increases at a localized region within the line, it creates a large driving force for void nucleation. Gleixner and Nix [159] consequently use the nucleation criterion of Flinn [112,115]. The rate of void growth is determined by calculating the flux of atoms away from the point at which the void has formed. If a void is

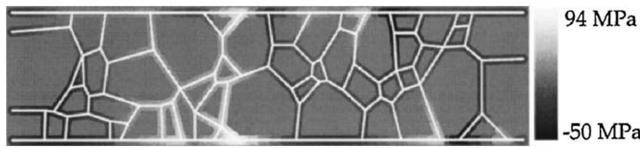

Fig. 51. Grain structure used in the simulations. Shown is the normal stress traction σ_n on the grain boundaries (courtesy of Dr. R. Gleixner) [159].

intersected by several paths, it is necessary to sum the contributions from all the intersecting paths, which gives

$$\frac{\partial V}{\partial t} = \sum_i A_i J_{a,i} \Omega = \frac{D_{gb}\Omega}{kT} \sum_i A_i \left(\frac{\partial \sigma_{n,i}}{\partial l} + \frac{F_e \cos(\theta_i)}{\Omega} \right), \tag{192}$$

where A_i is the area of the grain boundary diffusion path. The normal stress tractions on the grain boundaries σ_n obtained by simulation are shown in Fig. 51. The computationally efficient approach developed by Gleixner and Nix [159] is capable to simulate stress evolution in complex microstructures and can, therefore, be applied to interconnects with realistic grain structures. Both models of void nucleation and growth are integrated and so it is possible to simulate the complete stress evolution and void formation process. The main drawback of the method is that it would be very difficult to implement it for three-dimensional grain boundary networks, even for interconnect portions of moderate size. Furthermore, mechanical stress is not included in modeling void growth. Among others, the work of Gungor and Maroudas [121,122,160] has clearly shown the crucial importance of stress on an evolving void surface.

5.3. The driftless electromigration theory

The approach developed by Sah and Jie [161] is a unique treatment of EM, which renounces the notion of direct and electron wind force. It is argued that the direct force is practically absent, since the electric field is diminishingly small in metal because of the very high concentration of conduction electrons. The weak electric field is also incapable of significantly polarizing the electrons tightly bound to the metal atomic core, thus leaving the electron wind force without effect [161]. The lattice atoms or impurities cannot act as point scatterers which is the basis of all considerations presented in Section 1.3.

This radical view has not been addressed until now by leading experts on quantum-mechanical theory of EM.

Denying any kind of EM induced atom drift Sah and Jie [161] propose a new, "driftless", EM theory. In this theory EM is

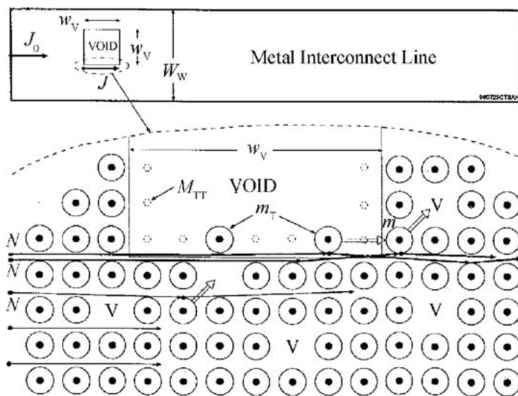

Fig. 52. The EM mechanism according to Sah and Jie [161]. Electrons are represented by dots, small broker circles are aluminum atom trapping sites on the interior surface of the void, and circled dots are the aluminum ion cores.

described as continuous process of trapping and releasing atoms from the surface of intrinsic metallic voids (Fig. 52). The governing equations for the balance of free atoms m and trapped atoms m_T are

$$\frac{\partial m}{\partial t} = D_m \frac{\partial^2 m}{\partial x^2} + (e_m + c_m m) m_T - c_m M_{TT}, \tag{193}$$

$$\frac{\partial m_T}{\partial t} = -(e_m + c_m m) m_T + c_m M_{TT}. \tag{194}$$

e_m is the emission rate of the atoms trapped at the void surface, c_m is the rate of capture of mobile atoms by the unoccupied surface traps, and M_{TT} is the concentration of traps at the surface of the void. The influence of the electrical current density J is given by $e_m = e_{m1} J$ and for higher current densities by $e_m = e_{m2} J^2$, because the drifting electrons also enhance vacancy migration to provide more vacancy sites for the atoms to move.

The work of Sah and Jie represents an interesting alternative development in EM modeling. By abandoning the notion of electron wind and introducing atom exchange on intrinsic void surfaces as exclusive EM mechanism it differs significantly from all other EM models on quantum-mechanical and phenomenological level. However, as EM models generally grow more and more complex alternative concepts may contain ideas for simplifications and compactification of models for practical use in engineering praxis.

6. Summary

Electromigration in interconnect structures of integrated circuits has been recognized as an important reliability problem in the early 1960s and since then extensively studied. This work reviews the history and the development of EM modeling and simulation. With extensive EM studies throughout the years our understanding of EM is becoming better, and improvements in designs and processes for the interconnect system have been made. We have given first an overview over fundamental physical concepts behind EM on a quantum-mechanical level. Different modeling approaches have been discussed together with some of the disputed aspects of the modern understanding of EM. The development of intrinsic voids which lead to interconnect failure goes through two distinctive phases. The first phase is the void nucleating phase and the second phase is the void evolution phase. We have presented the historical development of models for both phases up to the most modern concepts. The results of simulations based on these models have been shown for submicron interconnect features and a possibility of their verification and utilization in interconnect design has been discussed. Some concepts for the usage of simulation tools in combination with experimental tests have been also presented.

Acknowledgment

This work has been partly supported by the Austrian Science Fund with the project P18825-N14.

References

[1] P.R. Justinson, Analysis of Electromigration in Single- and Dual-Inlaid Cu Interconnects, Dissertation, The University of Texas at Austin, 2003.
[2] M. Hauschield, Statistical Analysis of Electromigration Lifetimes and Void Evolution in Cu Interconnects, Dissertation, The University of Texas at Austin, 2005.
[3] K.J. Puttlitz, K.A. Statler, Handbook of Lead-Free Solder Technology for Microelectronic Assemblies, CRC Press, 2004.
[4] J.R. Lloyd, Appl. Phys. Lett. 79 (7) (2000) 1061–1062.
[5] J.R. Lloyd, Microelectron. Eng. 49 (1999) 51–64.
[6] A. Christou, Electromigration and Electronic Device Degradation, Wiley-Interscience, 1994.
[7] C.M. Tan, A. Roy, Mater. Sci. Eng. 58 (1–2) (2007) 1–75.

[8] E.T. Ogawa, K.D. Lee, V.A. Blaschke, P. Ho, IEEE Trans. Reliabil. 51 (4) (2002) 403–419.
[9] C. Bosvieux, J. Friedel, J. Phys. Chem. Solids 23 (1962) 123–136.
[10] R. Sorbello, Phys. Rev. B 31 (1985) 798–804.
[11] A. Lodder, Physica A 158 (3) (1989) 723–739.
[12] H.B. Huntington, A.R. Grone, J. Phys. Chem. Solids 20 (1/2) (1961) 76–87.
[13] K. Hess, Advanced Theory of Semiconductor Devices, Prentice Hall, 1988.
[14] E. Merzbacher, Quantum Mechanics, John Wiley and Sons, Inc., 1998.
[15] A. Lodder, Europhys. Lett. 72 (5) (2005) 774–779.
[16] R. Kubo, J. Phys. Soc. Jpn. 12 (1957) 570–586.
[17] P. Kumar, R.S. Sorbello, Thin Solid Films 25 (1975) 25–35.
[18] L.E. Reichl, A Modern Course in Statistical Physics, Wiley-VCH, 2004.
[19] A. Lodder, J. Phys. Chem. Solids 51 (1) (1990) 19–25.
[20] R.S. Sorbello, J. Phys. Chem. Solids 34 (6) (1973) 937–950.
[21] L.J. Sham, Phys. Rev. B 12 (8) (1975) 3142–3149.
[22] W.L. Schaich, Phys. Rev. B 13 (8) (1976) 3350–3359.
[23] R.P. Feynman, Phys. Rev. 56 (4) (1939) 340–343.
[24] A.H. Verbruggen, R. Griessen, Phys. Rev. B 32 (2) (1985) 1426–1429.
[25] A. Lodder, J.P. Dekker, AIP Conf. Proc. 418 (1998) 315–329.
[26] J. Lloyd, K.P. Rodbell, in: G.C. Schwartz, K.V. Srikrishnan (Eds.), Handbook of Semiconductor Interconnection Technology, 2006, pp. 471–520.
[27] J.R. Black, IEEE Trans. Elec. Dev. 16 (4) (1969) 338–347.
[28] A. von Glasow, Zuverlässigkeitsaspekte von Kupfermetallisierungen in Integrierten Schaltungen, Dissertation, Technische Universität München, 2005.
[29] I.A. Blech, C. Herring, J. Appl. Phys. 29 (3) (1976) 131–133.
[30] I.A. Blech, J. Appl. Phys. 47 (4) (1976) 1203–1208.
[31] I.A. Blech, K.L. Tai, Appl. Phys. Lett. 30 (8) (1976) 387–389.
[32] H.A. Schafft, T.C. Staton, J. Mandel, J.D. Shott, IEEE Trans. Elec. Dev. 34 (3) (1987) 673–681.
[33] B.J. Root, T. Turner, Proc. Intl. Reliab. Phys. Symp. (1985) 100–107.
[34] C.C. Hong, D.L. Crook, Proc. Intl. Reliab. Phys. Symp. (1985) 108–114.
[35] R.E. Jones, L.D. Smith, J. Appl. Phys. 61 (1987) 4670–4678.
[36] R.W. Pasco, J.A. Schwarz, Proc. Intl. Reliab. Phys. Symp. (1983) 10–23.
[37] A. Scorzoni, B. Neri, C. Caprile, F. Fantini, Mater. Sci. Rep. 7 (1991) 143–220.
[38] T.M. Chen, T.P. Djeu, R.D. Moore, Proc. Intl. Reliab. Phys. Symp. (1985) 87–92.
[39] J. Lloyd, J.J. Clement, Thin Solid Films 262 (1) (1995) 135–141.
[40] E. Zschech, P.R. Besser, Proc. Interconnect Technol. Conf. (2000) 233–235.
[41] M.A. Meyer, I. Zienert, E. Zschech, Mater. Inform. Technol. 1 (1) (2005) 95–100.
[42] J.R. Lloyd, Semicond. Sci. Technol. 12 (1997) 1177–1185.
[43] J.Y. Kim, Investigation on the Mechanism of Interface Electromigration in Copper Thin Films, Dissertation, The University of Texas at Arlington, 2006.
[44] C. Ryu, K.-W. Kwon, A.L.S. Loke, H. Lee, T. Nogami, V.M. Dubin, R.A. Kavari, G.W. Ray, S. Wong, IEEE Trans. Elec. Dev. 46 (6) (1999) 1113–1120.
[45] O. Kraft, E. Arzt, Acta Mater. 46 (11) (1998) 3733–3743.
[46] C.W. Chang, C.V. Thompson, C.L. Gan, K.L. Pey, W.K. Choi, Y.K. Lim, Appl. Phys. Lett. 90 (2007) 193505.
[47] Z.-S. Choi, R. Mönig, C.V. Thompsona, Appl. Phys. Lett. 90 (2007) 241913.
[48] D.T. Walton, H.J. Frost, C.V. Thompson, Proc. Mat. Res. Soc. Symp. 225 (1991) 219–224.
[49] E. Arzt, W.D. Nix, J. Mater. Res. 6 (1991) 731–736.
[50] H. Kang, I. Asano, C. Ryu, S. Wong, Proc. Intl. VLSI Multilevel Interconnection Conf., 1993, 223–229.
[51] E. Zschech, M.A. Meyer, S.G. Mhaisalkar, A.V. Vairagar, A. Krishnamoorthy, H.J. Engelmann, V. Sukharev, Proc. Intl. Conf. Mater. Adv. Technol. 504 (1–2) (2005) 279–283.
[52] J. Lloyd, E. Arzt, Symp. Proc. Mater. Reliabil. Microelectron. II 265 (1992) 45–57.
[53] A.H. Fischer, A. Abel, M. Lepper, A.E. Zitzelsberger, A. von Glasow, Proc. Intl. Reliab. Phys. Symp. (2000) 359–363.
[54] A. von Glasow, A.H. Fischer, D. Bunel, G. Friese, A. Hausmann, O. Heitzsch, M. Hommel, J. Kriz, S. Penka, P. Raffin, C. Robin, H.P. Sperlich, F. Ungar, A.E. Zitzelsberger, Proc. Intl. Reliab. Phys. Symp. (2003) 146–150.
[55] C.L. Gan, C.V. Thompson, K.L. Pey, W.K. Choi, J. Appl. Phys. 94 (2) (2003) 1222–1228.
[56] M. Hauschildt, M. Gall, S. Thrasher, P. Justison, R.H.L. Michaelson, H. Kawasaki, P.S. Ho, Appl. Phys. Lett. 88 (21) (2006) 2119071–2119073.
[57] M. Hauschildt, M. Gall, S. Thrasher, P. Justison, R. Hernandez, H. Kawasaki, P.S. Ho, J. Appl. Phys. 101 (4) (2007) 0435231–0435239.
[58] S.H. Kang, E. Shin, Solid-State Electron. 45 (2001) 341–346.
[59] H. Wever, Elektro- und Thermotransport in Metallen, Johann Ambrosius Barth, Leipzig, 1973.
[60] M. Shatzkes, J.R. Lloyd, J. Appl. Phys 59 (11) (1986) 3890–3893.
[61] M.A. Korhonen, P. Borgesen, K.N. Tu, C.Y. Li, J. Appl. Phys. 73 (8) (1993) 3790–3799.
[62] R.W. Balluffi, A.V. Granato, in: F.N.R. Nabarro (Ed.), Dislocation in Solids, 1979, pp. 1–133.
[63] J.J. Clement, IEEE Trans. Dev. Mat. Rel. 1 (1) (2001) 33–42.
[64] S.R. deGroot, Physica 9 (1942) 923–924.
[65] J.J. Clement, J. Appl. Phys. 82 (12) (1997) 5991–6000.
[66] R. Rosenberg, M. Ohring, J. Appl. Phys. 42 (13) (1971) 5671–5679.
[67] R.W. Balluffi, Grain Boundary Structure and Kinetics, ASM, Metals Park, 1980, pp. 297–329.
[68] R.W. Balluffi, Metall. Trans. A 13 (1982) 2069–2095.
[69] R. Kirchheim, Acta Metall. Mater. 40 (2) (1992) 309–323.
[70] M.E. Sarychev, Y.V. Zhitnikov, J. Appl. Phys. 86 (6) (1999) 3068–3075.
[71] V. Sukharev, E. Zschech, W.D. Nix, J. Appl. Phys. 102 (5) (2007) 530501–530514.
[72] M.R. Sorensen, Y. Mishin, A.F. Voter, Phys. Rev. B 62 (6) (2000) 3658–3673.
[73] J.C. Fisher, J. Appl. Phys. 22 (1) (1951) 74–77.
[74] R.E. Hoffman, D. Turnbull, J. Appl. Phys. 22 (5) (1951) 634–639.
[75] I. Kaur, Y. Mishin, W. Gust, Fundamentals of Grain and Interphase Boundary Diffusion, Wiley, West Sussex, 1995.
[76] C. Herring, J. Appl. Phys. 21 (5) (1950) 437–445.
[77] C. Herring, in: W.E. Kingston (Ed.), Physics of Powder Metallurgy, 1951, pp. 143–179.
[78] C. Herring, in: R. Gomer, C.S. Smith (Eds.), Structure and Properties of Solid Surfaces, 1952, pp. 5–81.
[79] F.C. Larche, J. Cahn, Acta metall. 21 (1973) 1051–1062.
[80] F.C. Larche, J. Cahn, Acta metall. 26 (1978) 1579–1589.
[81] F.C. Larche, J. Cahn, Acta metall. 33 (3) (1985) 331–357.
[82] H. Ceric, R.L. de Orio, J. Cervenka, S. Selberherr, IEEE Trans. Dev. Mat. Rel. 9 (1) (2009) 9–19.
[83] G.L. Povirk, Proc. Mater. Res. Soc. Symp. 473 (1997) 327–342.
[84] S. Rzepka, M.A. Korhonen, E.R. Weber, C.Y. Li, Proc. Mater. Res. Soc. Symp. 473 (1997) 329–335.
[85] H. Ceric, R. Heinzl, C. Hollauer, T. Grasser, S. Selberherr, Stress-Induced Phenomena in Metallization, AIP, 2006, pp. 262–268.
[86] H. Ye, C. Basaran, D. Hopkins, IEEE Trans. Comp. Pack. Manufact. Technol. 26 (3) (2003) 673–681.
[87] R. Kirchheim, U. Kaeber, J. Appl. Phys. 70 (1) (1991) 172–181.
[88] K. Weide-Zaage, D. Dalleau, X. Yu, Microelectron. Reliab. 43 (9) (2003) 1821–1826.
[89] P.R. Besser, E. Zschech, W. Blum, D. Winter, R. Ortega, S. Rose, M. Herrick, M. Gall, S. Thrasher, M. Tiner, B. Baker, G. Braeckelmann, L. Zhao, C. Simpson, C. Capasso, H. Kawasaki, E. Weitzman, J. Electron. Mater. 30 (4) (2001) 320–330.
[90] J.P. Hirth, J. Lothe, Theory of Dislocations, McGraw-Hill, 1968.
[91] V. Sukharev, A. Kteyan, E. Zschech, W.D. Nix, IEEE Trans. Dev. Mat. Rel. 9 (1) (2009) 87–97.
[92] A. Kteyan, V. Sukharev, M.A. Meyer, E. Zschech, W.D. Nix, Stress-Induced Phenomena in Metallization, AIP, 2007, pp. 42–55.
[93] N. Singh, A.F. Bower, D. Gan, S. Yoon, P.S. Ho, J. Leu, S. Shankar, J. Appl. Phys. 97 (1) (2004) 135391–1353911.
[94] C.P. Flynn, Point Defects and Diffusion, Clarendon Press, Oxford, 1972.
[95] M.E. Glicksman, Diffusion in Solids, John Wiley and Sons, Inc., 2000.
[96] M.J. Aziz, Appl. Phys. Lett. 70 (21) (1997) 2810–2812.
[97] M.J. Aziz, Proc. Simulation of Semiconductor Processes and Devices Conf., 2003, 137–142.
[98] B.M. Clemens, W.D. Nix, R.J. Gleixner, J. Mater. Res. 12 (8) (1997) 2038–2042.
[99] V. Petrescu, W. Schoenmaker, Predictive Simulation of Semiconductor Processsing: Status and Challenges, Springer Series in Materials Sciences, vol. 72, 2004, pp. 387–456.
[100] V. Sukharev, R. Choudhury, C.W. Park, Physically-Based Simulation of the Early and Long-Term Failures in the Copper Dual Damascene Interconnect, Intl. Integrated Reliability Workshop Final Report, pp. 80–85, 2003.
[101] P.H. Dederichs, K. Schroeder, Phys. Rev. B 17 (6) (1978) 2524–2536.
[102] G.H. Vineyard, J. Phys. Chem. Sol. 3 (1) (1957) 121–127.
[103] K. Schroeder, K. Dettmann, Z. Physik B 22 (1975) 343–350.
[104] M.S. Daw, W. Windl, N.N. Carlson, M. Laudon, M.P. Masquelier, Phys. Rev. B 64 (2001) 045205.
[105] C.C. Liao, Z.H. Gan, Y.J. Wu, K. Zheng, R. Guo, L.F. Zhang, J. Ning, Proc. Intl. Symp. on the Physical and Failure Analysis of Integrated Circuits, 2009, 685–689.
[106] J. Wilkening, L. Borucki, J.A. Sethian, SIAM J. Appl. Math. 64 (6) (2004) 1839–1863.
[107] J. Wilkening, L. Borucki, J.A. Sethian, SIAM J. Appl. Math. 64 (6) (2004) 1864–1886.
[108] C.L. Gan, C.V. Thompson, K.L. Pey, W.K. Choi, H.L. Tay, B. Yu, M.K. Radhakrishnan, Appl. Phys. Lett. 79 (27) (2001) 4592–4594.
[109] J.T. Trattles, A.G. O'Neill, B.C. Mecrow, J. Appl. Phys. 75 (12) (1994) 7799–7804.
[110] R. Raj, M.F. Ashby, Acta metall. 23 (1975) 653–666.
[111] J.P. Hirth, W.D. Nix, Acta metall. 33 (3) (1985) 359–368.
[112] R.J. Gleixner, B.M. Clemens, W.D. Nix, J. Mater. Res. 12 (1997) 2081–2090.
[113] J.W. Christian, The Theory of Transformations in Metal and Alloys, Part I, Pergamon, 2002.
[114] D.A. Porter, K.E. Easterling, Phase Transformations in Metals and Alloys, Stanley Thornes (Publishers) Ltd., 2000.
[115] P.A. Flinn, MRS Bull. 20 (11) (1995) 70–73.
[116] E. Zschech, H.-J. Engelmann, M. Meyer, V. Kahlert, A.V. Vairagar, S.G. Mhaisalkar, A. Krishnamoorthy, M. Yan, K.N. Tu, V. Sukharev, Zeitschrift fur Metallkunde 96 (9) (2005) 966–971.
[117] Z. Jing, M.O. Bloomfield, L. Jian-Qiang, R.J. Gutmann, T.S. Cale, IEEE Trans. Sem. Man. 19 (4) (2006) 437–448.
[118] P.S. Ho, J. Appl. Phys. 41 (1) (1970) 64–68.
[119] Z. Suo, W. Wang, J. Appl. Phys. 76 (6) (1994) 3410–3421.
[120] M.E. Gurtin, Thermomechanics of Evolving Phase Boundaries in the Plane, Clarendon Press, Oxford, 1993.
[121] M.R. Gungor, D. Maroudas, Appl. Phys. Lett. 72 (26) (1998) 3452–3454.
[122] M.R. Gungor, D. Maroudas, Appl. Phys. Lett. 73 (26) (1998) 3848–3850.
[123] D.R. Fridline, A.F. Bower, J. Appl. Phys. 85 (6) (1999) 3168–3174.
[124] E. Arzt, O. Kraft, W.D. Nix, J.E. Sanchez, J. Appl. Phys. 76 (3) (1994) 1563–1571.
[125] M. Mahadevan, R. Bradley, Phys. Rev. B 59 (16) (1999) 11037–11046.
[126] M. Mahadevan, R. Bradley, Physica D 126 (3) (1999) 201–213.
[127] M. Mahadevan, R. Bradley, J.M. Debierre, Europhys. Lett. 45 (1999) 680–685.
[128] D.N. Bhate, A.F. Bower, A. Kumar, J. Mech. Phys. Solids 50 (2002) 2057–2083.
[129] D.N. Bhate, A. Kummar, A.F. Bower, J. Appl. Phys. 87 (4) (2000) 1712–1721.
[130] J. Blowey, C. Elliott, Eur. J. Appl. Math. 2 (1991) 233–279.
[131] J. Blowey, C. Elliott, Eur. J. Appl. Math. 3 (1992) 147–179.
[132] H. Ceric, S. Selberherr, IEICE Trans. Electron. (3) (2002) 421–426.

[133] H. Ceric, R. Sabelka, S. Holzer, W. Wessner, S. Wagner, T. Grasser, S. Selberherr, Proc. Simulation of Semiconductor Processes and Devices Conf., 2004, 331–334.
[134] P.S. Ho, T. Kwok, Rep. Prog. Phys. 52 (1989) 301–348.
[135] F.M. d'Heurle, P.S. Ho, in: J.M. Poate, K.N. Tu, J.W. Mayer (Eds.), Thin Films: Interdiffusion and Reactions, vol. 1, 1978, pp. 243–303.
[136] D.N. Bly, P.J. Rous, Phys. Rev. B 53 (20) (1996) 13909–13920.
[137] R.S. Sorbello, Proc. Mater. Res. Soc. Symp. (1996) 73–81.
[138] T. Ohkubo, Y. Hirotsu, K. Nikawa, Mater. Trans., JIM 37 (1996) 454–457.
[139] T. Shinzawa, T. Ohta, Proc. IEEE Intl. Interconnect Technology Conf., 1998, p. 427.
[140] D. Maroudos, M.R. Gungor, Comput. Mater. Sci. 23 (2002) 242–249.
[141] F.G. Sen, M.K. Aydinol, Turkish J. Eng. Environ. Sci. 30 (2006) 387–394.
[142] F.G. Sen, M.K. Aydinol, J. Appl. Phys. 104 (2008) 073510.
[143] J.D. Gale, A.L. Rohl, Mol. Simul. 29 (2003) 291–341.
[144] V. Heine, I.V. Abarenkov, Philos. Mag. 9 (1964) 451–465.
[145] I.V. Abarenkov, V. Heine, Philos. Mag. 12 (1965) 529–537.
[146] R.S. Sorbello, Proc. Mat. Res. Soc. Symp. 225 (1991) 2–12.
[147] P.J. Rous, D.N. Bly, Phys. Rev. B 62 (12) (2000) 8478–8486.
[148] L.J. Bain, M. Engelhardt, Statistical Analysis of Reliability and Life-Testing Models, Marcel Dekker, Inc., 1991.
[149] E.T. Ogawa, J.W. McPherson, J.A. Rosal, K.J. Dickerson, T.C. Chiu, L.Y. Tsung, M.K. Jain, T.D. Bonifiled, J.C. Ondrusek, W.R. McKee, Proc. Intl. Reliab. Phys. Symp. (2002) 312–321.
[150] H. Matsuyama, M. Shiozu, T. Kouno, T. Suzuki, H. Ehara, S. Otsuka, T. Hosoda, T. Nakamura, Y. Mizushima, M. Miyajima, K. Shono, Proc. Intl. Reliab. Phys. Symp. (2007) 638–639.
[151] K. Yoshida, T. Fujimaki, T. Miyamoto, T. Honma, H. Kaneko, H. Nakazawa, M. Morita, Digest Intl. Electron Devices Meeting, 2002, 753–756.
[152] T. Kouno, T. Suzuki, S. Otsuka, T. Hosoda, T. Nakamura, Y. Mizushima, M. Shiozu, H. Matsuyama, K. Shono, H. Watatani, Y. Ohkura, M. Sato, S. Fukuyama, M. Miyajima, Digest Intl. Electron Devices Meeting, 2005, 187–190.
[153] A.V. Vairagar, S.G. Mhaisalkar, A. Krishnamoorthy, K.N. Tu, A.M. Gusak, M.A. Meyer, E. Zschech, Appl. Phys. Lett. 85 (13) (2004) 2502–2504.
[154] M. Hauschildt, M. Gall, S. Thrasher, P. Justison, R. Hernandez, H. Kawasaki, P.S. Ho, J. Appl. Phys. 101 (2007) 043523.
[155] L. Arnaud, T. Berger, G. Reimbold, J. Appl. Phys. 93 (1) (2003) 192–204.
[156] K. Sasagawa, N. Nakamura, M. Saka, H. Abe, J. Electron. Packag. 120 (1) (1998) 360–366.
[157] K. Sasagawa, K. Naito, M. Saka, H. Abe, J. Appl. Phys. 87 (6) (2000) 2785–2791.
[158] K. Sasagawa, M. Hasegawa, M. Saka, H. Abe, J. Appl. Phys. 91 (11) (2002) 9005–9014.
[159] R.J. Gleixner, W.D. Nix, J. Appl. Phys. 86 (4) (1999) 1932–1944.
[160] M.R. Gungor, D. Maroudas, J. Appl. Phys. 85 (4) (1999) 2233–2246.
[161] C.-T. Sah, B.B. Jie, Chinese J. Sem. 25 (5) (2008) 815–821.